Influence of Discharge Ratio and Junction Angle on Sediment Transport and Deposition Patterns in Open Channel Confluences: An Experimental Study

QINGCHENG YU

Thesis submitted to the University of Ottawa
in partial fulfillment of the requirements for
The Master of Applied Science degree in Civil Engineering

Faculty of Engineering
University of Ottawa

Abstract

Open channel confluences are common geographical structures in surface runoff. Most natural rivers originate from mountains and hills, flow into a main stream at confluences and finally head into the sea. Confluences are major sites for a main stream to obtain sediment and water from a tributary. Complex turbulence structures such as vortices, flow stagnation, secondary flow, flow re-circulation and water exchange both in vertical and lateral directions result in complicated sedimentation, erosion, mixing and contaminant transport at open channel confluences. The detailed study of flow dynamics and morphodynamics in confluences is of great significance to the urban flood control, scour of the river bed, design and maintenance of the channel and sediment and pollutants transport. This thesis describes a novel flume experiment on the sediment transport patterns in channel confluences as a function of different flow and geometry conditions. The initial equilibrium bed geometry was developed in a mobile bed confluence flume under four cases including two junction angles and two discharge ratios. The equilibrium bed was fixed for each case allowing for detailed flow velocimetry. The observed spatial patterns of turbulence statistics are evaluated with respect to the equilibrium bathymetry. Sediment were then fed instantaneously to the tributary channel at three different feeding sites in order to study the sediment deposition patterns. It was observed that although the sediment initiated at different feeding sites move along different paths through the confluence, all sediment tend to deposit at the face of the dune in the flow separation zone. This thesis also investigated how the deposition pattern would change versus time when feeding at the same site from the tributary channel. The time history of deposition pattern was also investigated for one of the cases. The sediment that initially deposit at the face of the dune eventually moved to the back of the dune and deposit around the post-confluence scour hole, demonstrating that over time the deposition pattern evolves to a state which is similar with the original bed morphology.

Acknowledgments

First, I would like to thank Dr. Colin Rennie, my supervisor and the chair of Department of Civil Engineering, University of Ottawa. He always tried his best to help me out when I had troubles in my research. In addition, he takes a very serious and highly responsible attitude towards both academic research and thesis writing. It is such a great honor for me to have Dr. Rennie being my first supervisor during my academic career. He is more than a supervisor or a teacher to me, but also a close friend and a great example.

I would also like to thank Dr. Saiyu Yuan, the professor of the Department of Hydraulic Engineering, Hohai University. He also gave me a lot of precious guidance during my work and helped me solve the accommodation and experiment expenses issues. I would like to acknowledge that Dr. Saiyu's contribution on this study is equivalent to the second supervisor. Unfortunately, his name could not appear on the front page due to University of Ottawa's regulations. I would like to acknowledge Dr. Majid Mohammadian and Dr. Ousmane Seidou as the examiners of this thesis and the defence, and I am very appreciated for their very valuable comments on this thesis.

Thank you to Guolong Zhao, Huiming Zhang, Quanshuai Liu, Hanqing Zhao and Saber Ansari for their assistance in the flow field data collection, sediment feeding and image rectification. Thanks to financial aid from the International Experience Scholarship Program of University of Ottawa and the "111" Program of Hohai University. Without their help, I would never accomplish so much.

I must express my very profound gratitude to my parents, Haiying Yu and Wei Jiao for providing me with unfailing support and continuous encouragement throughout my study.

Finally, I would like to give my special thanks to my girlfriend, Amanda Chen. Her lovely smile gives all the reasons why I keep pursuing.

Contents

List of Figures

List of Tables

Nomenclature

α	Confluence junction angle (°)
γ	Unite weight of clear Water in 25℃ (N/m^3)
η_1	Percentage of total (%)
η_2	Percentage of grains smaller than the sieve pore size (%)
ν	Kinematic viscosity of clear water in 25℃(Pa·s)
ρ_s	Dry density of sediment
b_1	Tributary channel width (m)
b_2	Main channel upstream width (m)
b_3	Downstream channel width (m)
d	Grain size (mm)
D	Sieve pore size (mm)
D_{25}	Diameter that 25% of the specimen is finer than
D_{50}	Diameter that 50% of the specimen is finer than
D_{75}	Diameter that 50% of the specimen is finer than
D_{90}	Diameter that 90% of the specimen is finer than
E	Gradation test error

F_r	Froude number
F_{r_t}	Froude number for tributary stream
F_{r_m}	Froude number for main stream
F_{r_d}	Froude number for downstream stream
ΔF	Relative filtered amount for Reynolds shear stress
g	Gravitational acceleration (m/s^2)
h_0	Initial bed surface elevation (m)
h_1	Flow surface elevation (m)
Δh	Flow depth (m)
M_1	Sieve weight (g)
M_2	Sieve and passing weight (g)
ΔM	Net passing weight (g)
P	Wetted perimeter (m)
Q	Discharge rate (L/s)
Q_t	Discharge rate of the tributary channel (L/s)
Q_m	Discharge rate of the main channel (L/s)
Q_d	Downstream discharge rate (L/s)
Q_r	Discharge ratio
R	Hydraulic radius (m)

RSS	Reynolds shear stress (N/m^2)
RSS'	Raw Reynolds shear stress in ADV data file (N/m^2)
RSS_r	Filtered Reynolds shear stress (N/m^2)
Re	Reynolds number
Re_t	Reynolds number for the tributary stream
Re_m	Reynolds number for the main stream
Re_d	Reynolds number for downstream stream
S_o	Sorting coefficient
TKE	Turbulent kinetic energy (m^2/s^2)
U	Flow velocity component in x-axis direction (m/s)
V	Flow velocity component in y-axis direction (m/s)
W	Flow velocity component in z-axis direction (m/s)
UV	Reynolds shear stress component, τ_{uv}(N/m^2)
UW	Reynolds shear stress component, τ_{uw}(N/m^2)
VW	Reynolds shear stress component, τ_{vw}(N/m^2)
W_o	Original sample weight (g)

Chapter 1 Introduction

1.1 Terminology

In geography, an open channel confluence or junction occurs where two or more open channel rivers or flows join together to form a single channel. While it is possible for multiple channels to join at the same junction, the confluences studied in this thesis refer to that of only two channels joining.

An open channel confluence can occur in several configurations: where a smaller lower flow river (tributary) joins a larger river (main stream); or where two streams with comparable flow rates meet together and become the source of a new river with a different name; or, where two anabranch channels originating from one river rejoin at a downstream junction. All three types will be considered in this paper. Open channel confluences are common geographical structures in river networks, both in natural rivers (Figure 1) and in artificial canals (Figure 2).

Figure 1. The confluence of Mississippi River and Missouri River, U.S.A. The flow direction is shown as arrows: the blue arrow stands for the tributary flow while the red arrow stands for the main flow. The blue line indicates the shear layer. (Modified after [21])

Figure 2. The confluence in Meixi Stream, China. The flow direction is shown as arrows: the blue arrow stands for the tributary flow while the red arrow stands for the main flow. The blue line indicates the shear layer. (Modified after [22])

The region with white bubbles seen in Figure 2 indicating intensive flow mixing is referred to as the confluence zone. It generally starts at the mouth of tributary and the main stream cross section which lines between the apex of the junction corner and the opposite point in the outer bank and ends at the tail of flow recovery zone. A general conceptual model describing the various components of a confluence flow field is introduced later in Section 2.1.

1.2 Significance

Open channel confluence flow is very common in nature and daily life, which is of great concern to environmental engineering and water conservancy projects. The exchange of water in a confluence area produces a lot of unique hydraulic characteristics, mainly including secondary flow, local scouring, sedimentation and so on. Research on the flow characteristics of confluences is important to address problems such as urban flood control, riverbed erosion, sediment transport, pollutants mixing and transport both in theory and practice. In recent years, due to the utilization of water resources, the management of fluvial channel regulation, the construction of urban flood control projects and city planning, the flow characteristics of open channel confluences has increasingly attracted research attention. To demonstrate the importance of confluence research, some of these aspects are addressed in more detail below.

1.2.1 Urban Drainage Pipe and Canal System

Urban drainage issues include industrial waste-water, sanitary sewage emission and rainfall drainage. Blockage is prone to take place in the separation zone and stagnation zone at an open channel confluence decreasing the transport capacity of the drainage. Open channel confluences are also the places where pollutants begin to diffusion into a main stream. Therefore, research on flow characteristics at open channel confluences is necessary for the operation and maintenance of urban drainage system (Figure 3).

Figure 3. The canal confluence management in L.A. River, U.S.A[23].

1.2.2 The Sediment Transport and the Fluvial Bed Evolution

The flow characteristics of open channel confluence are of great importance to the study of sediment transport and sedimentology. Tributaries are a major source of main stream sediment. Before tributary sediment goes into the main stream, its size and concentration may vary greatly with that of the main stream, which would break the original equilibrium for the sediment transport [44][63]. Sediment tends to deposit at the separation region and narrow the entire river width. The tributary flow deflects to the outer bank of main stream and is squeezed by the separation zone, leading to flow acceleration and secondary flow, finally resulting in the riverbed erosion.

Due to the availability of water and relatively flat land, despite the flood risk, the junction corner area in river confluences has been considered as one of the best places for urban development and waterway transport for thousands of years. In recent years, due to the increasing need of water resources exploitation and waterway regulation, the problem of water-sediment movement and riverbed evolution has attracted more and more attention. In addition, the open channel confluence issues are very complicated. The channel boundary condition usually varies a lot along the stream, and the relative influence of multiple variables such as flux ration, confluence angle, channel width, bed topography, river bed composition and sediment concentration make it really difficult to analyze.

The shoals at the mouth of open channel confluences are often the crucial part of the channel regulation. For example, in Szechwan province, China, the Dadu River and Fuhe River join at Leshan Mountain, Minjiang River and Jinshan River join at Yibin City, Tuojiang River flows into The Yangtze River at Luzhou City, Jialing River joins The Yangtze River at Chongqing City, and Wusuri River goes into The Yangtze River at Beili City etc. (Figure 4) [63]. The above-mentioned confluences have been the focus of recent research in Chinese hydrology, morphology, river conservancy and waterway regulation [33] [16] [54]. Moreover, it is of great importance to analyze the impact of reservoirs on confluences [17] [57]. For example, the waterway condition at the confluence area of Jialing River and The Yangtze River has been a hot spot in recent channel research after the Three Gorges Dam was built. [16] [54] [32]

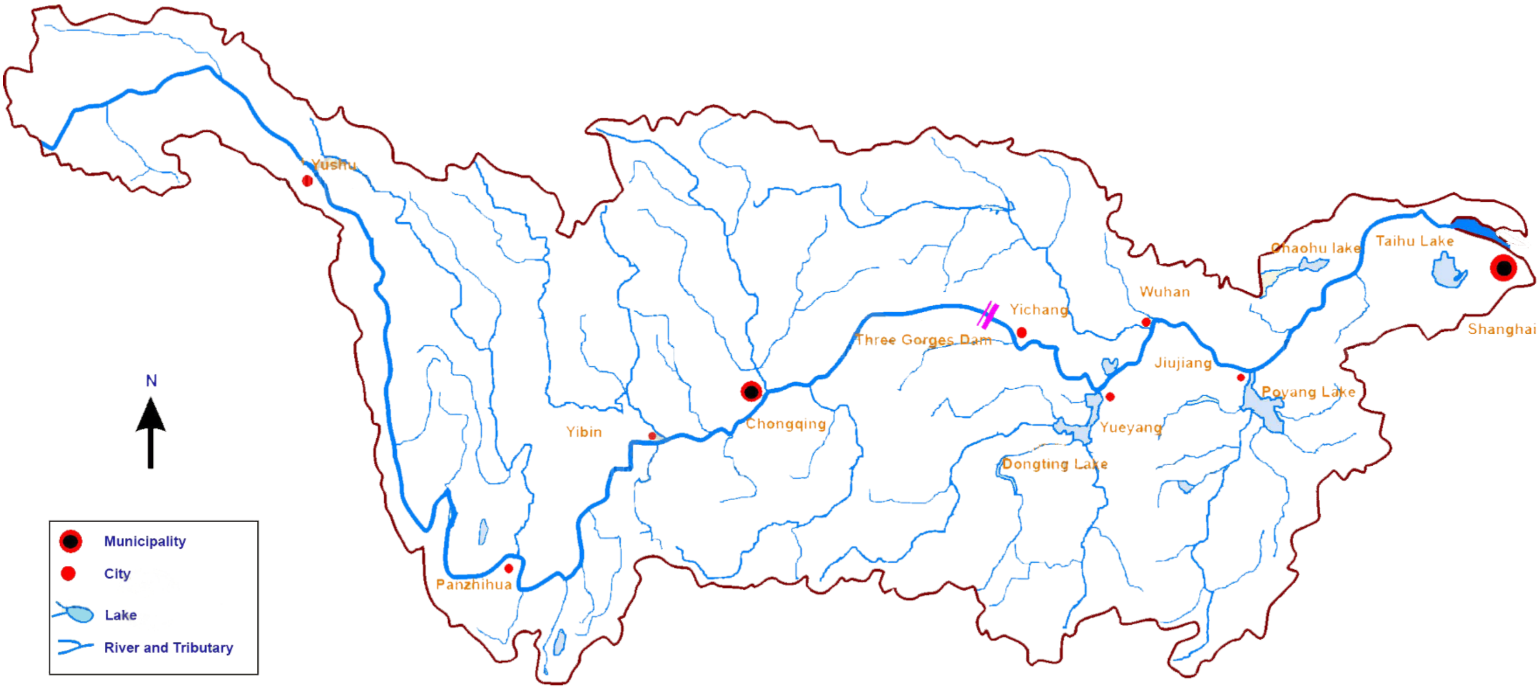

Figure 4. The water system of the Yangtze River [25]

1.2.3 Pollutants Mixing and Transport

Due to the enormous cost of wastewater treatment, in developing countries sewage is often treated in a simple and cursory way and then discharged into the nearby river. At the same time, because the infrastructure of urban and rural areas is imperfect, the surface runoff load resulting from rainfall usually flows directly into the nearby rivers, then flows into the main stream. Finally, at the confluence area the traffic is usually more developed and the population is larger, which often causes serious water pollution. It is necessary to predict the pollution mixing area accurately in the vicinity of confluences, so as to maintain clean water bodies and control water pollution in the most efficient way. It is worth noting that pollutants are often adsorbed to sediment, thus transport of polluted sediment in confluences is a subject deserving greater research effort.

1.3 Organization of the Thesis

This thesis firstly looks into the previous studies on confluence flow and sedimentation patterns through both experimental and numerical methods in order to summarize the common results, analyze the possible reasons for different conclusions, compare the different methodologies, point out the flaws and propose the possible future research areas. From the literature review a set of research objectives is developed.

The experimental methodology follows (Chapter 4) including the flume parameters, the flow condition, measurements and the experiment procedures. This part will also explain the reason why the experiment is designed as it is, as well as other preliminary testing arrangements that proved to be infeasible.

The fifth chapter shows the experiment results of the morphology, the flow field and the sedimentation patterns for different series. This chapter will also introduce the methods of data processing and analyze the results preliminarily.

Finally, a deep analysis summarizes the general pattern of sediment transport and morphodynamics. In addition, this chapter will also include the underlying defects and limitations of this experiments in order to set warnings and provide a reference for future studies.

Chapter 2 Literature Review

2.1 Conceptual Model and Flow Patterns

The physical factors that define a confluence include: the channel width, flow depth, confluence angle (α in Figure 5), bed topography, discharge ratio, sediment concentration and cross sectional configuration. The "discharge ratio" in this thesis is defined as the ratio of tributary flow discharge and mean flow discharge. The cited articles which use other definition will be noted.

Flow dynamics at channel confluences are characterized by six distinct regions including areas of flow stagnation zone, flow deflection zone, flow separation zone (also re-circulation zone in some papers), maximum velocity zone (also flow acceleration zone in some papers), gradual flow recovery zone and shear layer (also mixing layer in some papers) [22] [8] (Figure 5).

As the tributary flow approaches the confluence zone, it deflects gradually towards downstream due to the lateral constraint of the main channel flow at the flow deflection zone. In the meantime, the incoming tributary flow also squeezes the flow path of the main stream and may cause a slight rise of upstream water level [30][58], sometimes resulting in a back-water effect towards the upstream[62], and even a local separation zone adjacent to the outer bank of upstream[19].

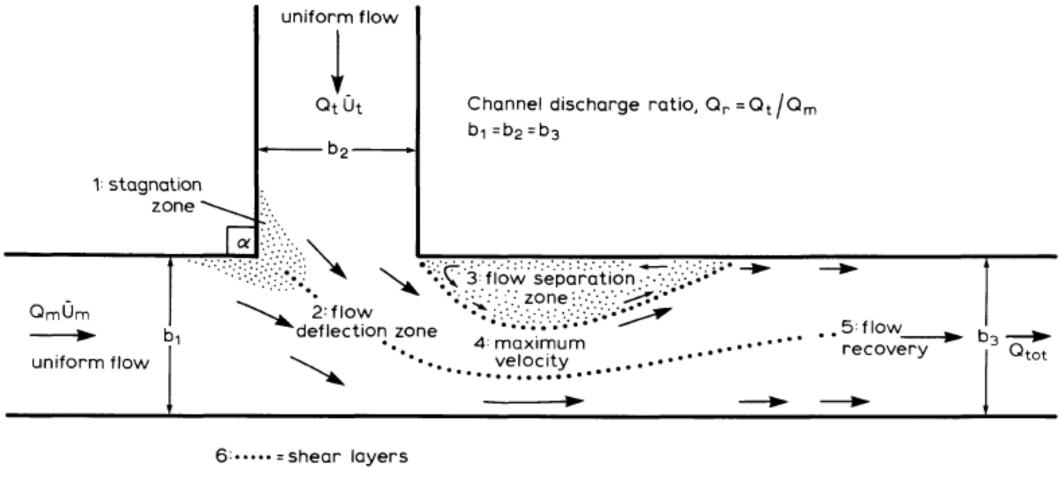

Figure 5. The conceptual model of open channel confluence [22]

Flow along the inner bank of the tributary (tributary left bank in Fig. 2.1.1) detaches at the downstream junction corner from the inner bank due to inertia effect, moves along a curved line towards downstream and finally re-attaches at the inner bank of the downstream main channel. Within the flow separation zone, some of the flow also moves towards upstream along the inner bank of the main channel.

Flow along the right bank of tributary and the left bank of main stream deflect towards the outer bank of the main channel due to the constraint between two streams, leading to the formation of stagnation zone.

Following that, a shear layer generates at the contact surface of tributary and main stream from the apex of stagnation zone and extends towards the outer bank (Figure 5). In fact, it is not a simple plane but a zone with a particular width, which is characterized by high velocity gradient, noticeable vortices, flow mixing (mixing layer) and down-welling flow [61] [59] [60] [52] [56] [46] [49] [1].

Due to the flow path squeezing from separation zone and the superposition of discharge from tributary and mean channel, flow accelerates in the middle of the confluence. This flow acceleration zone is characterized by secondary flow, maximum flow velocity and intensive scouring [61] [58] [52] [56] and is also the corridor of sediment transport [8] [30].

After the mixing between the tributary and main stream and the diminishment of the separation zone, the confluence cross-sectional flow field gradually recovers to that of a normal open channel. This is the flow recovery zone, where the turbulence level decreases and the secondary flow weakens [61] [59] [42].

2.2 Physical Model

2.2.1 Separation Zone

2.2.1.1 Size Variation in Space

The size of separation zone due to the variation of confluence angle and discharge ratio has been studied [6]. It is suggested in [6] that the variable “momentum ratio” is more useful than “discharge ratio”, because although the discharge ratio is an adequate measure of relative channel contributions in cases where channel width is invariable, the momentum ratio is universally applicable where the width of streams differs.

It was found that width and length of separation zone increase systematically with the confluence angle increasing from 30° to 90° and the momentum ratio increasing from 0.2 to 1.0 (Figure 6). This is because it is harder for the tributary flow to go parallel with the main stream flow and reattach to the inner bank as the confluence angle or momentum ratio increases. Moreover, it is evident that the predicted values [36] overestimate the width of the separation zone, and therefore underestimate the fraction of the channel occupied by the free stream [6] due to the inappropriate use of stream line theory (Figure 6).

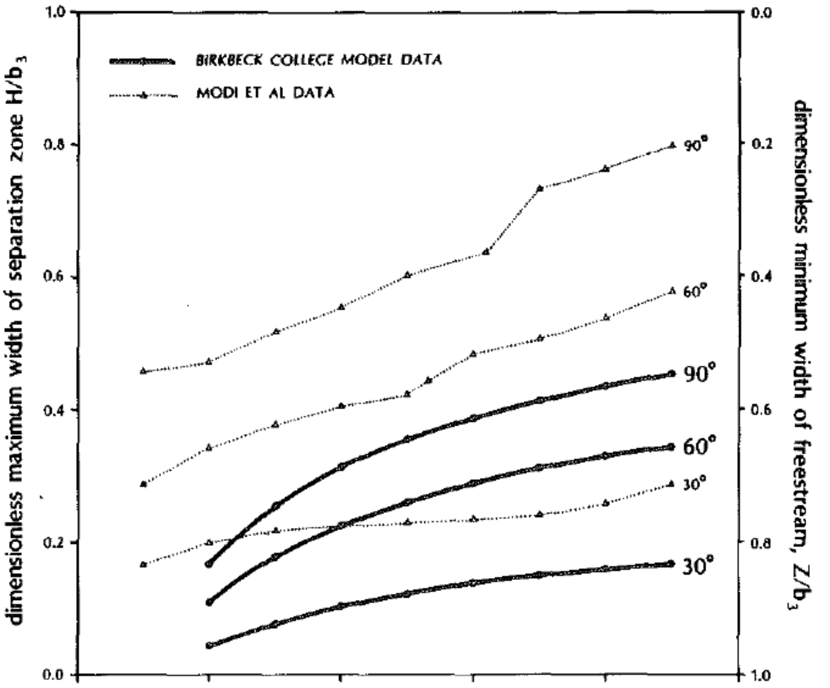

Figure 6. Maximum width of separation zone, H/b3, or minimum width of post-confluence combined stream flow, Z/b3, as a. function of discharge ratio, for 3 confluence angles [6].

A slight anomaly to this pattern is introduced by the 105° junction which at low discharge ratios has a smaller separation zone than either the 70° or 90° junctions [8] (Figure 7). It can be seen, however, that the rate of increase declines at higher discharge ratios where the effects of the confining far (outer) bank, together with pressure effects within the separation zone, become important.

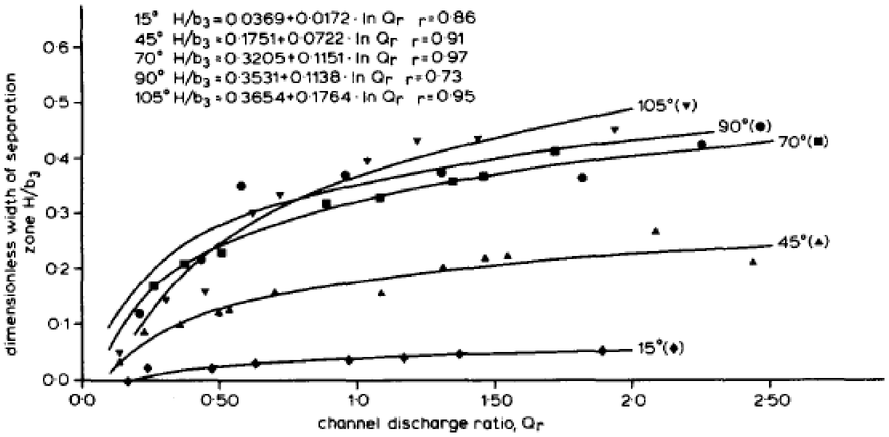

Figure 7. Plots of the dimensionless width of the separation zone, H/b3, against discharge ratio for five junction angles [8].

In contrast, it was discovered in [19] that the total area of separation zone decreases as the confluence angle decreases and reaches to its minimum value at the junction angle of 45° (Figure 8). It is reckoned that this is because when the confluence angle is very small, the tributary flow tends to go parallel with the main stream without deflection, reattaching only far downstream along the inner bank, which results in a longer separation zone.

Interestingly, the development of width is faster than that of length as the confluence angle or momentum ratio increases [6]. This may be because as the confluence angle or momentum ratio increases, it is much harder for the main stream to compress the tributary flow beside the separation zone due to the large momentum in the flow acceleration zone. At the same time, it is less difficult for the flow to reattach to the inner bank due to the smaller momentum in the flow recovery zone.

However, the size of separation zone is only measured at the water surface in [6]. It is observed in [34] that the size of the separation zone (both length and width) increases from the bed to water surface, primarily owing to the difference of the flow-in angle and velocity between the upper and lower layer at the tributary mouth. Consequently, tributary velocity lines at the confluence mouth are closer to the inner bank near the surface and closer to outer bank near the bed [20]. This agrees with the result in [61] [60] [56] [19] (Figure 9a) but contradicts with that of [58] [52] [49] [38] [40], in which the separation zone width increases dramatically from the bed up to about a quarter of flow depth and then remains constant (Figure 9b).

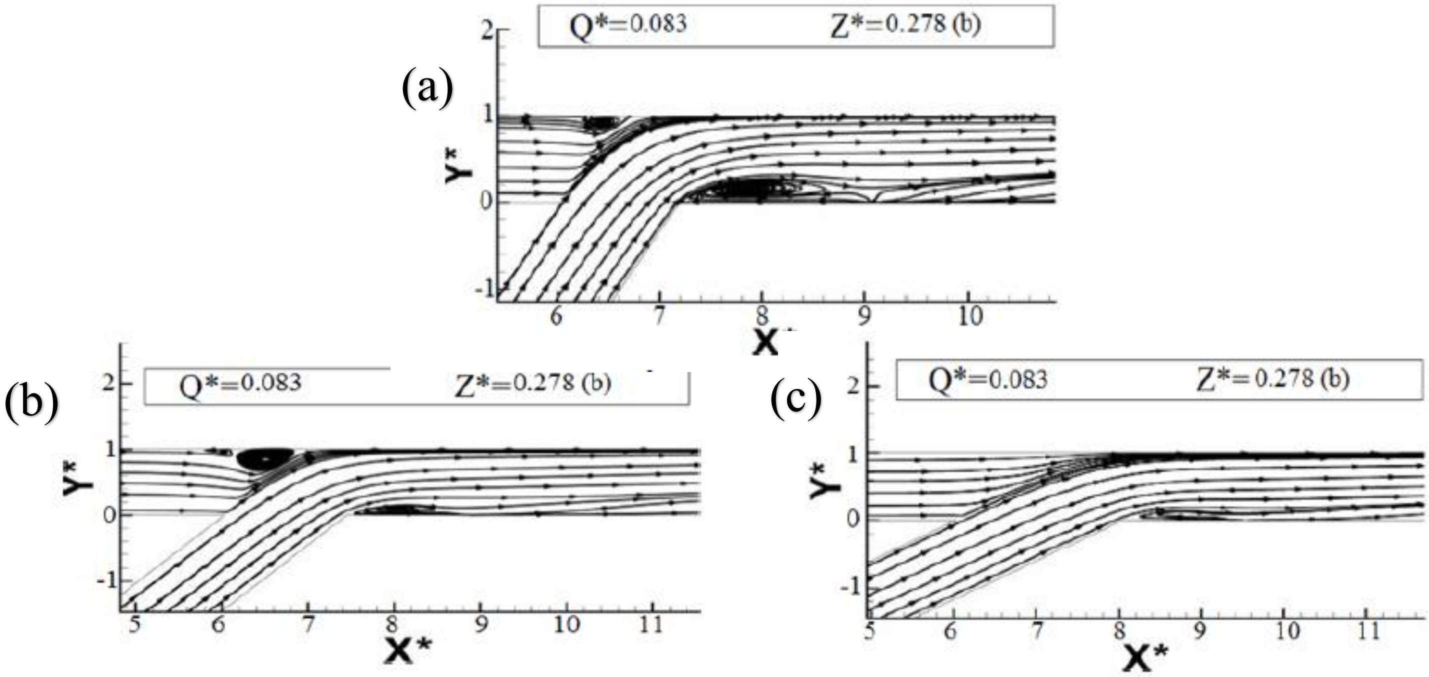

Figure 8. The streamlines for (a) 30°, (b) 45° and (c) 60° confluences at a discharge ratio (main stream/tributary) value of 0.083. [19]

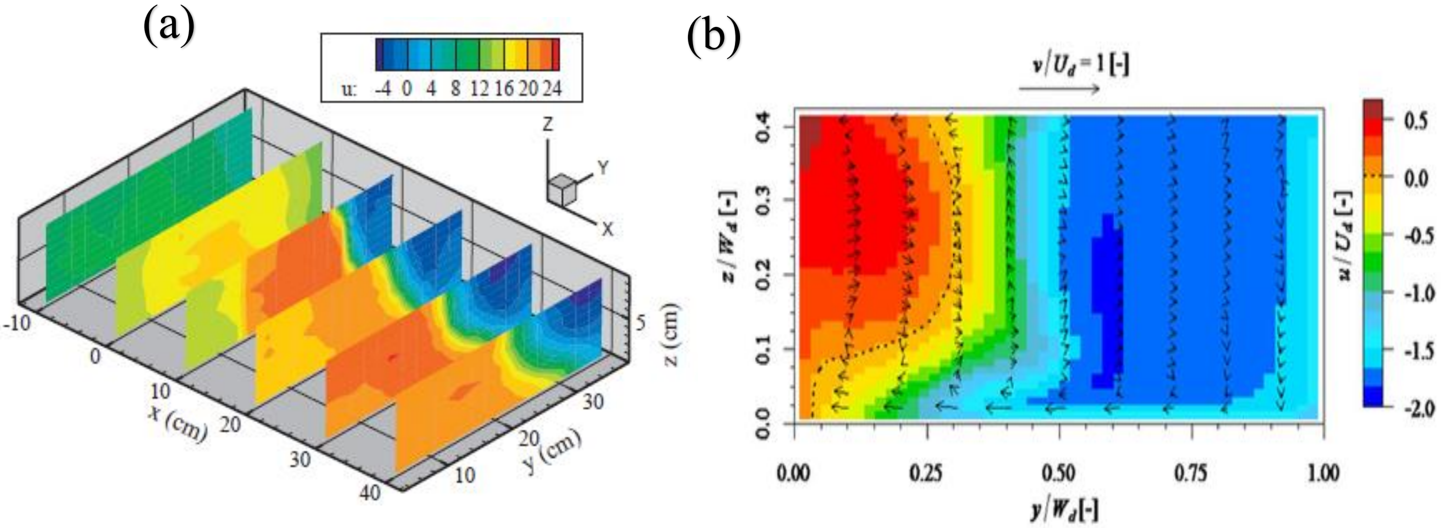

Figure 9. Variation of the separation zone size over depth (a) increase from the bed to flow surface uniformly [60] (b) increase dramatically then remain constant [49].

The separation zone near the bed could also be totally absent in some cases such as bed discordance, wherein the bed level of the tributary differs from that of the main channel. Flow in the deeper main channel is entrained from near the upstream junction comer into the flow separation zone in the lee of the step and routed towards the downstream junction comer [12], which diminishes the flow separation zone at the bottom. In addition, as the tributary flow goes into the confluence area, the flow beneath it tends to upwell (Figure 10) due to the compression effect. The separation zone near the bed is destroyed by fluid upwelling, nearer the water surface, where upwelling is less significant, a flow separation zone still exists [12].

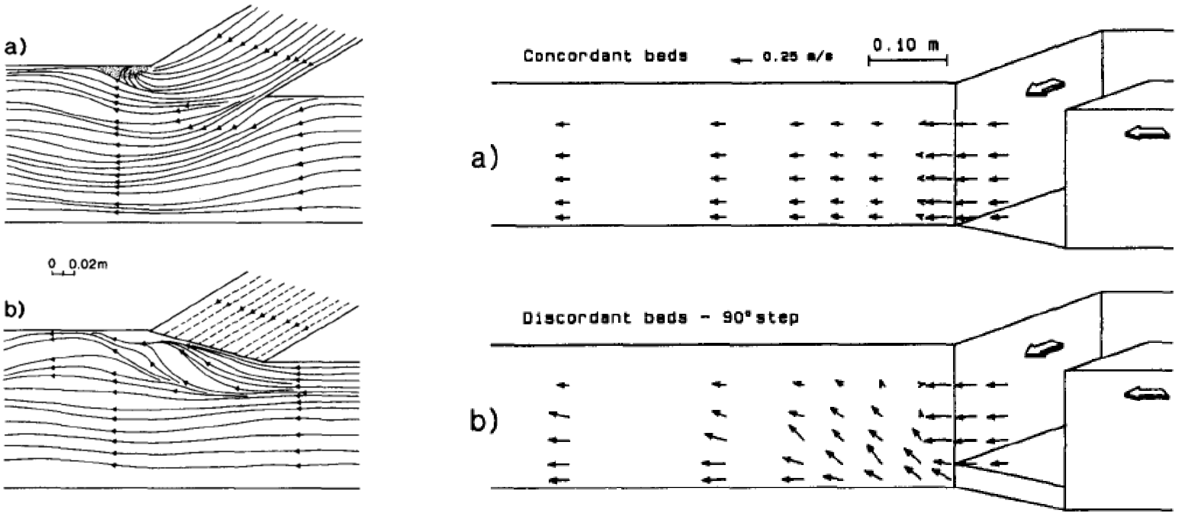

Figure 10. The streamlines near the bottom (Left figures) and velocity vectors near the inner bank of post-confluence (Right figures). (a) Concordant bed (b) Discordant bed [12].

2.2.1.2 The Separation Zone in Special Cases

The separation zone could also be found near the outer bank of the main channel under the circumstance of a symmetric straight channel or bend channel and also result in a dune [46] (Figure 11). The persistence of this dune in [46] contrasts with periodic erosion of the point dune at the confluent meander bend studied by [18], both high-angle confluences, but conforms to patterns of bed morphology typically found in meander bends [18]. The development of a dune at the downstream junction corner, which was documented previously at a high-angle confluent meander bend [45], also occurs at the high-angle confluent meander bend in [46], but not at the low-angle confluent meander bend due to the smaller size of separation zone.

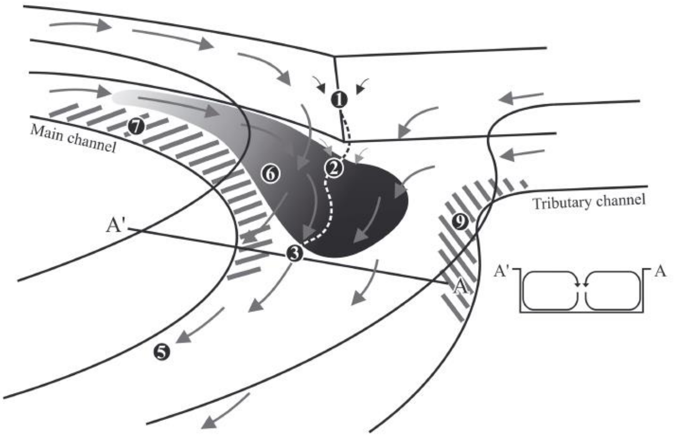

Figure 11. The bed morphology at a bend confluence (❾ and ❼ are the sedimentation zone) [46].

In addition, the size of the dune could be larger than the size of separation zone in some cases [46], suggesting that deposition of bedload related to patterns of decreasing bed shear stress downstream of the junction corner is primarily responsible for development of the dune [47] [10].

The main channel separation zone is also observed in [19] due to the extremely large discharge ratio (Q = 0.917) near the outer bank (Figure 12), which has a different formation mechanism compared with [46]. The main stream is nearly fully blocked by the enormous tributary flow rate. It can only enter the confluence zone through a slender passageway near the outer bank in the confluence zone. Flow along the inner bank of main stream deflects towards the outer bank at the mouth of confluence zone due to the obstruction of tributary flow and recirculates towards the upstream near the outer bank, which results in a separation zone. Similarly, the separation zone is found to have a spatial structure, which is larger near the bed and smaller near the flow surface [19]. It is reckoned that this is because the flow near the bed is easier to deflect and recirculate due to the smaller velocity.

A similar phenomenon could be seen at the left bank tributary due to the extremely small discharge ratio (Q=0.083) (Figure 13). It was found in [19] that flow near the inner bank in the main stream could detach from the bank and enter the tributary channel when the flow rate is low in the tributary. In this case, flow near the left bank

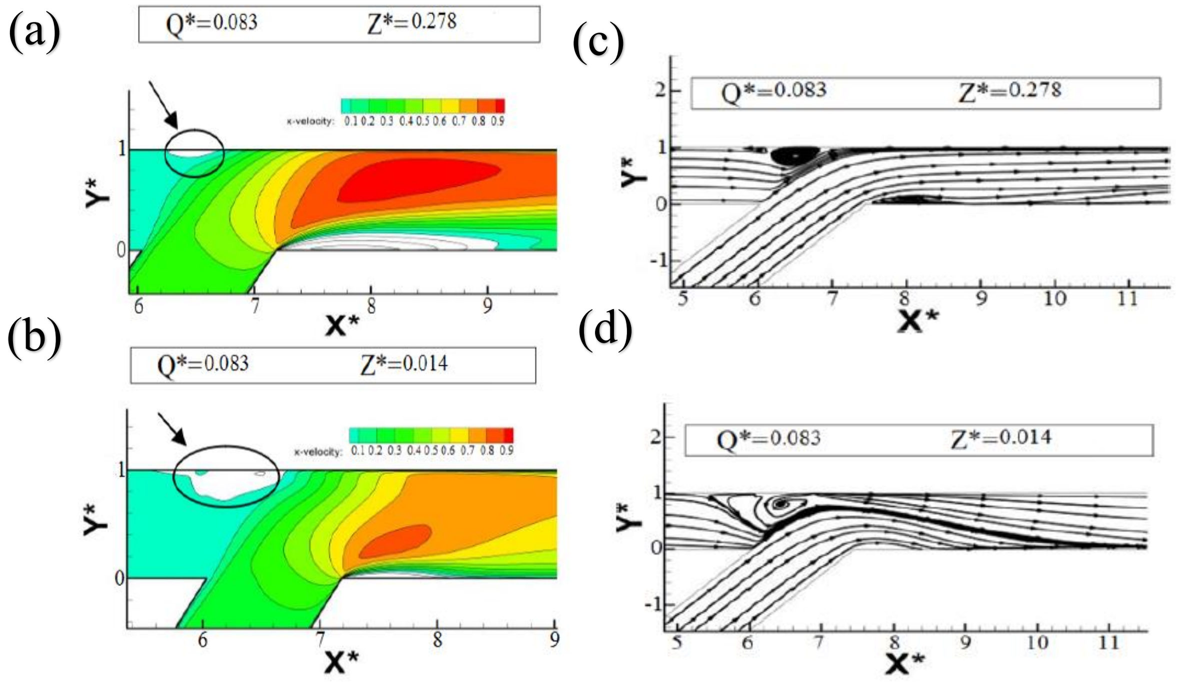

Figure 12. The flow field of a 45° confluence at a discharge ratio (main stream/Tributary) value of 0.083. (a)(b) Velocity contour map near flow surface and bottom. (c)(d) Streamlines near flow surface and bottom [19].

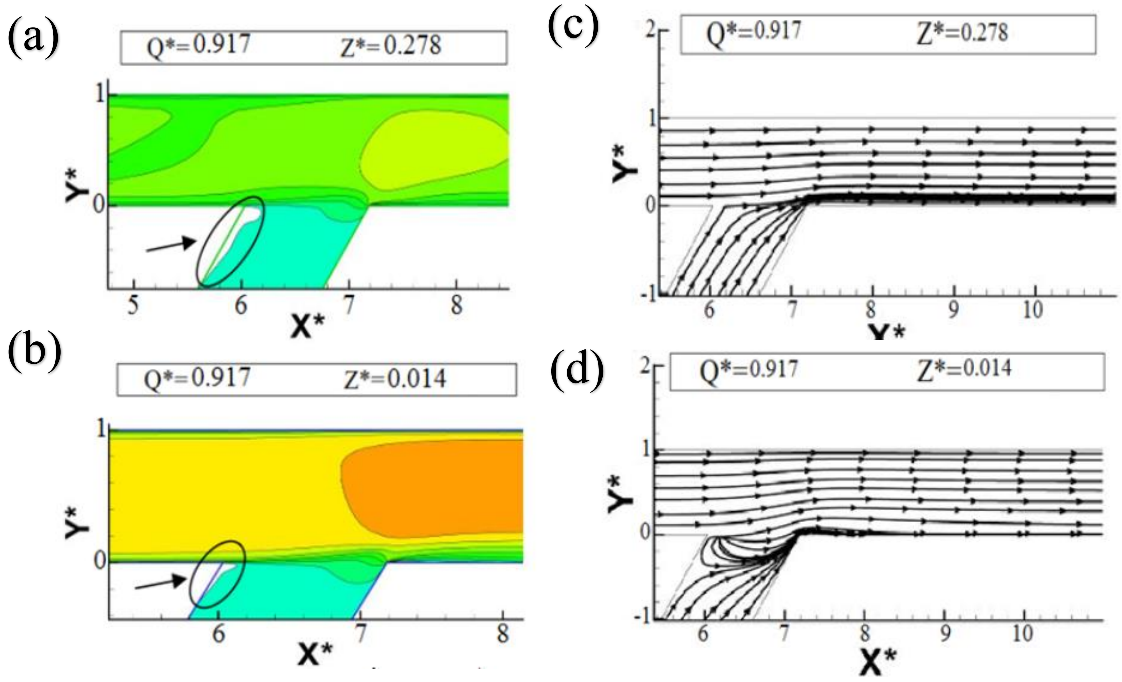

Figure 13. The flow field of a 60° confluence at a discharge ratio (main stream/tributary) value of 0.917 (a)(b) Velocity contour map near flow surface and bottom. (c)(d) Streamlines near flow surface and bottom [19].

of the tributary channel deflects towards the right bank (Figure 13d), resulting in the formation of separation zone. The spatial distribution of the separation zone is larger near the surface because the flow velocity is larger near the surface in the main stream, which makes it easier to go into the tributary for a longer distance.

2.2.2 Secondary Flow

Generally speaking, a secondary flow is generated in the flow acceleration zone [34] [58] [52] [46] and could be noted as the "tributary secondary flow" (The red vortex in outer side in Figure 14a).

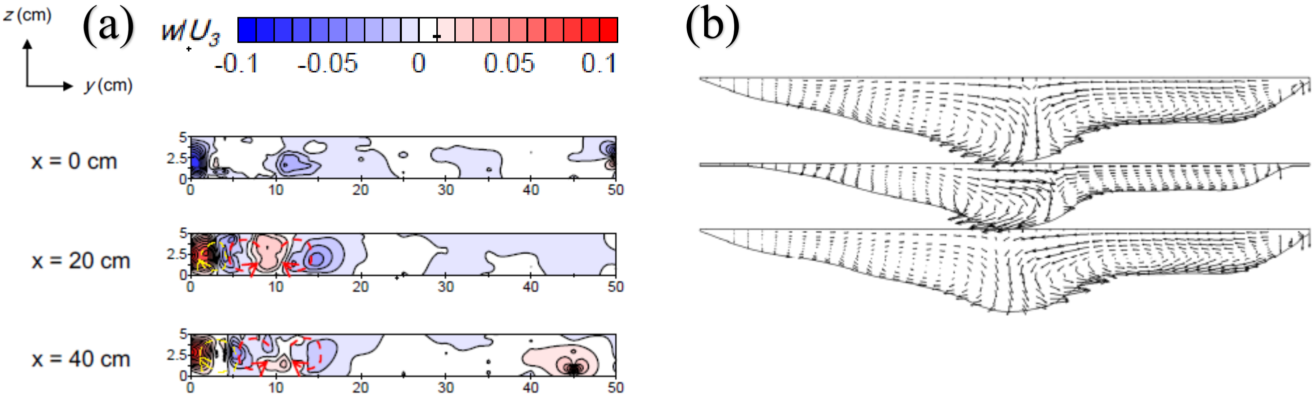

Figure 14. (a) The vertical velocity and secondary flow in yz-plane. The boundary between the separation zone and flow acceleration zone is at y=10cm. The red and yellow circles mark the secondary flow. (Modified after [58]) (b)The secondary flow in an open channel confluence with bend-shape tributary and mean channels under different discharge ratio conditions [4].

The mechanism can be explained as follows. Set the downstream flow direction as the x-axis positive direction. Set the cross-stream direction (pointed to the inner bank) as the y-axis positive direction. Set the vertical direction (upward) as the z-axis positive direction. The tributary flow will move a curved path through the confluence area, thus the centrifugal force is generated in the tributary stream due to the curved flow path. Due to the centrifugal effect, the flow surface in the outer side of the curve rises and the flow surface in the outer side of the curve drops, forming a flow surface transverse gradient. The streamwise velocity is larger near the flow surface while lower near the bed and the centrifugal force is proportional to the square of the streamwise flow velocity in the tributary flow. Therefore, the centrifugal force distribution along the z-axis also follows the same rule. The lateral pressure difference caused by the flow surface transverse gradient can be considered as constant along the z-axis. After the abovementioned two terms are combined, the force of the upper flow points to the outer bank while the force of the lower flow body points to the inner bank, causing the flow near the surface moving towards the outer bank while the flow near the bed moving towards the inner bank, generating a secondary flow along the inner side (tributary side) of shear layer. In addition, it is observed that the tributary secondary flow center usually moves along the shear layer, especially when the discharge ratio varies [58] [46].

Some bottom flow would penetrate into the separation zone, upwell and generate a secondary flow within the flow separation zone [34] [58] [49], which could be noted as the “separation secondary flow” (the yellow vortex in Figure 14a). Interestingly, an additional separation secondary flow was found in [58] (The red vortex near the yellow one in Figure 14a). However, the separation secondary flow is absent in [52] [46]. That is generally due to a small size of separation zone [52] or an experimental condition of low flow [46].

In addition, result in [4] witnesses a noticeable secondary flow from main channel and continue to exist in confluence zone due to the bend channel shape, which could be noted as the “main stream secondary flow”. It usually locates at the outer side of the shear layer, beside the tributary secondary flow [4] (Figure 14b).

The presence of secondary flow in the confluence is further validated through the bed surface phosphorus adsorption experiments in [60] and [56] (Figure 15). Due to the considerable downwelling flow and large velocity beside the upstream part of shear layer, the surface phosphorus concentration witnesses a peak value at that spot and decreases after that owing to the fading of secondary flow intensity.

In contrast, the main stream secondary flow is weak without a sand bed and sediment-feeding [61] [56] [60] [49] (Figure 9b). In some particular cases [52] [42], the main stream secondary flow no longer lies beside the tributary secondary flow but above it (Figure 16) resulting in distortion of the shear layer (Figure 17).

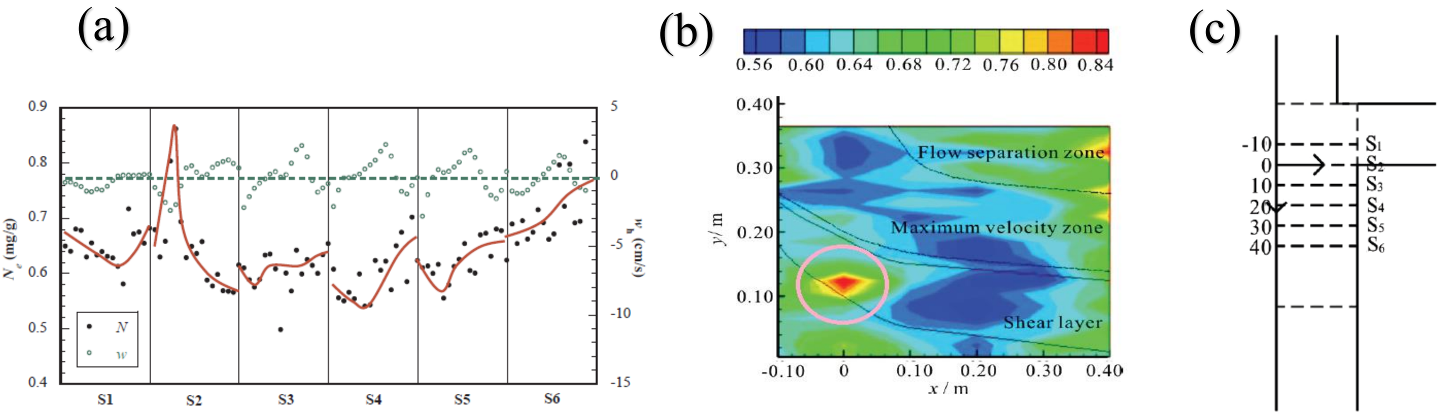

Figure 15. The bed surface phosphorus adsorption in confluence zone. (a) The concentration of phosphorus (black dots) in bed surface for different cross sections (the cyan dots stand for the vertical flow velocity) [60]. (b) A plan view for the concentration of phosphorus (pink circle marks the peak value) [56]. (c)a plan view for cross section set [60] [56].

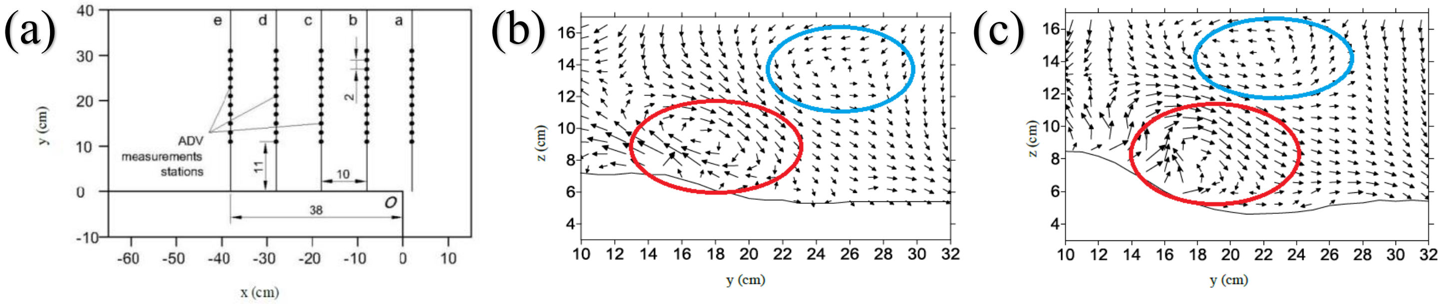

Figure 16. The stack position of two secondary flows at two downstream cross sections. The blue and red circle stands for the near-bed and near-surface secondary flow, respectively. (a) The cross sections for flow measurements; (b) The secondary flow at cross section 'd'; (c) The secondary flow at cross section 'e' (Modified after [42]).

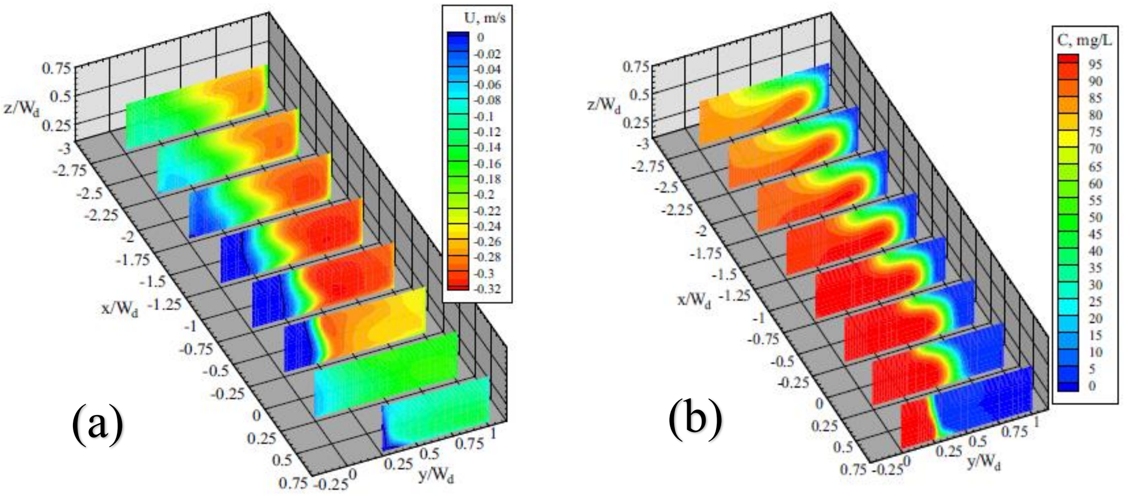

Figure 17. The distortion of (a) shear layer and (b) mixing layer [52].

2.2.3 Sedimentation and Erosion

The separation zone usually witnesses a noticeable sedimentation and formation of a bar, often attached to the downstream inner bank [34] [61] [62] [30] [52] [42] (Figure 18). This deposition zone may be a site for the preferred accumulation of heavy mineral grains [7]. The bar results from the secondary flow sediment entrainment near the bed beneath the flow acceleration zone (Figure 9b). The sediment that are eroded from the bed beneath the shear layer [61] or come from the tributary [30] move with the secondary flow at the flow acceleration zone. The secondary flow near the bed moves towards the inner bank beside the flow separation zone (Figure 16b) and brings sediment into the flow separation zone, where sediment tend to deposit due to the low flow rate [56].

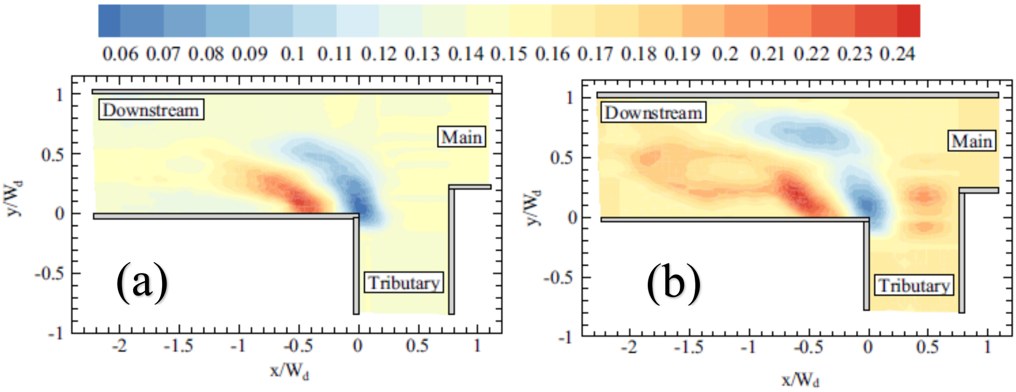

Figure 18. The typical sedimentation and scouring pattern at open channel confluence for different discharge ratios in flume experiment (a) Discharge ratio=2:3; (b) Discharge ratio=3:2. Note that the color bar stands for the elevation in unit of meter [52].

It is concluded in [20] that increasing discharge ratios would reduce the maximum height of deposition in the separation zone. Moreover, local tributary widening and lower value of gradation coefficient could enhance the morphologic gradient in the main channel by means of larger deposition [20].

Experiments conducted with poorly sorted sediment have shown that the face of the bar in the separation zone is covered by a mixture of coarse sediment, sorted such that the diameter increases from the top toward the toe of the bar [30]. This grain sorting can be explained by the balance of the upslope drag force and of the downslope gravitational force on the grains: the former scales with the square of the sediment particle diameter whereas the latter scales with the cube of the sediment particle diameter [50]. The similar result is observed both in [61] (Figure 19) and [30] (Figure 20).

In addition, the size of the bar could be larger than the size of separation zone in some cases [46], suggesting that deposition of bedload related to patterns of decreasing bed shear stress downstream of the junction corner is primarily responsible for development of the bar [47] [10].

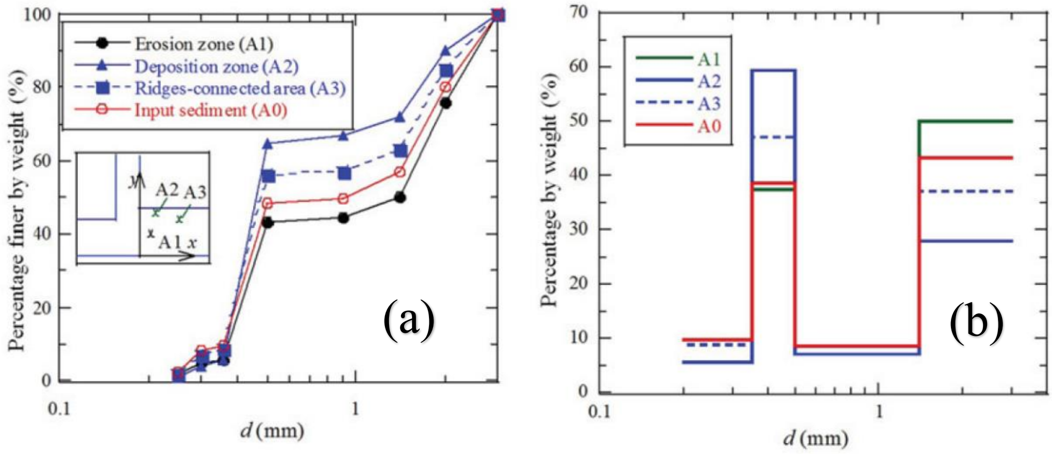

Figure 19. (a) Grain size distribution of samples measured by hand sieving and (b) mass fraction of a certain grain size range of surface sediment for different sample locations [61].

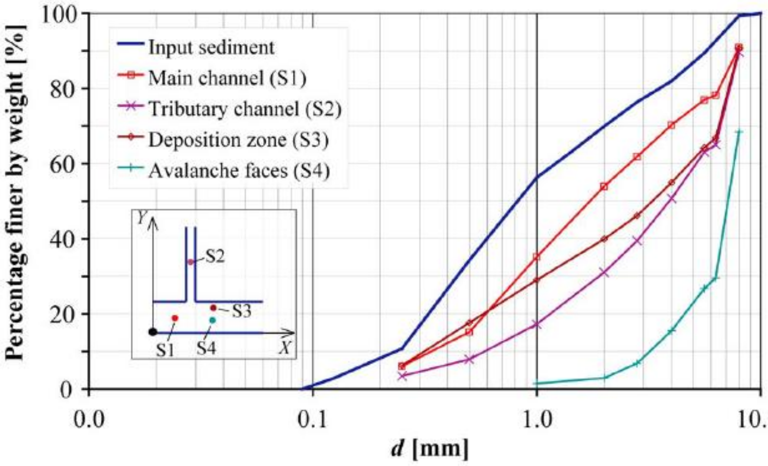

Figure 20. Grain size distribution of the input sediment and the different samples [30].

The bed morphology generated in [52] is characterized by a scour hole (Corner scour hole) located near the downstream junction corner (Figure 19a) when discharge ratio is low (2:3) and an additional scour hole (Shear scour hole) located beneath the shear layer when discharge ratio is high (3:2) (Figure 19b), which agrees with [61] [59] [60] [52] [42]. The corner scour hole and shear scour hole are attributed to the spiral vortices at the downstream junction corner [30], and the shear flow [8] developed from the upstream junction corner oriented approximately 30° with respect to the inner bank of the downstream channel, which agrees with [8].

In contrast, the bed morphology generated in [8] shows that a scour hole locates at the flow acceleration zone beneath the shear layer both in flume experiments and a real channel and spans from the stagnation zone to the foot of the separation zone bar (Figure 21), which agrees with [34] [46] [11]. It is considered in [8] that the shear layer, which is created between the two convergent flows, generates powerful vertical vortices. These are responsible for increased bed shear stresses within the junction which, together with the increase in velocity as both flows enter the confluence, are responsible for considerable bed scour [8]. However, [37] and [3] did not consider the mixing layer as a primary factor to the formation of the scour zone, rather that curvature-related helical cells were mainly responsible for scouring at confluences. The similarity of morphology between flume and natural channels not only demonstrates the validity of laboratory modelling but also enables the examination of factors that were effectively controlled in the flume, such as channel width adjustment and the effect of non-equilibrium bed conditions [8].

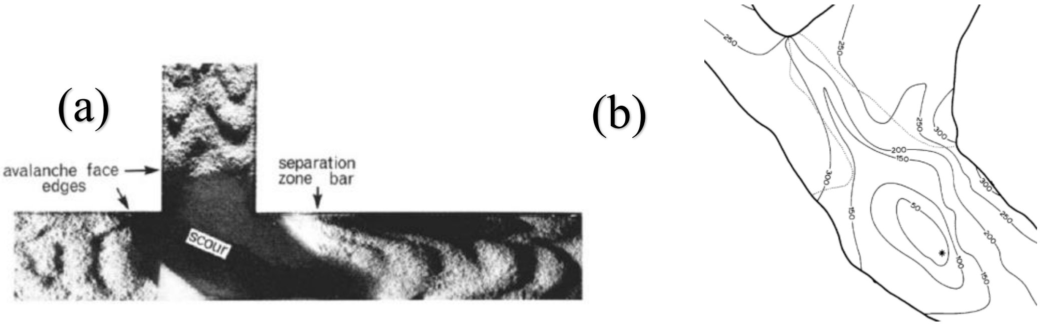

Figure 21. The bed morphology developed at 90˚confluence (a) flume experiment at a discharge ration of 1.05 (b) of Widdale Beck and the River Ure at Appersett, North Yorkshire. U.K. (Modified after [8]).

In addition, it could be seen that the shear scour hole is much more significant in higher discharge ratio than that in lower one [52] [11]. It is reckoned that flow generated from the tributary accelerates in the acceleration zone and the velocity becomes comparable with that of main stream under lower discharge ratio condition and becomes much larger than that of main stream under higher one, which results in a higher velocity gradient and severe shear stresses. Moreover, as the discharge ratio increases the shear scour hole tends to increase both in depth and size, approaching the outer bank, while the corner scour hole barely changes [42].

In conclusion, the formation mechanism of the scour hole is due to the increased bed shear stresses around the shear layer or helical cells. The absence of corner scour hole is due to the upstream sediment feeding in tributary (Figure 22). The sediment transport maps (Figure 22) indicate that little sediment is transported through the scour, but instead bedload from each confluent channel is transported around the side of the scour [8].

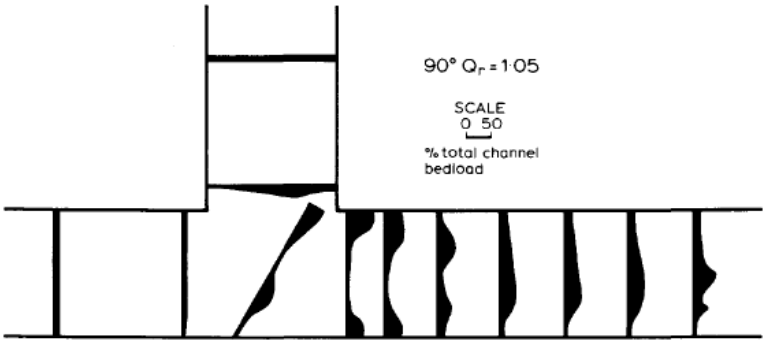

Figure 22. Map of total sediment transport distribution within the 90" confluence flume over a bed developed at a discharge ratio of 1.05. Sediment transport rates are expressed as the percentage of bedload passing a given cross section [8].

Nevertheless, scour holes have been reported to be absent in some cases such as bed discordance [30] [11] [37] [2] [5] [12] (although the minimum bed elevation in confluence area is slightly lower than that of the upstream main channel in [11] and [30]). The scouring observed in [11] is likely the result of local erosion due to the bank protrusion which constricts the flow in that zone. Moreover, it is also observed in [11] that the scour depth barely changes as the discharge ratio increases, suggesting these zones of local scouring differ from typical confluence scours. The reason for scour absence is studied in [12], where the bed discordance is shown to obliterate flow deflection at the bed and create a distortion of the mixing layer between the flows, resulting in fluid upwelling at the downstream junction corner [12]. This upwelling is responsible for the absence of a zone of marked flow acceleration in the post-confluence channel [12].

The confluence flume study by involved relatively low discharge and momentum flux ratios where a small steep tributary with a high supply of poorly sorted sediment joined a large, low-gradient main channel. The discharge ratio (tributary/main stream) was 0.11. The difference between the low-flow depth in the steep tributary and the higher flow depth in the main channel created a marked bed discordance in the tributary zone (Figure 23a).

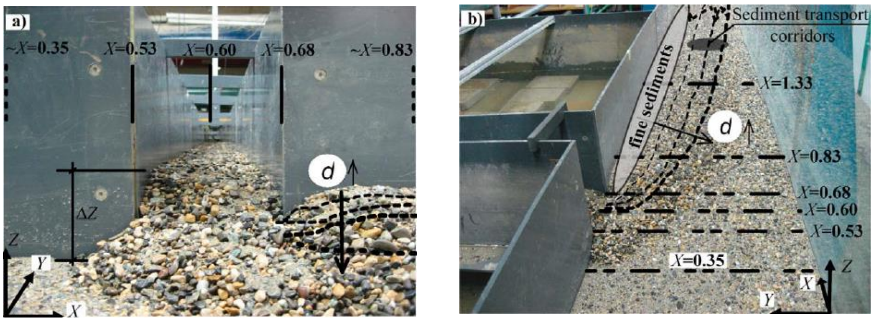

Figure 23. Equilibrium bed topography (a) looking up to the tributary channel from the tributary mouth (b) looking up at confluence area and post-confluence channels with constant sediment feeding from the tributary channel [30].

Under this circumstance, the bed morphology (Figure 24) generated in [30] is quite different from the general bed morphology generated from the flume studies under no-sediment-feeding condition (Figure 18). Sediment tends to deposit in the flow separation zone due to the relatively low flow rate and forms a bar gradually. The flow depth decreases in the post-confluence zone as the bar grows and the acceleration zone is also squeezed by the zone, which results in a much higher rise of the flow velocity and sediment transport. The sediment coming from the tributary could be transported much further and the bar also develops much wider and longer than the general case.

In addition, due to this bed discordance, the tributary flow penetrates into the main channel mainly in the upper part of the water column, whereas the main-channel flow is hardly hindered by the tributary in the lower part of the water column, giving rise to a two-layer flow structure in the confluence zone. This distinct two-layer flow structure superposes with the original flow structure and creates a complex flow field. The flow field is also constantly changing as the bed discordance level and sand bar evolve. It is worth further and deeper investigation and study.

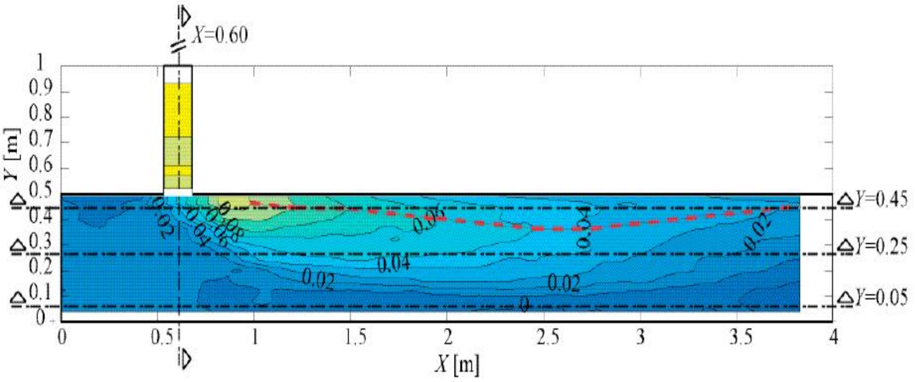

Figure 24. Equilibrium bed topography at the main and post-confluence channels with constant sediment feeding from the tributary channel. [30]

The three-dimensional flow structure and bed morphology for incoming flows with high and low momentum-flux ratios at two large, natural confluent meander bends that have different tributary entry angles were examined by [46] (Figure 25). It can be seen that the bed morphology developed in confluences with different junction angles have different deposition and erosion patterns. However, the reason is still unclear in this study because the sediment feeding changes with the discharge ratio, making it difficult to isolate the influence of these two factors.

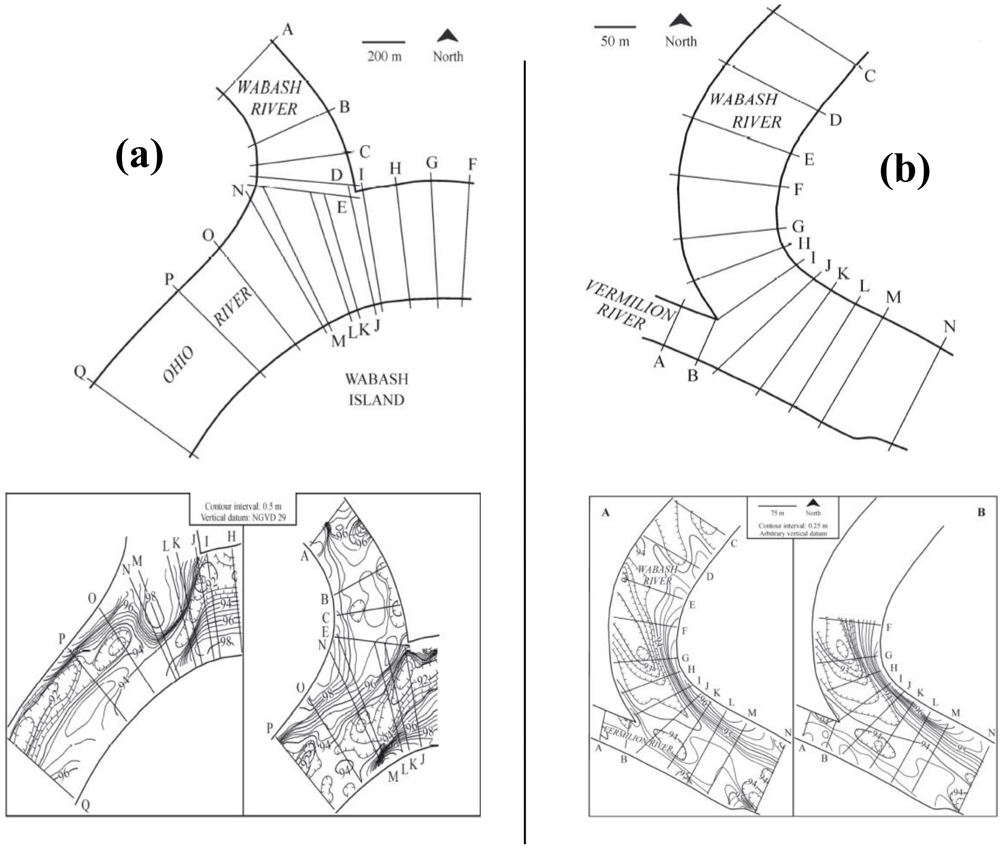

Figure 25. The bed morphology of 30° and 90° river confluences with different discharge ratios and sediment feeding condition. (a) the near-90° confluence; (b) the near-30° confluence. [46]

In a word, further study on the influence of discharge ratio and junction angle on open channel confluence flow field, bed morphology and sediment transport patterns needs to be done.

2.2.4 The Shear Layer

The center of the shear layer (or mixing layer) is defined as the location of maximum Reynolds stress, maximum velocity gradient [59] [35] and maximum turbulence level [59]. It is mentioned in [59] that the mixing layer would distort counterclockwise when looked from downstream due to the secondary flow (Figure 26).

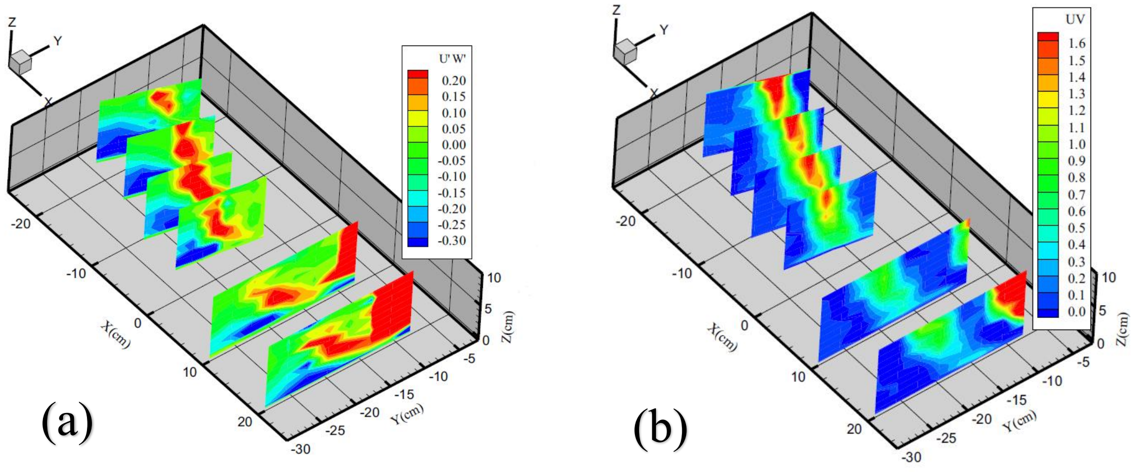

Figure 26. The contour map for the spatial distribution of Reynolds shear stress (a) <UW> and (b) <UV> (in units of cm^2/s^2) near the shear layer [59].

It is observed in [52] that the mixing layer tends to move towards the outer bank at first and then deflects towards the middle of the channel. The width of it increases as the flow advects downstream. This is because the flow compression is severe near the upper part of the mixing layer due to entry of tributary flow, but gradual mixing together of the two flows causes the velocity gradient to decrease. In addition, [48] and [52] showed that the mixing was slightly enhanced for a concordant bed as the discharge ratio increased.

The mixing pattern in a real river was evaluated in the study by [46] using temperature gradation (Figure 27). First, the term “momentum ratio” is defined as below:

$$M_r = \frac{\rho Q_2 U_2}{\rho Q_1 U_1} \tag{1}$$

Where ρ is fluid density (in kg/m^3), Q is discharge (in m^3/s), U is mean cross-sectional velocity (in m/s^{-1}), and the subscripts 1 and 2 refer to the main river and tributary (upstream river with the smallest drainage area), respectively. They investigated the potential for hand-held thermal infrared (TIR) imagery to provide rapid information on stream water mixing dynamics at small scales and compared with the water electrical conductivity and temperature data from cross-channel transects. They found that downstream momentum is advected laterally into the interface, especially for low momentum ratio, yet the temperature differential persists between the main river and tributary flow downstream of the confluence [46]. This lack of mixing between incoming flows, despite the existence of secondary flow, differs from findings at a small asymmetrical confluence where helical motion appears to distort the mixing interface and enhance mixing [48]. Moreover, it is concluded in [46] that the mixing interface at each site extends through the downstream channel, suggesting that mixing is limited and not greatly enhanced by lateral advection of momentum from helical motion within the confluence.

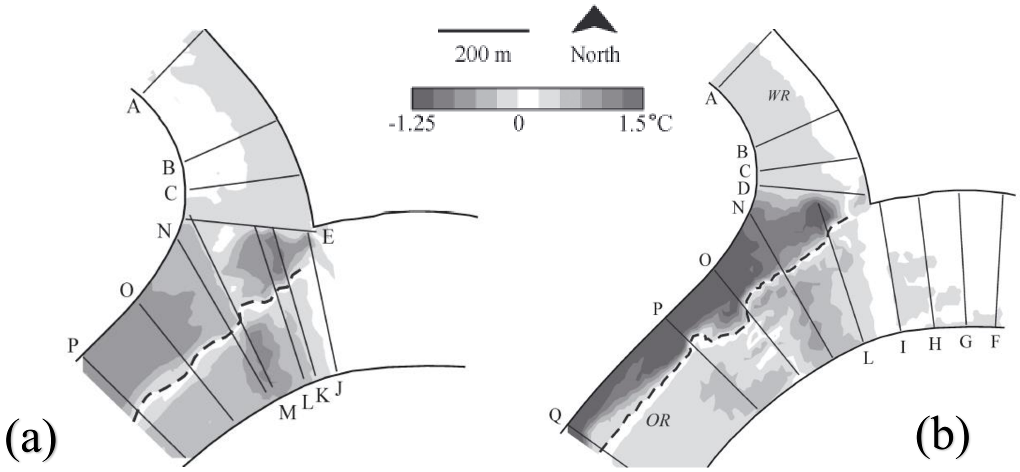

Figure 27. Deviation from mean water temperature near the surface at ORWR on (a) small discharge ratio and (b) large discharge ratio. Dashed line indicates approximate location of mixing interface [46].

2D Reynolds-Averaged-Navier–Stokes equations written in the so-called “Serret-Frenet local axis system” (terms include “s”, “n” and “b”) based on normal and tangential local mean velocity components were introduced by [35] to locate and characterize the shear layer. The Serret-Frenet coordinate system is based on the direction of the mean velocity at each point: “s” is directed along the mean velocity direction (i.e. along the streamline locally) and “n” is perpendicular to “s”, directed along the field lines towards the center of curvature [35]. This method could be used both in laboratory and field measurement, especially in regions where the angle between the mean flow velocity and the Cartesian frame-axis is large [35].

2.3 Numerical Modeling

While numerical modelling was not employed in this thesis, for completeness a few examples of numerical confluence models are reviewed briefly here.

2.3.1 Flow Field Simulation

A numerical simulation on the flow field for 90° open channel confluences using OpenFOAM was carried by [31]. The aim of this study was to evaluate the accuracy of different turbulence models, which include the Re-Normalization Group (RNG) k-ε model, the k-ω model and a Large Eddy Simulation (LES) model, compared to the experimental results. Not much difference was found in the performance of the RNG k-ε model and the k-ω model in predicting the vertical flow field (Figure 28). The k-ω model better predicted the range of the separation zone in both longitudinal and streamwise directions than the RNG k-ε model, but not necessarily the general shape of the separation zone (Figure 28a). Moreover, both the RNG k-ε model and the k-ω model's provided inadequate prediction of the vertical flow for the entire zone and the streamwise flow for the post-confluence zone.

Although the LES model showed better capability for capturing some unique details of the vertical flow field than the two-equation turbulence models, it could not do a better job in predicting the streamwise flow field, especially for the shape and the range of the separation flow. Quantitatively it was found that its separation zone was 20% shorter and more than 20% wider than in the physical model [31]. It is also clear that the LES model underestimated the velocities closer to the walls and bottom [31].

In conclusion, all three of these frequently-used turbulence models have their own flaws and work differently under different flow conditions. The LES model was meant to be more powerful to predict the eddies and secondary flow but proved to be overestimated, and the RNG k-ε model could be treated as the most accurate model among the three models.

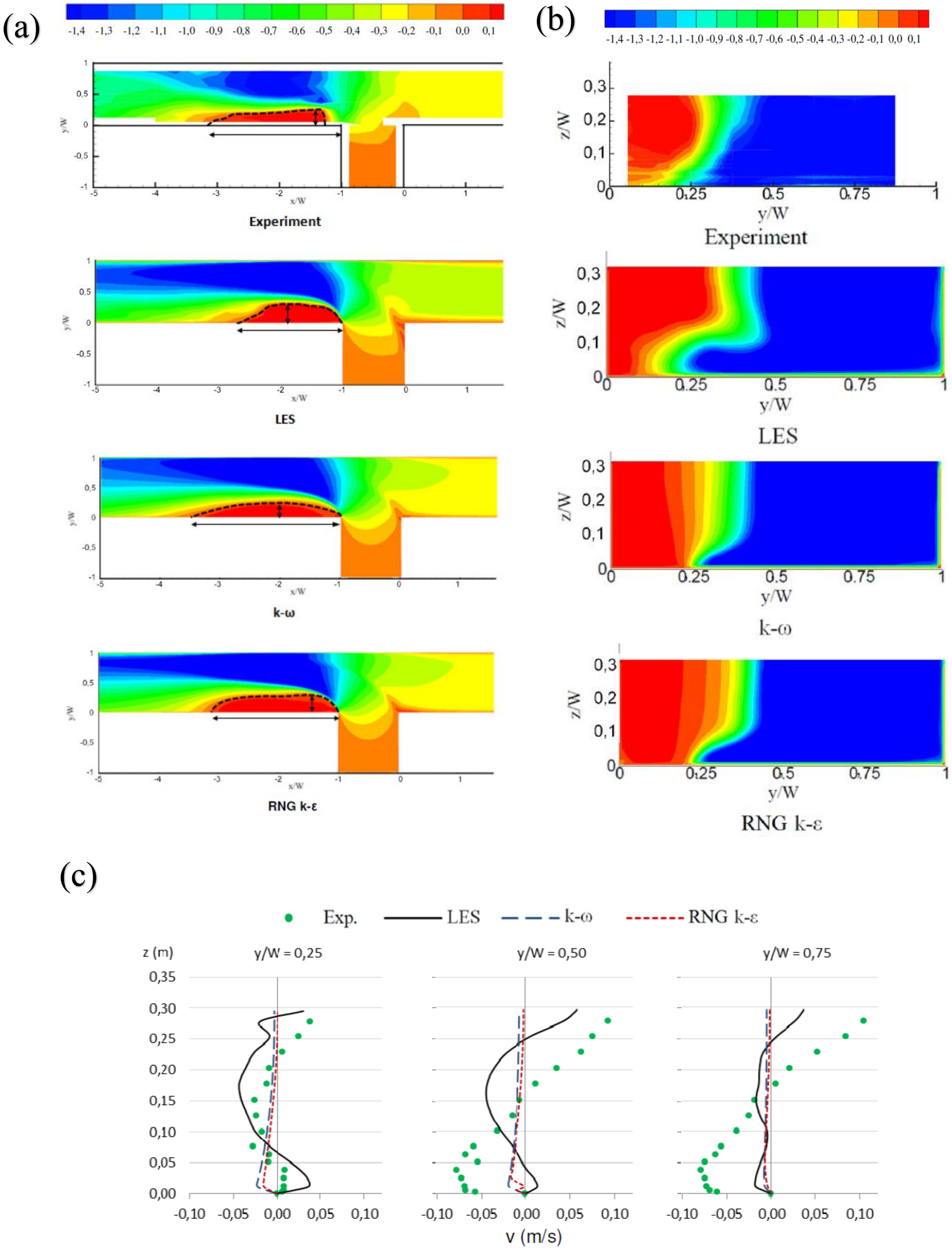

Figure 28. The velocity contour map for different numerical models (a) The plan view of streamwise velocity distribution at z/W = 0.014; (b) The cross section of streamwise velocity distribution at x/W = -1.67; (c) Vertical profile of lateral velocities at x/W =-6 [31]. Note that

the flow velocity unit is m/s.

2.3.2 Free Surface Simulation

One of the characteristics of open channel flow is the free surface. In the case of open channel confluence flow, the variation of flow surface in the separation zone and the flow depth ratio between the upstream of main stream and the confluence zone due to the back water effect at the mouth of confluence are pronounced in some particular cases. Following that, several free surface simulation methods are raised such as the static pressure assumption method, elevation function method, grid method, volume of fluid method (VOF), level set method, ghost fluid method etc.

The VOF method is characterized by defining the movable interface as a fluid volume function in the spatial grid and constructing a development equation for this fluid volume function. The interface tracking problem is converted to determine, with the simulation of the primary flow field and transport, the location of the movement interface, shape and deformation direction.

A fixed channel confluence with a right angle was considered by [58]. Numerical analyses by a large eddy simulation (LES) with the Volume of Fluid (VOF) method capable of treating the free surface boundary were performed to investigate three-dimensional structure of turbulent flow and water surface variations at the confluence. In this study, the Volume of Fluid (VOF) method implemented in FFB, which is a LES code generated, developed and validated in “Research and Development of Innovative Simulation Software” project sponsored by the Ministry of Education, Culture, Sports, Science and Technology (MEXT) of Japan [29], was used to capture the free surface interface with a high-accuracy. In VOF, to describe the evolution of free surface, an advection equation of volume fraction is employed. The VOF equation is given by:

$$\frac{\partial \alpha}{\partial t} + \frac{\partial \alpha \overline{u_i}}{\partial x_i} = 0 \tag{2}$$

Where α is the volume fraction and can be defined as:

$$\overline{\alpha} = \frac{\alpha - \alpha_U}{\alpha_A - \alpha_U} \tag{3}$$

Where the subscripts U and A denote the upwind and acceptor element, respectively.

Since the water depths of this study were measured using a scale and there were only three measurement points along each cross section (along the left bank, at the mid channel and along the right bank), the measurement accuracy is not sufficient to compare strictly with the numerical results. It is one of the shortcomings in this study. In addition, incoming tributary flow squeezes the flow path of mean stream and may cause a slightly rise of upstream water level [30] [58], which could also be observed according to the experiment results (the black circle in Figure 29). However, that zone could not be seen in the LES results, which makes the flow field generated from the model lack fidelity.

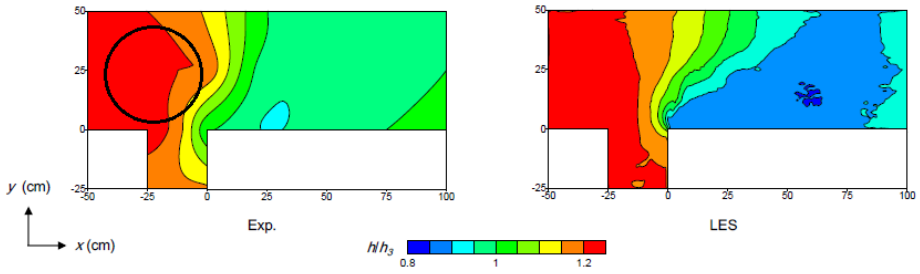

(a) Case T_0.5

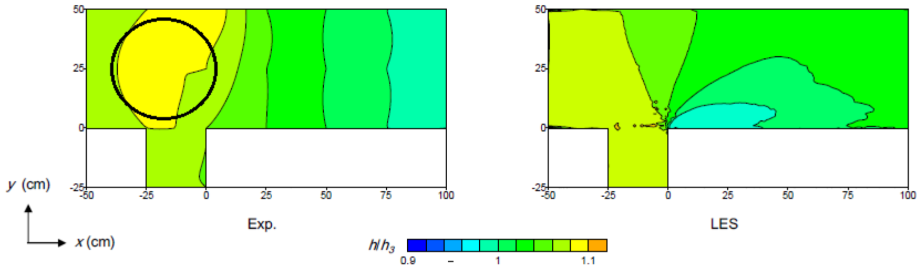

(b) Case T_2.0

Figure 29. Comparison of mean water depth distribution. Experiment results are shown on the left column while the LES results are shown on the right column. (a) ‘T_2.0’ and (b) ‘T_0.5’ stand for the discharge ratio (main stream/tributary) value of 2.0 and 0.5, respectively (Modified after [58]).

2.4 Conclusion

The study on open channel confluence flow and morphodynamics is of great importance to predict the sediment transport and channel evolution patterns. However, the interaction between flow, sediment and the bed morphology is quite complex and with many relevant variables, which makes it challenging to apply experimental results to real river cases. Moreover, numerical models cannot yet simulate the open channel confluence precisely for application to all confluence flow conditions.

Still, the recent open channel confluence studies have many agreements and similar results, which are listed below:

- There are several flow zones and layers in an open channel confluence characterized by different flow patterns: the separation zone, the flow acceleration zone, the shear layer, the stagnation zone and the flow recovery zone.
- The separation zone usually witnesses a low flow rate, a re-circulation flow in horizontal plane and sometimes a secondary flow in cross-sectional plane. The size of separation zone increases from the bed to the free surface and increases as the discharge ratio (tributary stream/mean stream) and the junction angle increases. Significant sedimentation also occurs in this zone and form into a bar. The size of the bar is usually bigger than that of the separation zone. The sediment on the face of the bar are sorted as coarse to fine from the toe to the top of the bar.
- The shear layer is characterized by large streamwise flow velocity gradient and Reynolds shear stress. Downwelling flow takes place in this layer and results in deposition of heavier sediment. The shape of the shear layer can be distorted by the secondary flow as the flow moves towards the downstream.
- The flow acceleration zone has the maximum level of flow velocity and secondary flow. A scour hole usually is located in this area. The size and shape of the scour hole may vary as the discharge ratio and junction angle changes.

There were also different results observed and problems remain to be solved in recent studies on open channel confluences, which are also listed below:

- The secondary flow pattern in the flow acceleration zone differs between flume experiments. It could be two secondary flow cells lying up and above the flow separated by the shear layer. It also could be only one secondary flow cell. The reason is still unclear in most studies.
- Most flume experiment cases are carried out under no-morphology and no sediment feeding conditions. Furthermore, the flume experiment cases with developed morphology and the real river case share little similarities. There has yet to be a physical model which could simulate the case in real river confluence and summarize the general pattern.
- The location and range of the scour hole is quite different under sediment feeding and no-feeding conditions. And there is no scour hole observed in one flume experiment case with sediment feeding from the tributary.
- The generation of the scour hole is attributed to the secondary flow in some studies while from the high flow velocity in some others. The generation mechanism remains to be solved.
- The two variables, discharge ratio and junction angle, which mainly affect the confluence flow and morphodynamics, haven’t been studied systematically under the presence of bed morphology and sediment feeding.
- The bed load sediment transport and bed morphology under nine flow conditions was studied by [15] based on near-bed velocity and stresses. However, the flow field measurement was only taken near bed and there were only 5~6 sample points for each cross section near the shear layer zone. The lack of flow field data did not allow for a solid discussion of the morphodynamic mechanisms.

Chapter 3 Objectives

This study is inspired by the studies of [61], [30] and [19]: [61] studied the flow and morphology features under different discharge ratios in a 90° confluence flume; [19] focused on the variation of flow path in confluence flumes with different junction angles but no morphology condition; [30] introduced constant feeding of sediment into the tributary channel and studied the equilibrium morphology state in a 90° confluence flume. However, there was no sediment feeding in [61], and [30] and [19] did not have a proper initial bed morphology state. In addition, each abovementioned study only focused on one variable (discharge ratio, junction angle, sediment feeding) that may affect the confluence flow separately. No research has been done with all the three factors together and initial bed morphology states.

This study is the first to examine the flow field, bed morphology and sediment transport patterns under different discharge ratio, junction angle and sediment feeding conditions. The study is conducted by means of flume experiments. By introducing additional sediment in the tributary, this study attempts to model real cases of sediment delivery from the tributary. It is recognized that such sediment in field conditions could possibly be contaminated, thus this study allows for assessment of fate and transport of contaminants from a tributary to a main channel. Sediment feeding conditions that may affect the sedimentation pattern are systematically considered, including the feeding location, the feeding amount and the sedimentation pattern evolution after feeding. The objective of this study is to find the similarities and differences of sedimentation pattern under different flow and sediment feeding conditions and to try to explain the mechanism by studying the flow field. Note that the flow field investigation in this study only serves as a tool for explaining the sedimentation pattern. Other subjects concerning the flow field such as the size of flow separation zone and the distortion of shear layer are not the primary foci of the study.

Chapter 4 Methodology

4.1 Experiment Setup

4.1.1 Flume Setup

The confluence flume setup and parameters are shown in Figure 30. A flume with a modifiable junction angle was used in this study, which allows for isolation and evaluation of key variables. The wall and the bottom of the flume used the same material of PMMA (Polymethyl methacrylate) in order to have a clear sight inside and avoid excessive deformation due to environmental temperature and air pressure.

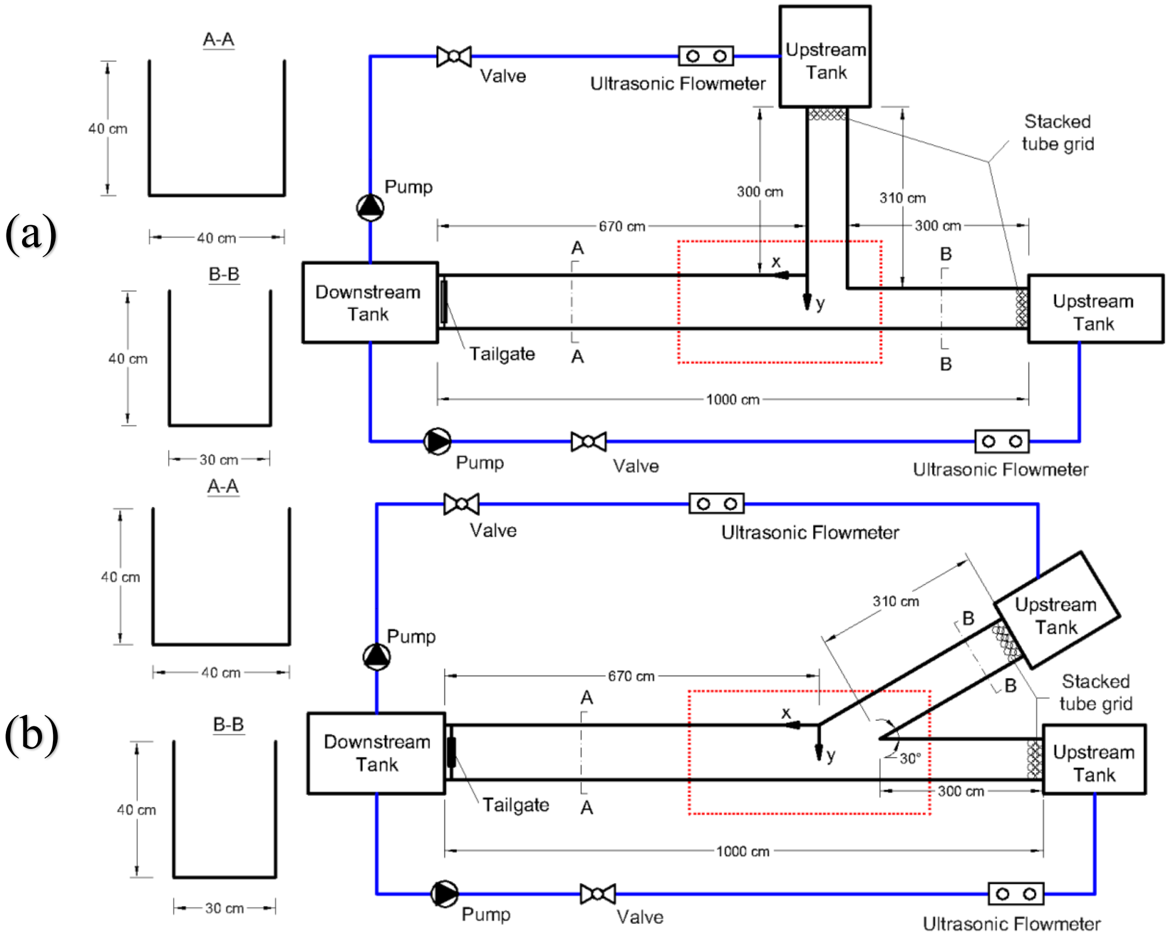

Figure 30. The sketch for confluence flumes setup and parameters. The blue lines stand for the pipeline system. The red area stands for the test area. A-A and B-B are the cross section view for downstream and upstream (both the tributary and main channel) respectively. (a) 90° confluence flume; (b) 30° confluence flume. (Note: The sketch drawing is not to scale)

The water was pumped out from the bottom of the downstream tank into two tubes (blue lines in Figure 30) extending to the upstream tanks by the pumps. The two pumps had the same fixed working load of 30L/s and the working load could not be adjusted once turned on. The flow discharge inside the tube could be adjusted by the wheel-handle valve which was connected to a water gate inside the tube. The flow discharge inside the tube could be detected by the ultrasonic flowmeter and read on the monitor of the terminal. The outlets of the tubes were at the bottom of the tank to make sure the water goes into the flume by free overflow, which could stabilize the upstream flow state.

Two stacked tube grids (Figure 31) were set at the outlet of upstream tanks. The grid was manufactured using equally sized PVC tubes. Tubes were glued together to form a grid layer. Adjacent layers were close packed and also glued together. The parallel stacked structure was used to stabilize the flow. The grid was designed to be a rectangular shape with the same width of the flume and 5cm higher than the flow depth in order to make sure the whole flow field is stabilized by the grid. The test area (Red dots in Figure 30) was about 250cm away from the upstream tank outlet in order to have steady flow at the entrances to the test area. The flow depth could be adjusted by the tailgate at the inlet of downstream tank.

Figure 31. The picture of stacked tube grid.

The height of the flume walls was 40 cm and the width was 30 cm for upstream channels and 40 cm for the downstream channel. The design of different width used in the flume was to mimic real river cases. The upstream junction corner was 310 cm away from the outlet of upstream tanks and the downstream junction corner was 670 cm away from the inlet of the downstream tank.

4.1.2 Flow, Bed and Sediment Condition

The flume experiment was carried out under two discharge ratio 3:2 and 2:3 in two confluences with the junction angle of 90° and 30°, which made it four cases in total. They were tagged as “90_3_2”, “90_2_3”, “30_3_2” and “30_2_3” separately based on the junction angle and discharge ratio. The initial bed elevation and flow depth were the same for all cases (Table 1).

Table 1. The hydraulic data of different flow cases.

Case No.	Junction Angle, θ (°)	Discharge Ratio, $Q_r = Q_t / Q_m$	Initial Bed Surface Elevation, h_0 (m)	Flow Surface Elevation, h_1 (m)	Flow Depth, Δh (m)	Upstream Flume Width, W_u (m)	Downstream Flume Width, W_d (m)	Hydraulic Gradient, J(%)
90_3_2	90	3:2	0.06	0.22	0.16	0.30	0.40	0.04
90_2_3		2:3						
30_3_2	30	3:2						
30_2_3		2:3						

Case No.	Discharge Rate, Q (L/s)			Reynolds Number, Re			Froude Number, Fr		
	Tributary Channel, Q_t	main channel, Q_m	Downstream Channel, Q_d	Tributary Channel, Re_t	main channel, Re_m	Downstream Channel, Re_d	Tributary Channel, Fr_t	main channel, Fr_m	Downstream Channel, Fr_d
90_3_2	9.00	6.00	15.00	15000	10000	21429	0.16	0.11	0.21
90_2_3	6.00	9.00		10000	15000		0.11	0.16	
30_3_2	12.00	9.00	21.00	20000	15000	30000	0.22	0.16	0.29
30_2_3	8.78	12.73	21.51	15000	14633	30729	0.16	0.23	0.30

The pre-test had shown that there was no change in the bed morphology after 24h’s scouring in 30° confluence flume when using the same discharge ratio and discharge rate as that of 90° confluence flume. Because the size of the separation zone in 30° confluence flume was much smaller than that in 90°confluence flume based on previous studies [8] [6] [19], which caused the intensity of flow acceleration and secondary flow to be much weaker to form a scour hole. In order to study the junction angle effect on confluence flow and morphology only, the discharge ratio should be kept the same. So the total discharge rate was raised in 30° confluence flume. It was raised to a state under where the maximum depth of scour hole developed in 30° confluence flume was equal to that of 90° confluence with the same discharge ratio in order to avoid additional variables (Table 1).

The test area was the area set for flow field measurements, bed morphology developments and sediment transport observation. The parameters and bed condition of test area is shown in Figure 32. The bed area (The yellow area in Figure 32) was filled with natural sands excavated from the real river, which ensured the natural grain shape and poor grain size gradation (Table 2 and Figure 33). The initial bed morphology was set to be flat with a thickness of 6 cm. The width of the bed area was 40cm for downstream channel and 30 cm for upstream channels. The bed area in downstream channel was smaller in 30° confluence channel than that in 90° confluence channel due to the smaller range of morphology variation in 30° confluence channel.

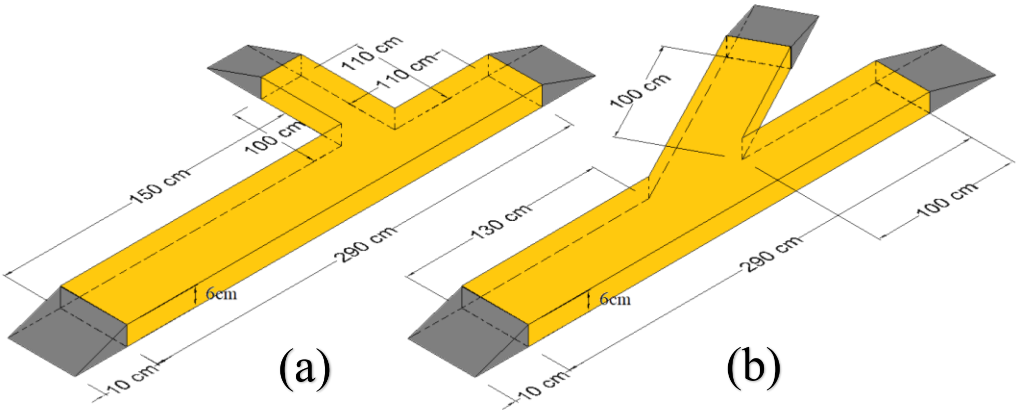

Figure 32. The sketch for the test area parameters and bed condition. (a) The 90° confluence flume; (b) The 30° confluence flume. (Note: The sketch drawing is not to scale)

Table 2. The sieve analysis results for the bed sand. The values of D_{25}, D_{50}, D_{75}, D_{90} and sorting coefficient are calculated from the fitted curve in Figure 33.

Sieve Pore Size, d/mm	Sieve Weight, M_1/g	Sieve and passing Weight, M_2/g	Net Passing Weight, ΔM/g	Percentage of Total, η_1	Percentage of Grains Smaller Than the Sieve Pore Size, η_2
1.6	252.71	255.67	2.96	0.0099	0.9901
1.43	263.06	270.41	7.35	0.0247	0.9654
1.25	269.76	273.93	4.17	0.0140	0.9513
1	260.18	263.14	2.96	0.0099	0.9414
0.9	253.38	255.03	1.65	0.0055	0.9358
0.8	254.73	266.23	11.50	0.0386	0.8972
0.71	253.10	258.50	5.40	0.0181	0.8790
0.45	250.11	295.90	45.79	0.1539	0.7252
0.355	259.23	303.76	44.53	0.1497	0.5755
0.2	246.48	364.63	118.15	0.3971	0.1784
0.095	252.55	301.15	48.60	0.1633	0.0151
0.088	254.37	256.75	2.38	0.0080	0.0071
0.074	257.05	257.51	0.46	0.0015	0.0055
0.057	248.47	248.94	0.47	0.0016	0.0040
0.045	243.23	243.91	0.68	0.0023	0.0017
0.038	248.84	249.09	0.25	0.0008	0.0008
0	237.46	237.71	0.25	0.0008	0
Sample Weight After Gradation Test) W/g			297.55	D_{25} /mm	0.21
				D_{50} /mm	0.32
Original Sample Weight W0/g			301.23	D_{75} /mm	0.47
				D_{90} /mm	0.80
Error, E			0.01	Sorting Coefficient (So)	2.23

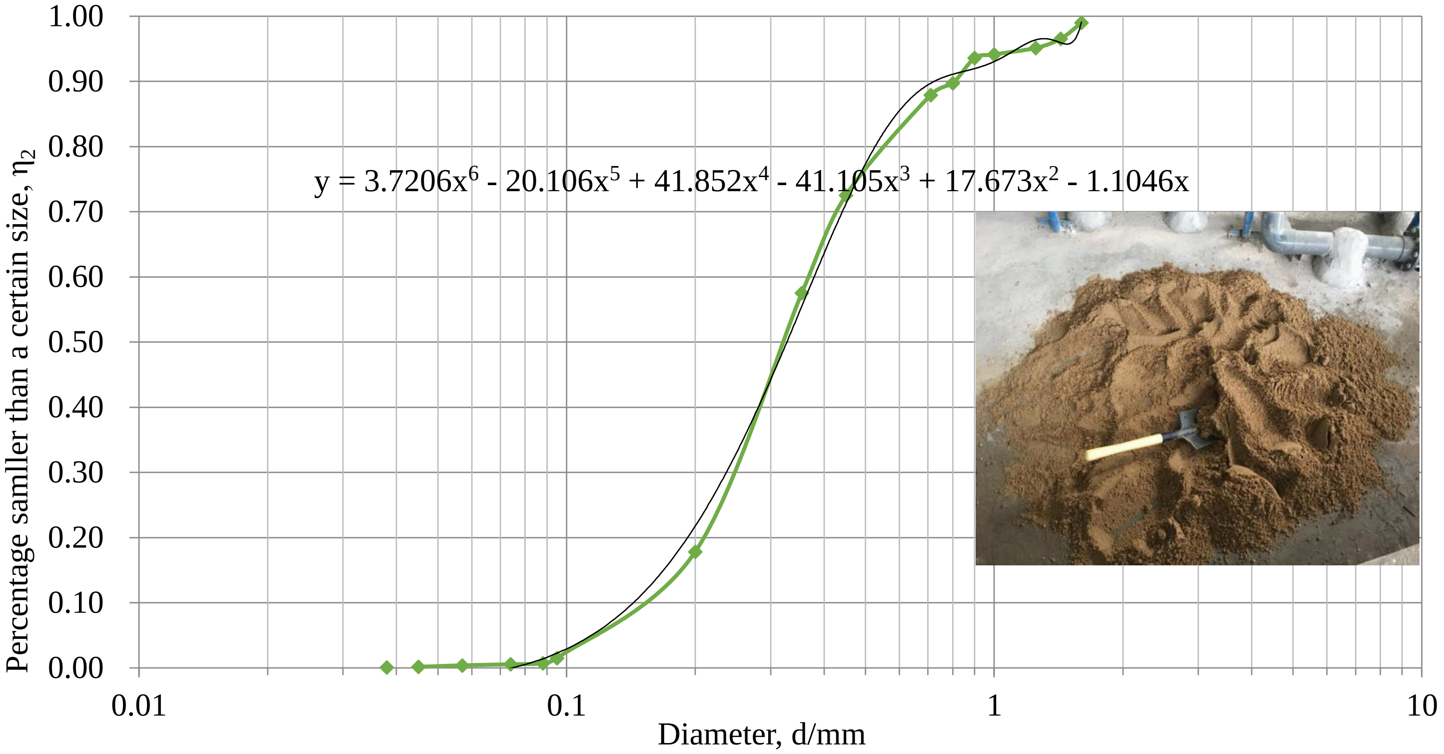

Figure 33. The gradation curve for the bed sand (The axis is logarithmically converted). The green curve stands for the gradation curve. The black curve is the fitted curve and the fitted function is shown aside.

The beginning of the bed area was constrained by concrete wedges (The gray parts in Figure 32) which had the same height as the bed thickness and same width as the channel width. The length of the wedges was 10 cm in order to provide a smooth slope connecting the bottom of the channel and the bed surface. The wedges were set to prevent erosion from taking place at the beginning and the end of the bed area. The locations of upstream wedges in all cases were set at least 100 cm away from the confluence area. Pretests in [61] had proved that 100 cm was enough for the upstream flow above the sand bed flow to be fully developed and following a log curve for the streamwise velocity distribution along z-axis. The downstream wedges were formed using rocks but not concrete (Figure 35).

The additional sediment fed into the flume were natural sands coated by waterproofing blue color, which made the sedimentation pattern easier to see through the flume walls or the water surface. The colored sediment were produced and processed through “resin solidification dying method” by the supplier. This method uses the mixture of ethoxyline resin and dye powder as the color layer and solidifies onto the sediment surface at 200-300°C. The color coating processed through this method would not fade inside the flow and the color layer was thin enough to make sure the unit weight does not change much after coloring (ρ_S= 2597~2650kg/m^3). The gradation of the additional sediment was determined after a series of pre-tests, which include feeding several groups of sediment with different combinations of diameters varying from 0.1 mm to 1.5 mm separately into the flume and then noting the sedimentation patterns respectively. The results showed that the additional sediment smaller than 0.074mm would not deposit in the test area and the additional sediment bigger than 0.095mm mostly deposit at the upstream bed area. Following that, the additional sediment with the marked diameter of 0.074-0.095mm (the marked diameter is marked by the supplier) were selected. The sieve analysis result of the selected additional sediment is shown in Table 3 and Figure 34.

Table 3. The sieve analysis results for the additional sediment. The value of D_{25}, D_{50}, D_{75}, D_{90} and sorting coefficient is calculated from the fitted curve in Figure 34.

Sieve Pore Size D/mm	Sieve Weight M_1/g	Sieve and Passing Weight M_2/g	Net Passing Weight, ΔM/g	Percentage of Total, η_1	Percentage of Grains Smaller Than the Sieve Pore Size, η_2
0.355	257.55	257.56	0.01	0.000014	1.0000
0.2	244.95	266.46	21.51	0.030167	0.9698
0.095	251.91	729.30	477.39	0.669514	0.3003
0.088	257.06	374.62	117.56	0.164872	0.1354
0.074	255.78	300.28	44.50	0.062409	0.0730
0.057	246.65	250.54	3.89	0.005456	0.0676
0.045	241.39	277.02	35.63	0.049969	0.0176
0.038	247.43	255.81	8.38	0.011752	0.0058
0	237.50	241.67	4.17	0.005848	0

Sample Weight (After test) W/g	713.04	D_{25}/mm	0.098
		D_{50}/mm	0.135
Sample Weight (Original) W0/g	712.8	D_{75}/mm	0.169
		D_{90}/mm	0.190
Error, E	0.0003	Sorting Coefficient (So)	1.72

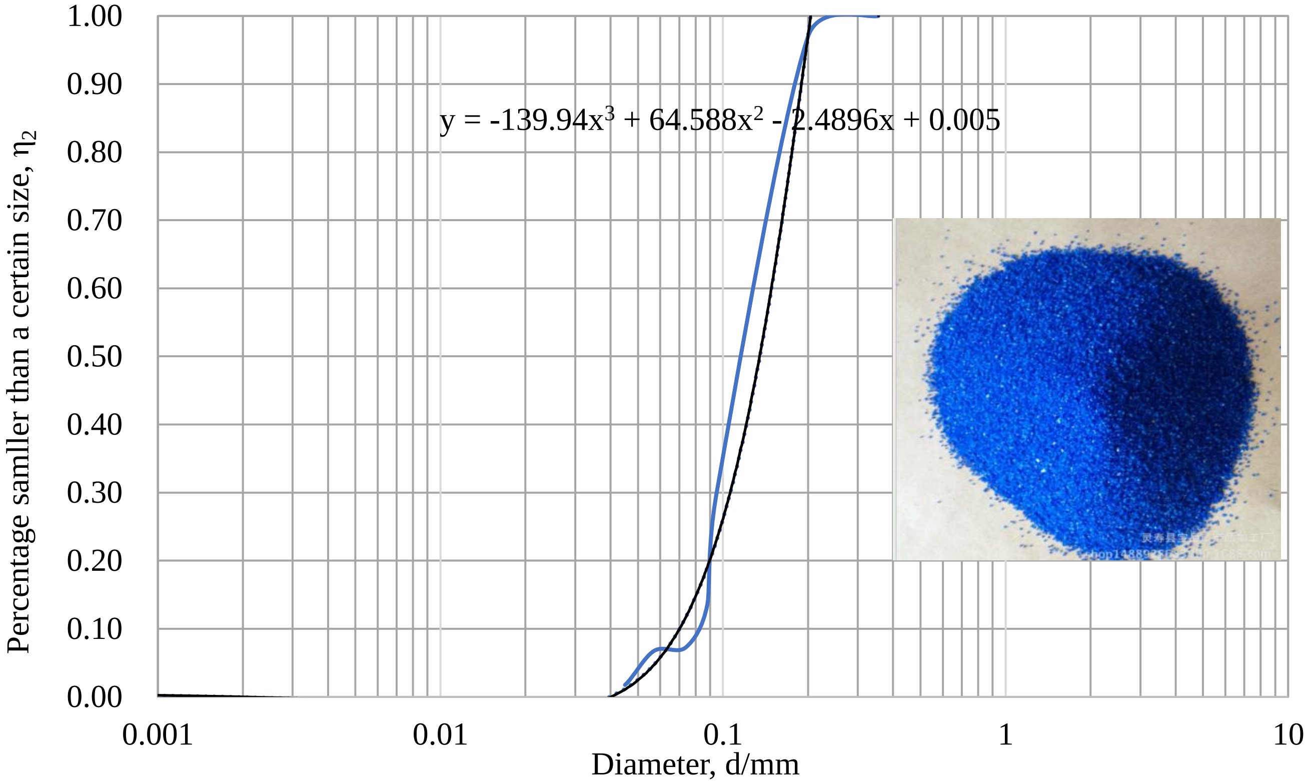

Figure 34. The gradation curve for the additional sediment (logarithmically converted). The blue curve stands for the gradation curve. The black curve is the fitted curve and the fitted function is shown aside.

4.2 Experiment Procedures

4.2.1 Preparation

First, inject clear water into the downstream tank until the water surface inside the tank reaches a certain level, which could make sure the outlet of the downstream tank is always below the water level when pumps are working. Then, set the concrete wedges in position. After that, add bed sands into the bed area and compact into near-flat state.

The purpose of pre-wetting was to set the original bed roughness closer to real River's bed roughness. The purpose of compaction was to make sure the bed roughness doesn't change much after consolidation. Then, drop the downstream sluice gate and raise the water level gradually until the bed surface is totally submerged. After 3 hours of wetting, drop the water level to the original value and raise the downstream sluice gate. Finally, adjust the bed thickness and compact the bed to the flat state (Figure 35a).

4.2.2 Equilibrium Bed State Generation

First, close the valve and turn on the pump. Gradually open the valve until the water comes out of the upstream tanks at a low flow rate to prevent scouring on the bed area. Then, adjust the flow rate and water level gradually at the same time until both of them reach the required value and fix the valve. The bed area should remain flat during the procedure. Finally, let it run for 24 hours. 24 hours' run is proved to be long enough to generate an equilibrium state (Figure 35b) through pre-tests.

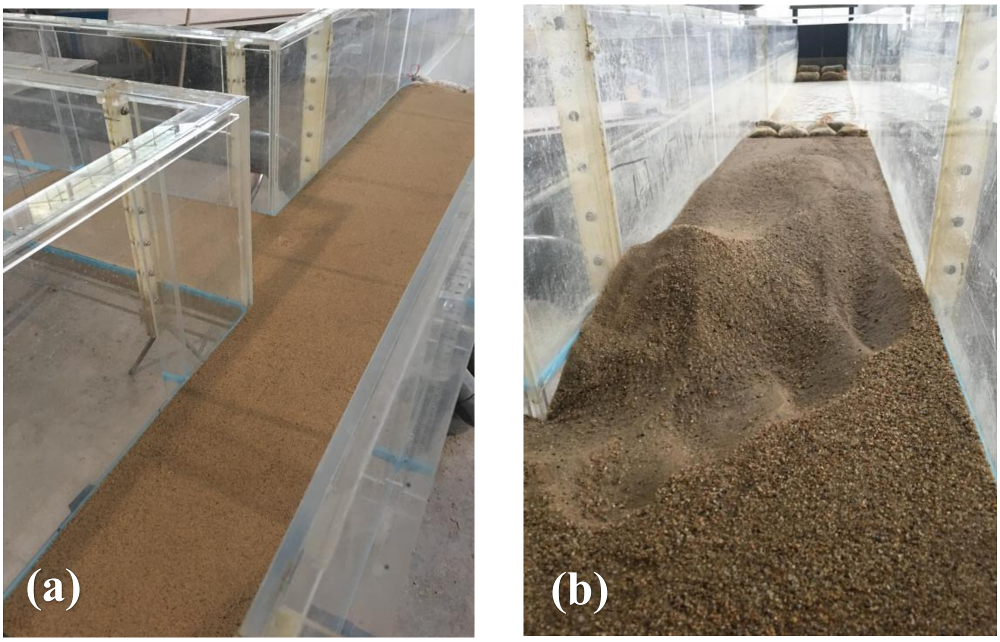

Figure 35. (a) The initial bed state and (b) the equilibrium bed state after scouring.

4.2.3 Consolidation

Gradually close the valve to let the water level drop down below the bottom of the flume and stay in the tanks. Then, let the bed area dry itself through 24 hours' undisturbed standing. After that, sprinkle cement power onto the bed area and pre-consolidate for another 24 hours. Finally, coat the bed area evenly with a grout layer and consolidate for another 24 hours. The grout layer is about 3mm thick. (Figure 36).

A mean absolute difference in the bed roughness estimate between fixed and loose beds of 0.166 mm was found when tested on a sand bed in [28]. The consolidation material used in [28] is plaster of Paris coated by spar urethane, which shares the similar surface property with grout. Moreover, the aggregate material used in grout is bed sand. In conclusion, it could be considered that the roughness didn't change much before and after the consolidation.

Figure 36. The consolidation process using (a) cement powder and (b) grout.

4.2.4 Measurements

The bed elevation was measured through a hand-held laser rangefinder (Figure 37a). The rangefinder was fixed on a frame above the flume which ensures the rangefinder always perpendicular to the flat bed surface. The frame could move both along the channel and across the channel on roller tracks with distance scale mark on it. Set the flume bottom surface as the datum of morphology measurement. The elevation of the rangefinder is first measured (50 cm). The, the x-y coordinate of one measured point was determined by the according scale mark on the roller track. The z coordinate of it was determined by the difference between 50 cm and the rangefinder reading value.

The rangefinder sampling gap was set as 5 mm across the stream and 2 cm along the stream. The elevation of intermediate points was calculated through spline interpolation in Matlab (See Appendix 2.2 Sedimentation Image Converting Code) based on the measured samples. The bed morphology map is generated by Tecplot 360 EX2018 R1.

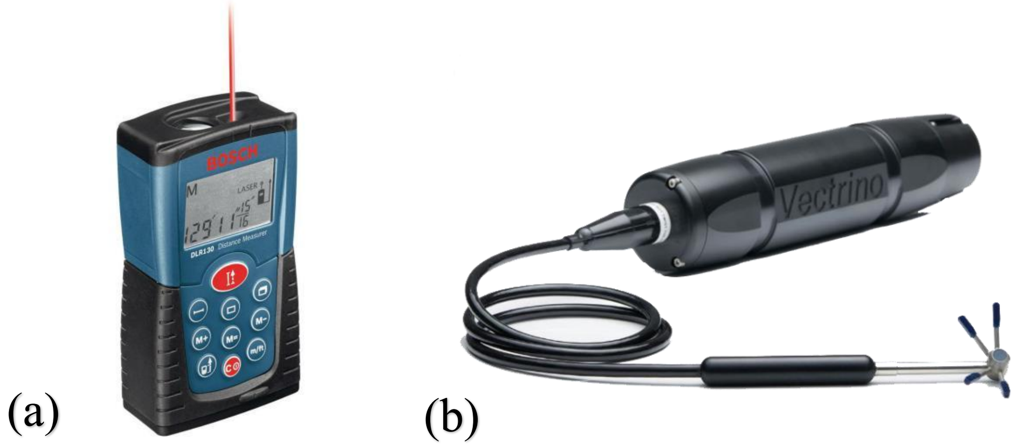

Figure 37. The measuring devices. (a) The laser rangefinder. (b) The Acoustic Doppler Velocimetry (ADV) [24] [26].

The flow field was measured through Acoustic Doppler Velocimetry (ADV) device (Figure 37b). ADV is based on the Doppler acoustic principle. The sampling points were measured non-invasively at a 5 cm distance ahead of the probe tip. Measurements reasonably near the sides and bottom of the channel could be done with considerably good accuracy. However, ADV could only make single-point measurements facing downwards, thus it was unable to measure the near surface flow field. In addition, it could not measure series of points at one time without disturbance. Finally, it is difficult to obtain accurate measurements at locations with shear within the sample volume due to high velocity gradients or large vortices [53]. Since the flow field in this study was at steady state and the near-surface flow is not a focus of this study, ADV was chosen as the measurement tool.

The locations of measured cross sections were chosen based on the bed morphology development after scouring. It started near the first scour hole and ended at the flow recovery zone in order to capture the entire confluence area. The detailed location of measured profiles is shown in Figure 38.

The lateral boundary of measured cross sections was 5 cm away from the flume walls in order to prevent any signal disturbance from the walls. The bottom of each measured cross section was 0.5 cm above the bed surface; points closer to the bed could not be measured due to signal interference from the bed. The gap between two measured cross sections was 10 cm. The gap between two measured vertical profiles in one cross section was 2 cm, which made 15 vertical profiles in total for each cross section. The gap between two measured points in one vertical line was 0.5cm at the near-bed area and 1cm at the other area in order to have more accurate measurements for the flow field near the bed (Figure 39).

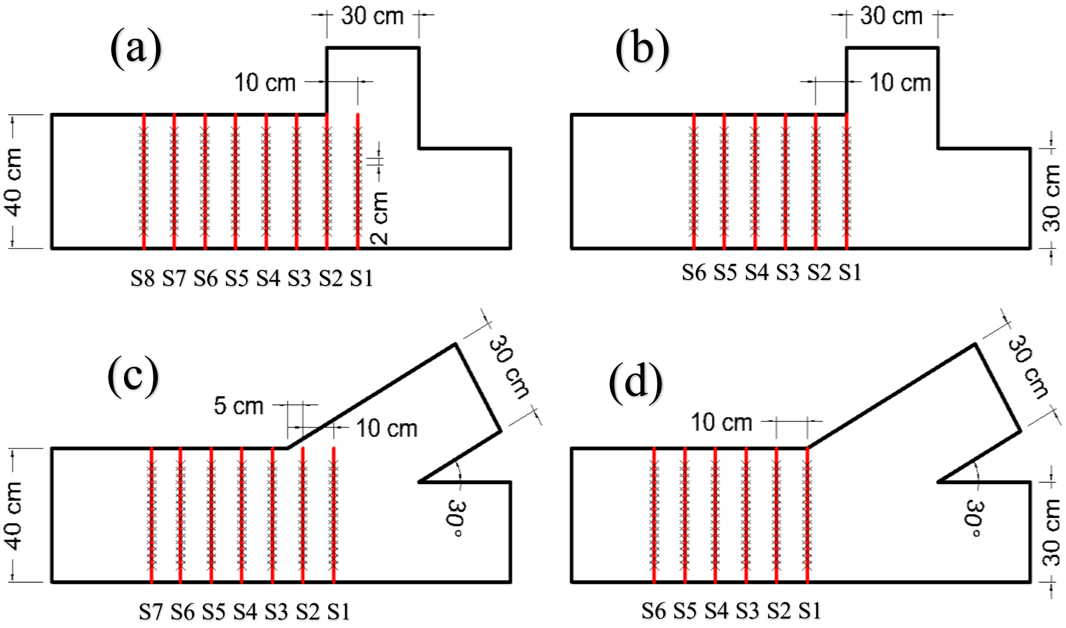

Figure 38. The location of measured cross sections for all 4 cases. The red lines indicate the measured cross sections. (a) case 90_3_2; (b) case 90_2_3; (c) case 30_3_2; (d) case 30_2_3. S1-S8 stands for the slice number in each case.

The sampling frequency was set to be 200 Hz. Previous study [59] had shown that the cumulative variance will be systematically convergent on a constant value when the recording length was longer than 60 s, which indicated the record length was sufficient to capture major sources of variation of velocity. Following that, the record length was set to be 100 s.

During the measurement stage, the correlation factors for 4 probes could be guaranteed to be at a high level (>80%) by adjusting the nominal velocity range, transmit length and sampling volume in Vectrino software interface and feeding talcum powder into the flume. Talcum has very good scattering and signal reflecting characteristics. Although the specific gravity of talcum (2.6-2.8) is bigger than clear water, which may bring additional negative flow velocity along the z-axis to the flow field. The talcum powder was sufficiently fine grained that settling velocity was negligible. Feeding talcum can raise signal intensity, improving measurement accuracy, and does not induce any disturbance to the flow field.

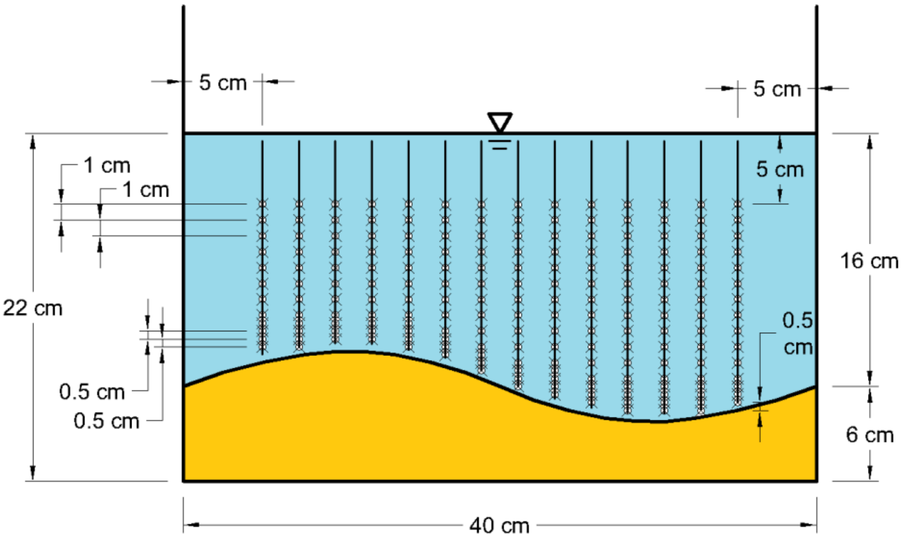

Figure 39. Schematic of ADV measurement lines for each cross section (Note: The sketch is not to scale).

4.2.5 Sediment Feeding

Turn on the pump, adjust the valve and tailgate until the discharge rate and flow depth reach the required value. Pre-wet the additional sediment in order to prevent the grains combining air and forming into bubbles and floating at the flow surface. Feed the sediment into the tributary channel through a glass funnel with the help of a constant tiny flow flushing (Figure 40). The sediment feeding rate was fixed at 67 g/min for all cases. The diameter of the funnel stem was 1cm, which made its disturbance to the flow field negligible. Pre-tests had shown that sediment tended to deposit before going into the confluence zone when the outlet of the funnel was set at the middle of the flow or near the bed. So the outlet of the funnel was submerged 2 cm under the flow surface.

There were three sets of sediment feeding experiments. The sediment used in all three sets were taken from the same one sample. The feeding location was set to be 100 cm away from the tributary mouth in all three sets.

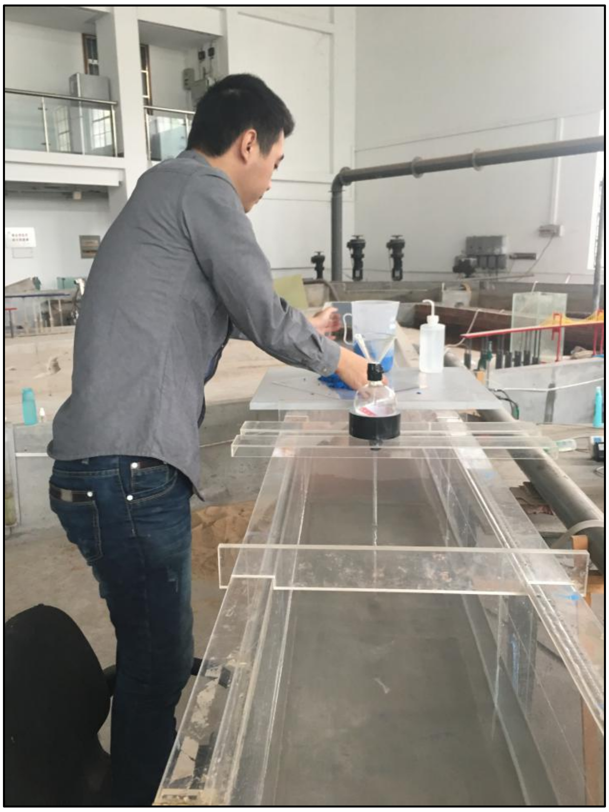

Figure 40. The sediment feeding process.

The first set was to study the sedimentation patterns under different feeding locations including the left bank, the mid channel and the right bank of the tributary. The left and right bank feeding location was 5 cm away from the bank and the mid channel feeding was 15 cm away from both banks. The pictures were taken one minute after the feeding was done. The feeding amount was 800 g for all three locations.

The second set was to study how the sedimentation pattern changed versus time when feeding from the mid channel of the tributary. The feeding location was 15 cm away from both banks. The pictures were taken one minute after the feeding was done and 1 h, 2 h and 3 h after the feeding was done. The feeding amount was 4000 g.

The third set was to study the sedimentation patterns under different feeding amount. The experiments were done in the first and second set, which were feeding 800 g and 4000 g sediment from the mid channel of the tributary and taking pictures one minute after the feeding was done.

After all the sedimentation pictures in the above-mentioned sets were collected, the sedimentation areas in the pictures were identified by its blue color, picked out and output as pictures with transparent background through Matlab (see more details in Appendix 2.2: Sedimentation Image Converting Code) and Adobe Photoshop CS6. Note that these pictures used red instead of blue as the indicator of the sedimentation area for higher color contrast with the flume background (gray). The final sedimentation pattern results pictures were generated combing these pictures with the bed morphology results generated in Tecplot 360 EX 2018 R1. The combination procedure is achieved through the Geo-referencing function in Arcmap 10.2.

4.2.6 Data Conversion and Analysis

The flow field data was converted through Matlab. The code could be seen in "Appendix 2: Matlab Code_2.1 The Flow Field Data Processing Code". The code copyright totally belongs to Dr. Colin Rennie [27] [43].

First, the data were replaced by "Not-a-Number" (NaN) from the raw ones by locating the samples where flow velocity was shown as "3276.7" or "0". This value is set by Vectrino as an indicator for the samples which were considered as bad for any directions.

Then, the suspicious data spikes were removed using three different despiking filters. First, the two redundant simultaneous vertical velocity measurements were used to identify and remove bad points, with a difference threshold set to 0.1 m/s. Second, the local instantaneous acceleration was calculated by dividing every two adjacent velocity measurements by the time gap between them throughout the time series. If the result was greater than 1.5 g = 14.7 m/s^2, the measured velocity value would be removed. Despiking was also done for those measurements which lay more than four standard deviations away from the local mean [41]. Values removed during the despiking procedures were substituted with a new value by means of linear interpolation from neighbouring values in the time series.

Following that, the data would be filtered if the noise ratio was higher than 0.75. The noise ratio in x-axis direction is determined by:

$$NR_x = \left| \frac{N_x}{\overline{\left| U' \right|}} \right| \tag{4}$$

NR_x is the noise ratio in x-axis direction. N_x is the noise level in x-axis direction (Table 4). U' is the fluctuating component for the velocity in x-axis direction. It is determined by:

$$U_i' = U_i - \overline{U_i} \tag{5}$$

The noise level in x-axis was determined by plotting the energy spectrum curve and integrating the difference between the measured spectrum curve and the theoretical -5/3 slope line within the inertial sub-range for the x-axis component (see [43] for details). Figure 41 shows the ideal energy spectrum curve under noise-free condition. Figure 42 shows the energy spectrum curves of two samples in case 90_3_2. The black circles mark the differences. It can be seen that the inertial sub-range is larger for the noisy sample than that for the low-noise sample, suggesting it had larger eddies. This was observed for almost all filtered samples. These eddies may have induced shear in the sample volume, leading to the noise at the high frequency end of the spectrum.

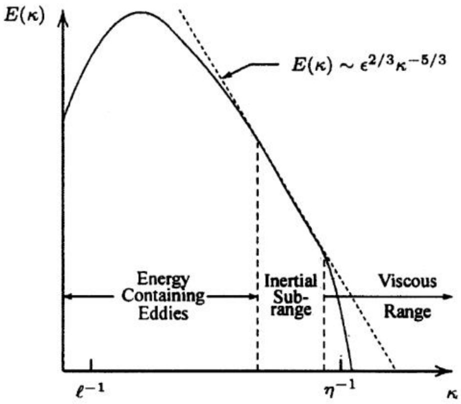

Figure 41. Energy spectrum for a turbulent flow (log-log scales) [55].

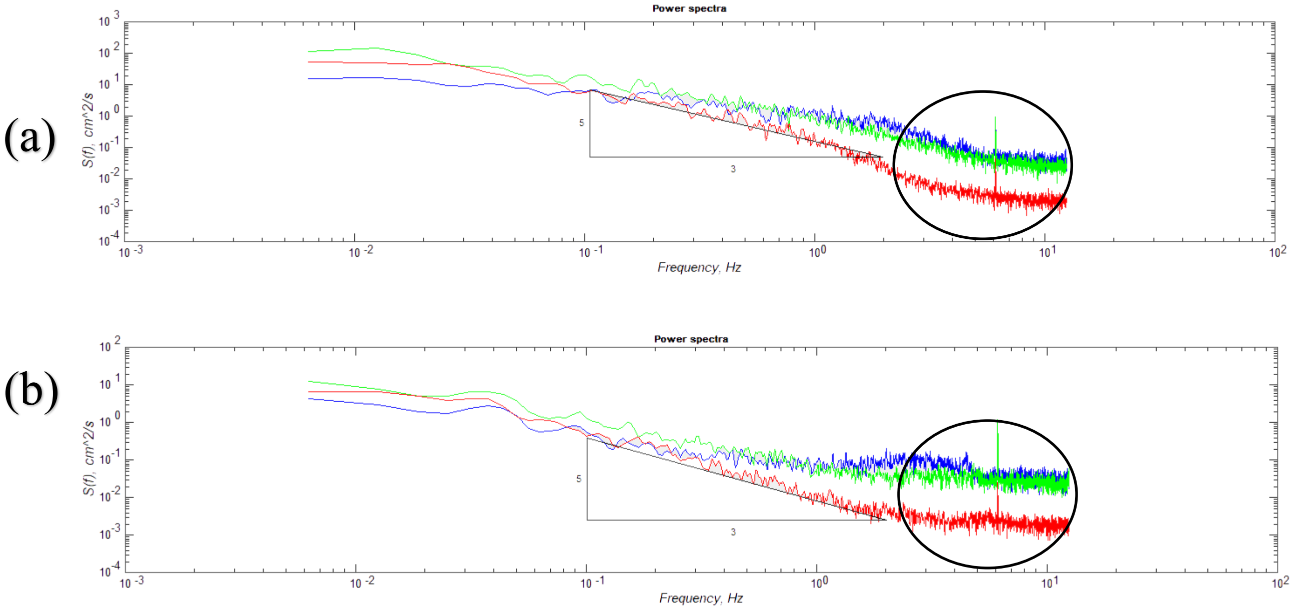

Figure 42. The energy spectrum for (a) a low-noise sample (N_x=0.013m/s) and (b) a noisy sample(N_x=0.072m/s).

Once a measurement sample is detected as having a large noise ratio (>0.75), the high frequency part of the time series that does not fit the -5/3 line will be cut off using a low pass filter and another variable called “Filter_Flag” is set to be “1” for this sample to mark it. Otherwise, it is set to be “0”. The locations of samples with Filter_Flag equal to 1 is plotted in Figure 43. and total number is summarized in Table 4.

Note that the noise ratio mentioned here is different from the Signal to Noise Ratio (SNR). The reason why using NR_x as the filter condition but not SNR is because SNR could be low if the measured point witnesses a high level of turbulence but a relatively low level of noise. Using SNR as the filter condition may wrongly filter out some turbulent components and lead to data distortion for Reynolds shear stress. The correlation factor is also not applied here to be the filter condition. The reason is mentioned in Chapter 4.2.4.

It can be seen in Figure 43(a) that the noise level in x-axis direction is lower near the shear layer and the separation zone for all 4 cases. Other areas share a similar level of noise ratio. Most filtered samples are located at the places which witness a low level of TKE. That's because the filter condition is the quotient of noise and fluctuating component, the places of lower level of TKE make it easier to trigger the filter condition when most places share the similar level of noise.

Table 43(b) shows that the percentage of filtered samples is somewhat larger in 30° confluence experiments than in the 90° confluence. It is also bigger under discharge ratio 2:3 than that under discharge ratio 3:2. This is because the overall turbulence level (TKE) is lower in 30° confluences and discharge ratio 2:3 condition, which makes it easier to trigger the filter condition.

Table 4. The total number of filtered samples for 4 cases.

Case No.	90_3_2	90_2_3	30_3_2	30_2_3	Total
Total Samples Volume	1415	1074	1324	932	4745
Filtered Samples Volume	59	137	88	128	412
Filter Percentage	4.17%	12.77%	6.65%	13.73%	8.68%

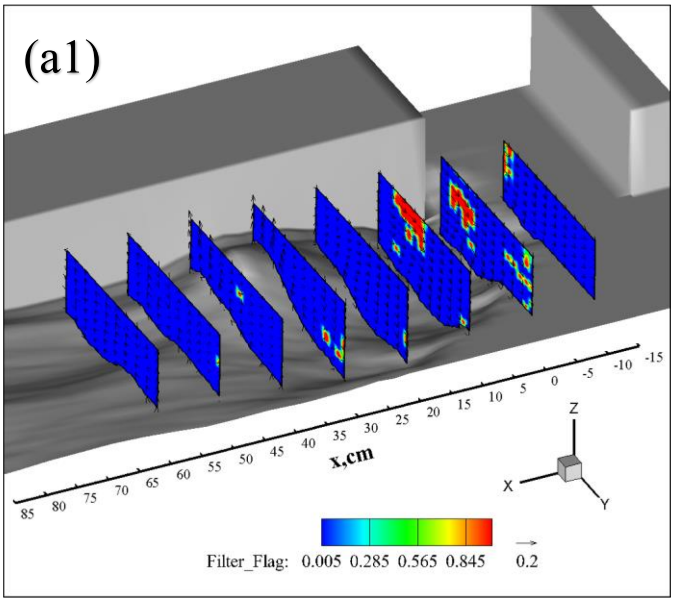
(a1)
85 80 75 70 65 60 55 50 45 40 35 30 25 20 15 10 5 0 -5 -10 -15
x,cm
Z
X
Y
Filter_Flag: 0.005 0.285 0.565 0.845
0.2

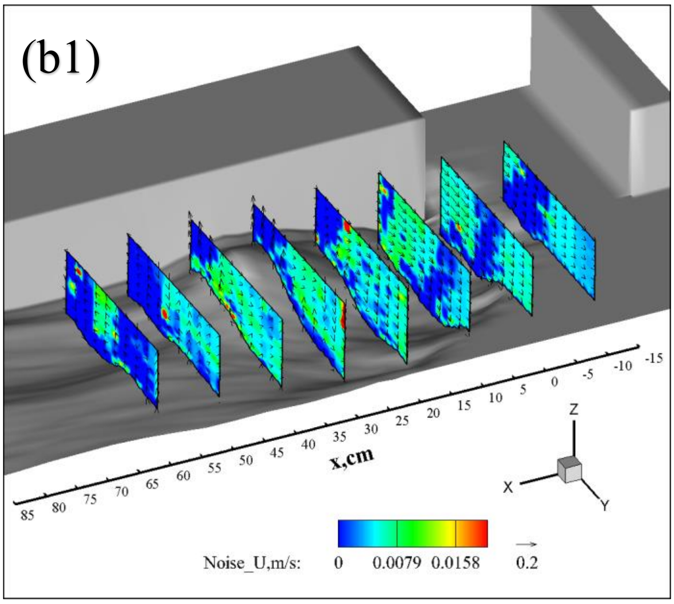
(b1)
85 80 75 70 65 60 55 50 45 40 35 30 25 20 15 10 5 0 -5 -10 -15
x,cm
Z
X
Y
Noise_U,m/s: 0 0.0079 0.0158
0.2

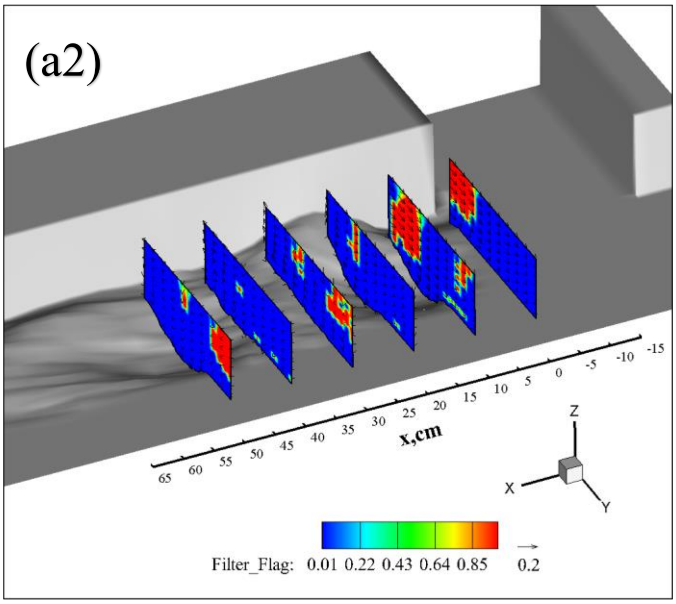
(a2)
65 60 55 50 45 40 35 30 25 20 15 10 5 0 -5 -10 -15
x,cm
Z
X
Y
Filter_Flag: 0.01 0.22 0.43 0.64 0.85
0.2

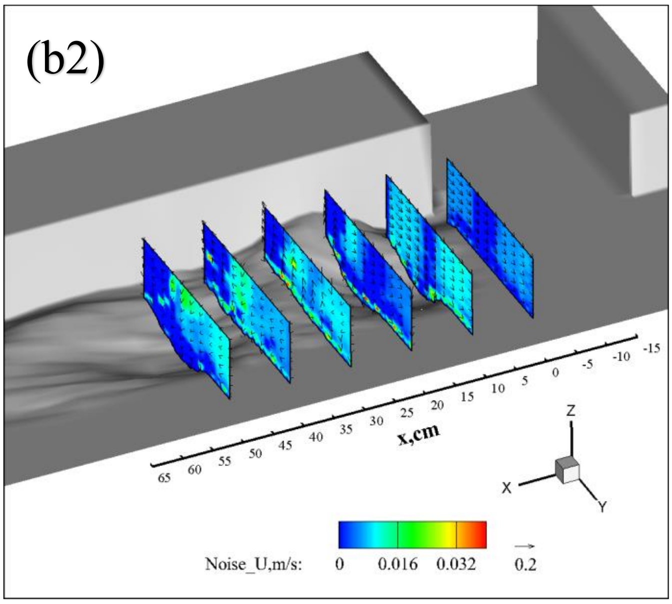
(b2)
65 60 55 50 45 40 35 30 25 20 15 10 5 0 -5 -10 -15
x,cm
Z
X
Y
Noise_U,m/s: 0 0.016 0.032
0.2

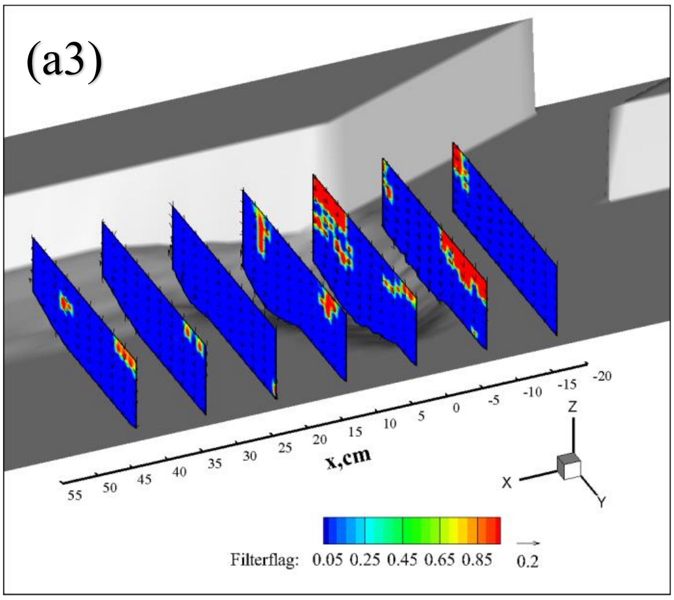
(a3)
55 50 45 40 35 30 25 20 15 10 5 0 -5 -10 -15 -20
x,cm
Z
X
Y
Filterflag: 0.05 0.25 0.45 0.65 0.85
0.2

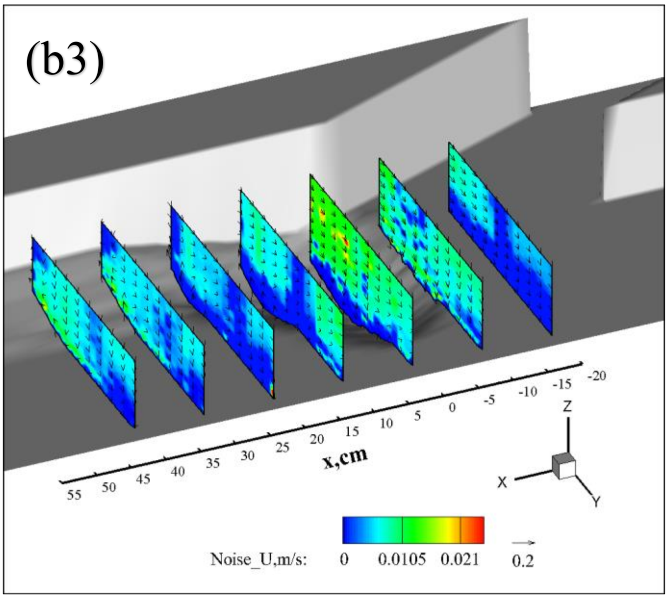
(b3)
55 50 45 40 35 30 25 20 15 10 5 0 -5 -10 -15 -20
x,cm
Z
X
Y
Noise_U,m/s: 0 0.0105 0.021
0.2

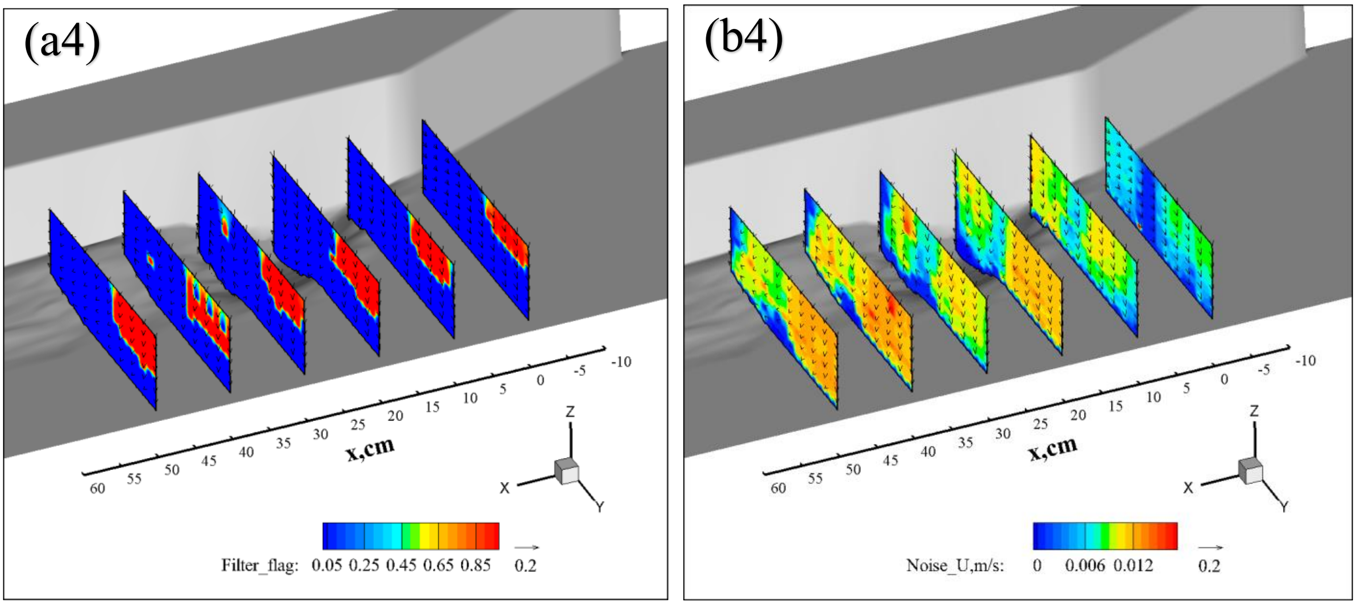

Figure 43. The location of all (a) filtered samples and (b) the noise level in x-axis direction. Number 1,2,3,4 stand for the case 90_3_2, 90_2_3, 30_3_2 and 30_2_3, separately. Note that the vectors stand for the secondary flow direction and intensity. Note use of different scales in each plot.

Finally, other variables including the fluctuating component (U’), Reynolds shear stress (RSS), and the turbulent kinetic energy (TKE) are calculated. The formulae are given as:

$$RSS = -\rho\overline{U^{'}V^{'}}, -\rho\overline{V^{'}W^{'}}, -\rho\overline{U^{'}W^{'}} \tag{6}$$

$$TKE = \frac{1}{2}(\overline{U^{'2}} + \overline{V^{'2}} + \overline{W^{'2}}) \tag{7}$$

Where U’, V’ and W’ are the turbulent components for the velocity in x-axis, y axis and z-axis, separately. ρ is the water density.

Chapter 5 Results

5.1 Bed Morphology

The bed morphology is measured by a hand-held laser rangefinder after the consolidation procedure. Samples are interpolated and plotted into color map through Tecplot 360EX_2018R1. The results are shown in Figure 44.

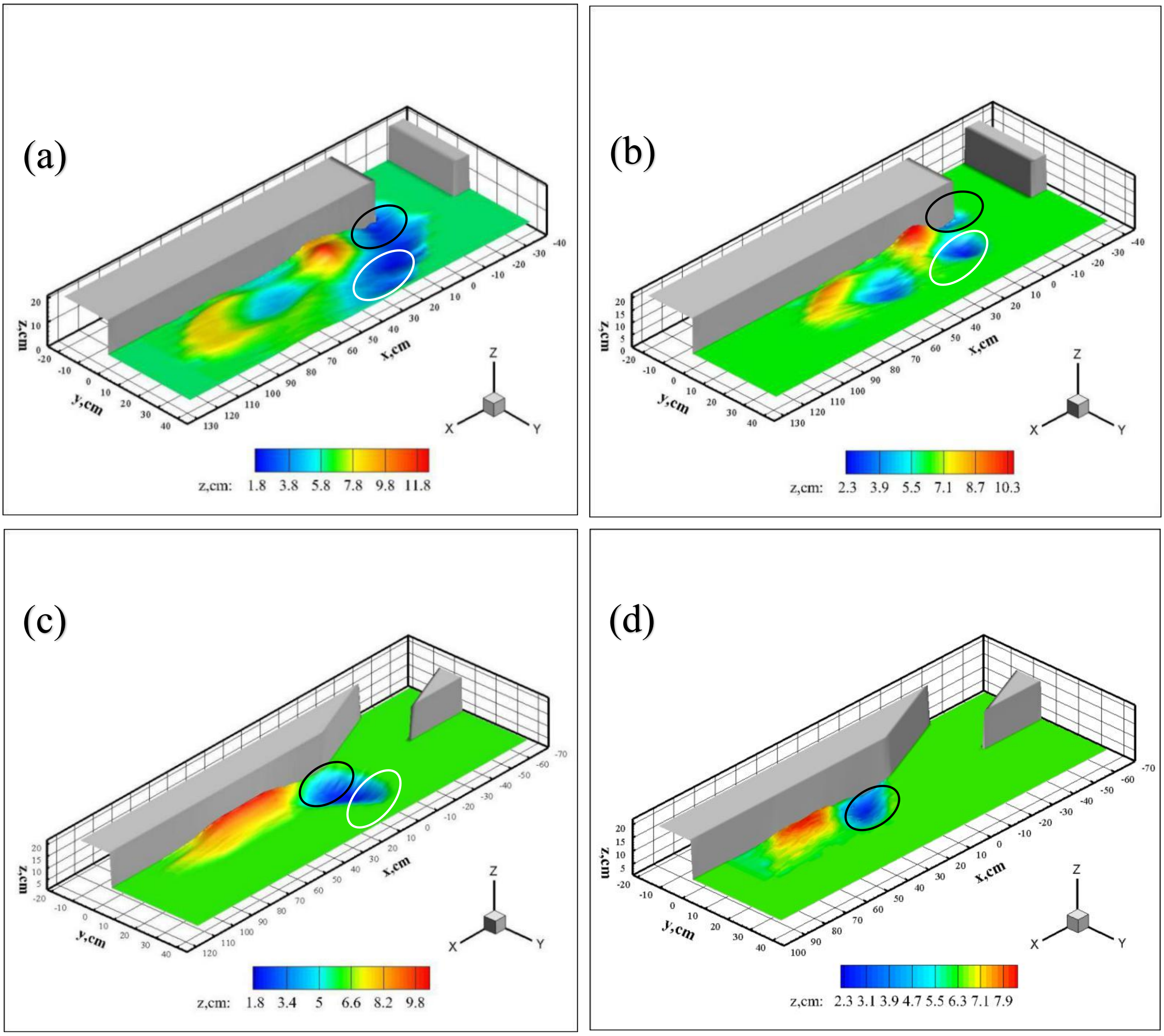

Figure 44. The color maps of equilibrium bed morphology state of 4 cases. The black circle marks the corner hole. The white circle marks the mid channel hole. (a) case 90_3_2; (b) case

90_2_3; (c) case 30_3_2; (d) case 30_2_3.

The x, y and z axes respectively extend towards the downstream direction, to the outer bank, and upwards. The places where elevation is equal to the original flat bed elevation, 6 cm above the flume floor, are colored green in the bathymetry maps. Note that the top of the flume edge in color maps is set to have the same height as the flow surface, which is 22 cm, in order to have a better view. The actual flume edge height is 40 cm, which is 18 cm above the flow surface. The contour maps throughout this chapter follow the same rules mentioned above.

The bed morphology in case 90_3_2 has the widest development range among all four cases (Table 5). Note that the scour hole in 90_3_2 does not quite reach the outer bank: the scour extends to about 1 cm from the outer bank and the boundary elevation between the biggest scour hole and the outer bank is 6cm. This proves that the flume channel is wide enough for a full development for all cases.

The bed morphology in case 90_3_2 is characterized by a curved scour hole developed from the downstream corner to the outer bank. The details of the curved scour hole can be seen clearly in the color map (Figure 44a). The picture shows that the curved scour hole is actually formed by two scour holes connecting together near the mid channel. One is near the downstream junction corner of the flume channel. It will be mentioned as the "corner hole" in the rest of the article. The other one seems to be located beneath the shear layer in mid channel and consists of four smaller adjacent scour holes. They will be mentioned as the "mid channel hole-A, B, C, D" in the rest of the article. "A, B, C, D" stands for the four smaller scour holes numbered from upstream to downstream, respectively. The upstream boundary of the mid channel hole-A is not consistent with that of the corner hole and is approximately pointed to the upstream junction corner, which also proves that the mid channel hole-A, B, C, D are generated due to a different reason (shear layer) compared with the corner hole (flow turning). Another reason why the curved scour hole can be treated as two is explained in case 90_2_3. In addition, a conical sand bar surrounded by the curved scour hole forms near the inner bank but is not connected with the bank. Another fan-shaped sand bar forms near the flow recovery zone at downstream, connecting the conical sand bar with two long sand ridges on its lateral side. The third scour hole is observed between the two sand ridges, but much shallower than the curved scour hole. It will be mentioned as the “downstream hole” in the rest of the article.

Table 5. The geometric parameter of the bed morphology development for 4 cases.

Case No.		90_3_2	90_2_3	30_3_2	30_2_3
Width of Bed Morphology Development Area, cm		48.0	29.0	31.0	10.0
Length of Bed Morphology Development Area, cm		122.5	82.5	95.0	75.0
Corner Hole	Maximum Depth, cm	4.0	2.5	3.0	3.7
	Area, cm^2	247.5	75.0	200.0	225.0
	Shape	Round	Round	Strip	Strip
	Location	Around the downstream junction corner		Behind the downstream junction corner	
Mid channel Hole	Maximum depth, cm	4.4	3.7	4.4	N/A
	Area,cm^2	862.5	240.5	122.7	
	Shape	Curved	Round	Round	
	Location	Mid channel			
Downstream Hole	Maximum Depth, cm	1.5	3.0	N/A	
	Area,cm^2	491.0	594.0		
	Shape	Round	Round		
	Location	Between two sand ridges	Near one sand ridge		
Upstream	Maximum Height, cm	6.0	4.5	4.1	1.9

Bar	Area, cm^2	491.0	198.0	750.0	385.0
	Shape	Cone	Half Cone	Trapezoid	
	Location	near but not attached to the inner bank	attached to the inner bank		
Downstream Bar	Maximum Height, cm	2.2	2.6	N/A	
	Area, cm^2	520.0	360.0		
	Shape	Cone	Half Cone		
	Location	Near the flow recovery zone			

The bed morphology in case 90_2_3 is characterized by the separated two scour holes: the corner hole and mid channel hole, which also proves that the curved scour hole in case 90_3_2 is actually two holes connecting together. The variation of discharge changes the relative position of the two scour holes. It also can be seen that the mid channel hole is much smaller in case 90_2_3 than that in case 90_3_2. In contrast, the corner hole does not very much in size between the two cases. Interestingly, the downstream hole is both deeper (3 cm) and bigger (approximately 594 cm^{2}) in case 90_2_3 than that in case 90_3_2 (1.5 cm and approximately 491 cm^{2}). The conical sand bar in case 90_2_3 is attached to the inner bank and both shorter (4.5 cm) and smaller (approximately 198 cm^{2}) than that in case 90_3_2 (6 cm and approximately 491 cm^{2}). Only the inner part of the fan-shaped sand bar and sand ridges are visible in case 90_2_3. Both the width (29 cm) and length (82.5 cm) of bed morphology development in case 90_2_3 is smaller than that in case 90_3_2 (48 cm and 122.5 cm).

The bed morphology in case 30_3_2 is characterized by a triangular scour hole and a trapezoidal sand bar attached to the inner bank. Although there is no clear boundary inside the hole that could separate it into two as in the 90° cases, the triangular scour hole can also be treated as two scour holes connecting together. One is a strip-shape scour hole after the downstream corner, which is similar to the corner hole in case 90_3_2 and 90_2_3. The other one is located near the mid channel beneath the shear layer, which is similar to the mid channel hole in case 90_3_2 and 90_2_3. In addition, no fan-shaped bar, sand ridges nor downstream scour hole are observed in case 30_3_2 compared with case 90_3_2.

The bed morphology in case 30_2_3 is characterized by a tilted scour hole after the downstream corner and a ribbon-shape sand bar attached to the inner bank. If the triangular scour hole can be treated as a combination of titled scour hole and a mid channel hole in case 30_3_2. The titled scour holes in case 30_2_3 and 30_3_2 share similar location with the corner holes in case 90_2_3 and 90_3_2. Thus, they will also be described as "corner holes" in the rest of the article. Both the height and area of the trapezoidal sand bar are smaller in case 30_2_3 (1.9 cm and appropriately 385 cm^2) than that in case 30_3_2 (4.1 cm and appropriately 750 cm^2). Interestingly, both the depth and area of the corner hole are bigger in case 30_2_3 (3.7 cm and appropriately 225 cm^2) than that in case 30_3_2 (3 cm and appropriately 200 cm^2), which is opposite comparing case 90_2_3 with 90_3_2. The fan-shaped bar, sand ridges and downstream scour hole are also not observed in case 30_2_3 compared with case 90_2_3.

In addition, it could be seen that the range of bed morphology development always starts upstream of the downstream junction corner for discharge ratio 3:2 cases and always starts exactly at the downstream junction corner for discharge ratio 2:3 cases. Moreover, the length and width ratio of bed morphology development area is quite similar for case 90_3_2 (ratio = 2.55) and 90_2_3 (ratio = 2.84). However, this ratio is not comparable for case 30_3_2 (ratio = 3.06) and case 30_2_3 (ratio = 7.50). This is probably owing to the flow trajectory and relative strength of the tributary as a function of confluence angle and discharge ratio.

5.2 Flow Velocity

The flow field is measured by an ADV after the consolidation and bed morphology measurement procedure. Samples are despiked and filtered through Matlab code. Then they are interpolated and plotted into contour map through Tecplot 360EX_2018R1.

The contour map of flow velocity results is shown in Figure 45, Figure 46. and Figure 47.

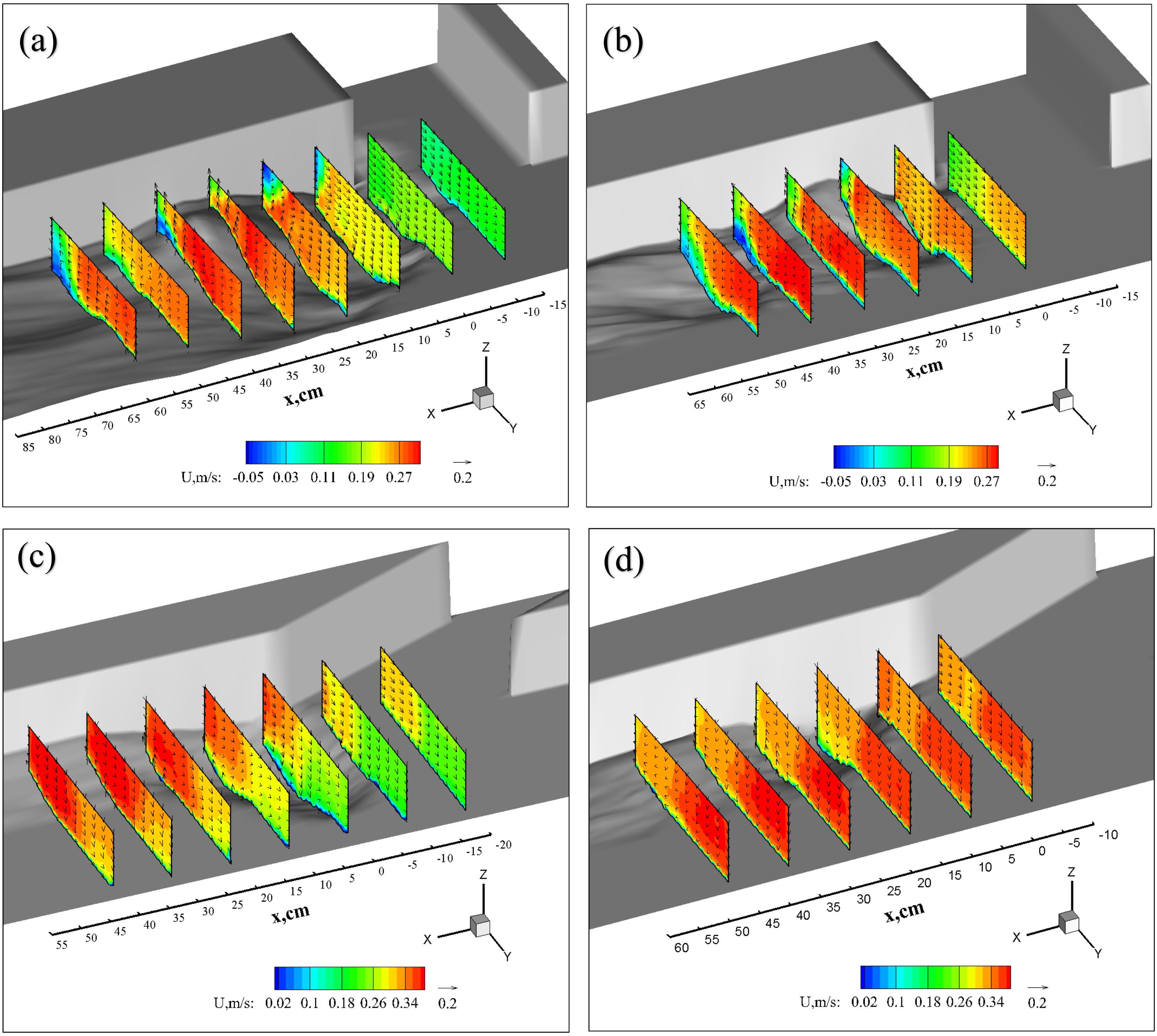

Figure 45. The streamwise flow velocity “U” contour map for 4 cases. (a) case 90_3_2; (b) case 90_2_3; (c) case 30_3_2; (d) case 30_2_3. Note that the vectors stand for the secondary flow direction and intensity. Note use of different scales in each plot.

The top of each slice shares the same elevation of 17 cm (11 cm above the initial bed elevation), which is 5 cm below the flow surface or the top of flume edge shown in the contour maps for all cases. This is because the ADV probe should be totally submerged into the flow and the transmitting length is about 5 cm. The bottom of each slice is 0.5 cm above the bed surface, the closest the ADV could measure to the bed. Both lateral sides of each slices are 5 cm away from the bank, which was set to avoid any signal disturbance coming from the boundary. The arrows plotted on each slice stand for the cross-sectional flow vectors (secondary flow measured as cross-stream and vertical velocity components). The arrow head points to the flow direction while the arrow length stands for the magnitude. A reference arrow length for 0.2 m/s is placed at the bottom of each map. The velocimetry contour maps in subsequent sections follow the same rules mentioned above.

Figure 45 shows that for the 90° cases, both tributary and main channel flow in the x-axis direction starts to accelerate at about x = 10cm (slice S3 in case 90_3_2 and S2 in case 90_2_3). It reaches the peak level at about x = 30cm (S5 in case 90_3_2 and S4 in case 90_2_3), then it maintains a high level in both cases. The flow acceleration is due to the compression of the flow towards the flow path induced by the separation zone and the upstream bar. The tributary flow and the main flow also collide with and shear each other and combine in a smaller initial total cross section (40cm × 16cm< 30cm × 16cm) while advecting downstream.

In contrast, the acceleration effect is reduced for 30°cases (velocity increase from 0.33 m/s to 0.36 m/s) compared to 90° cases (from 0.11 m/s to 0.3 m/s). The tributary flow starts to accelerate at about x = 0 cm (after S2 in case 30_3_2 and S1 in case 30_2_3) and then maintains that high level after x = 5 cm (after S3 in case 30_3_2 and S2 in case 30_2_3). And the main channel flow rate doesn't change much throughout the confluence zone both for case 30_3_2 and case 30_2_3. This relatively weak acceleration is probably due to the decrease of the size of flow separation zone and the upstream bar.

In addition, the low flow rate and reverse flow near the inner bank indicates the flow separation zone. Despite the concordant beds of the tributary and main channel, it can be seen that the flow separation zone is smaller near the bed and bigger near the flow surface for both cases. The flow separation zone is wider and longer in case

90_3_2 than that in case 90_2_3 from x = 10 cm (S3 in case 90_3_2 and S2 in case 90_2_3) to x = 30 cm (S5 in case 90_3_2 and S4 in case 90_2_3). This is because the bigger tributary flow rate makes it harder to turn and longer to reattach to the inner bank in case 90_3_2. This area of the separation zone will be denoted as “upstream separation area”. However, the separation zone is approximately of same size from x = 40 cm (S6 in case 90_3_2 and S5 in case 90_2_3) to x = 60 cm (S8 in case 90_3_2 and after S6 in case 90_2_3). This area of the separation zone will be denoted as “downstream separation area”. The presence of the downstream separation area is probably the reason why the flow velocity remains high in the flow recovery zone after the flow acceleration zone.

Interestingly, both cases witness a reverse flow zone in the downstream separation area. The reverse flow is probably due to the disturbance of the cone-shaped bar ahead of it, which could cause a wake flow behind it as flow bypasses.

In contrast, there is no low flow rate area shown near the inner bank in the 30° cases, which indicates that the flow separation zone is quite small (if the maximum width of the separation zone is less than 5 cm, this area couldn’t be measured or shown on contour maps). Smaller size of the flow separation zone brings a smaller level of compression effect towards the tributary flow, which explains why the acceleration effect is minimal in the 30° cases. In addition, there is no reverse flow detected after the sand bar, likely because a trapezoid-shaped bar with a low elevation would not cause any obvious wake flow behind it.

Figure 46 and Figure 47 show the secondary flow patterns by plotting the streamwise and vertical flow contour maps (a clearer view of secondary pattern could be seen in Figure 48). It can be seen that the secondary flow exists in all four cases but varies in intensity and range from one case to another.

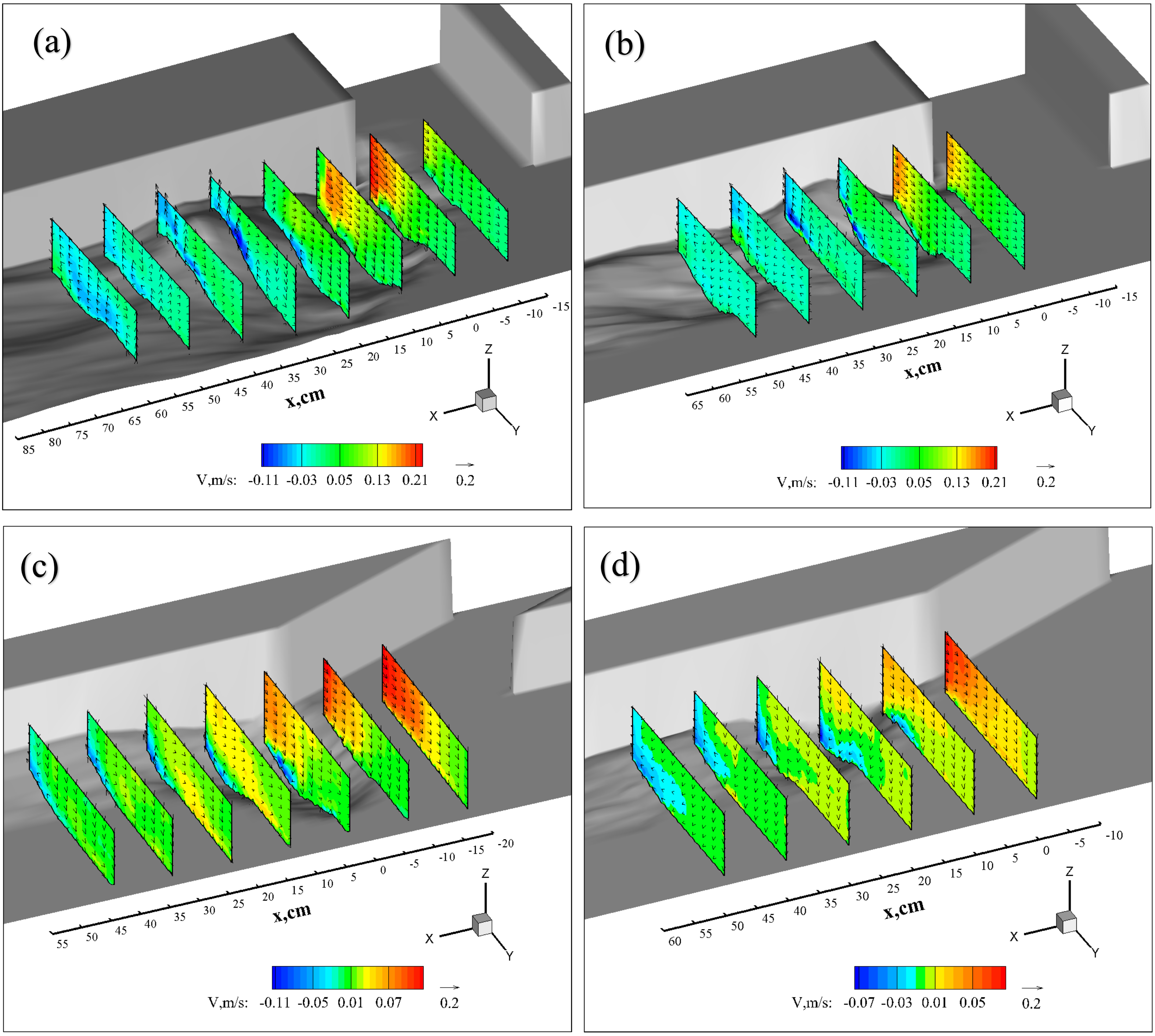

Figure 46. The cross-stream flow velocity "V" contour map for 4 cases. (a) case 90_3_2; (b) case 90_2_3; (c) case 30_3_2; (d) case 30_2_3. Note that the vectors stand for the secondary flow direction and intensity. Note use of different scales in each plot.

Figure 46 shows the cross-stream flow velocity contour map. If the flow towards the positive y-axis is defined as "outward flow" and the negative direction as "inward flow", for all cases the mouth of the tributary channel is the place witnessing a high level of outward flow, while the upstream face of the upstream bar has a high level of inward flow. The range of outward flow is always larger than that of inward flow for all cases, because the initial tributary flow state is outwards flow across the whole section. On the other hand, the inward flow is generated only when the downward flow hits the bottom and is forced to change direction. Interestingly, inward flow exists at the face of the upstream bar for all cases, but at the bottom of scour holes only for 30° cases. This inward flow in the scour hole can occur because the initial cross-stream flow velocity “V” emanating from the tributary channel is much lower in 30° cases compared with 90° cases, thus it is easier to be deflected by the mean flow and change the flow direction. So the inward flow location is closer to the tributary mouth in 30° cases than that in 90° cases.

Figure 47 shows the vertical flow velocity contour map. If the flow towards the positive direction of z-axis is defined as “upwelling flow” and the negative direction as “downwelling flow”, for all cases downwelling flow is located above the upstream scour hole, while upwelling flow occurs above the upstream face of the upstream bar.

Finally, Figure 48 provides the secondary flow streamlines superimposed on the streamwise velocity. The secondary flow generating from the tributary tends to move towards the outer bank due to the limitation of the upstream bar in case 90_3_2. This will be described as “outer secondary flow”. At the same time, the upwelling flow near the top of the upstream bar tends to go inward when it gets near the flow surface, and then follows the inner bank due to the deepening of flow path after the upstream bar. This results in the extension of the separation zone (the downstream separation area), which has another secondary flow inside of it, which will be denoted as “inner secondary flow”. The outer secondary flow rotates counter-clockwise along the flow path while the inner one rotates clockwise. The upstream bar also causes inclination of the shear layer between these two secondary flow cells. Flow goes upward and inward within the shear layer. This pattern is not so clear in case 90_2_3 due to the relatively weak secondary flow generating from the tributary channel. This is pattern is absent in case 30_3_2 and 30_2_3 due to the relatively small dimension of the upstream bar.

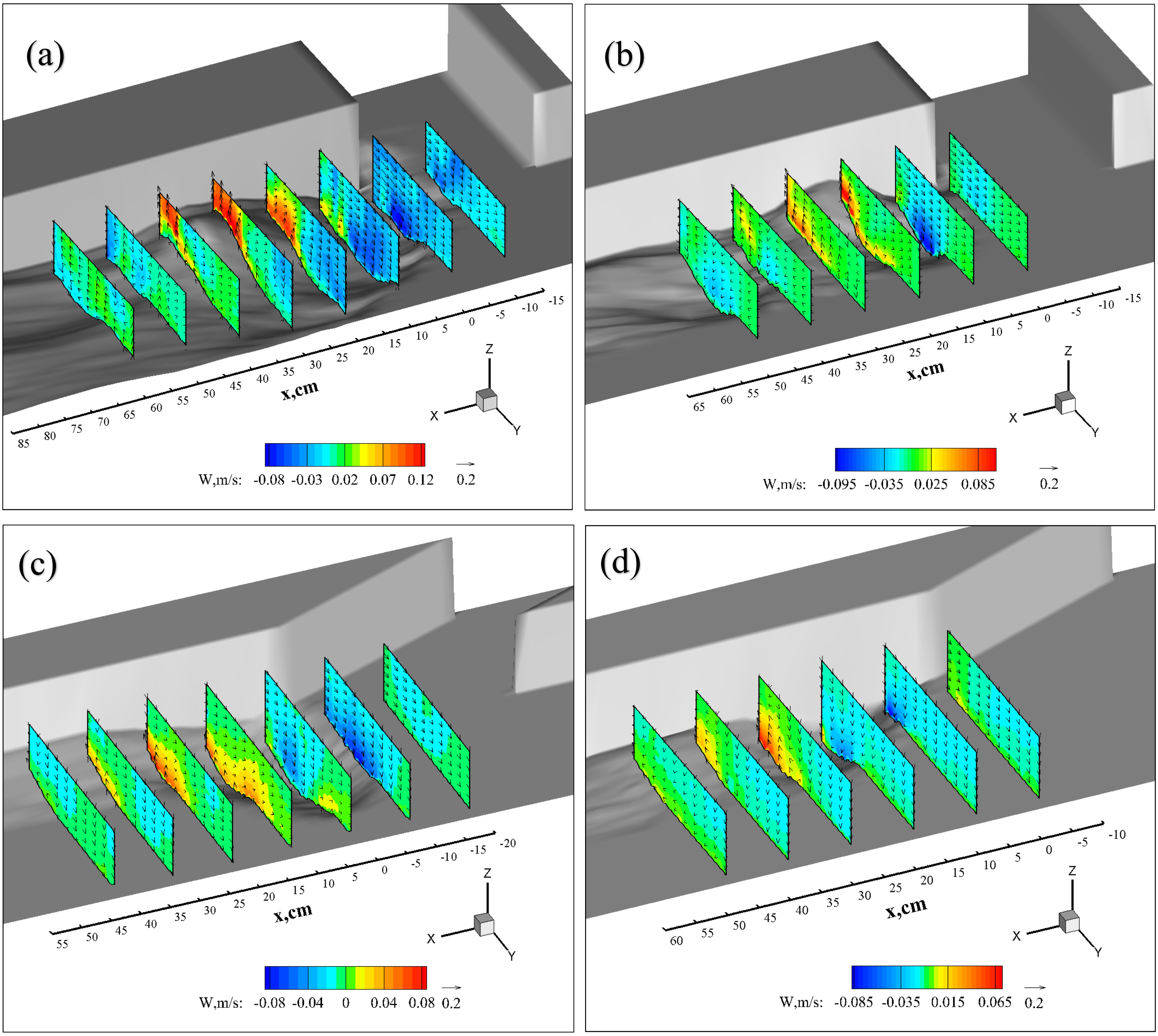

Figure 47. The vertical flow velocity "W" contour map for 4 cases. (a) case 90_3_2; (b) case 90_2_3; (c) case 30_3_2; (d) case 30_2_3. Note that the vectors stand for the secondary flow direction and intensity. Note use of different scales in each plot.

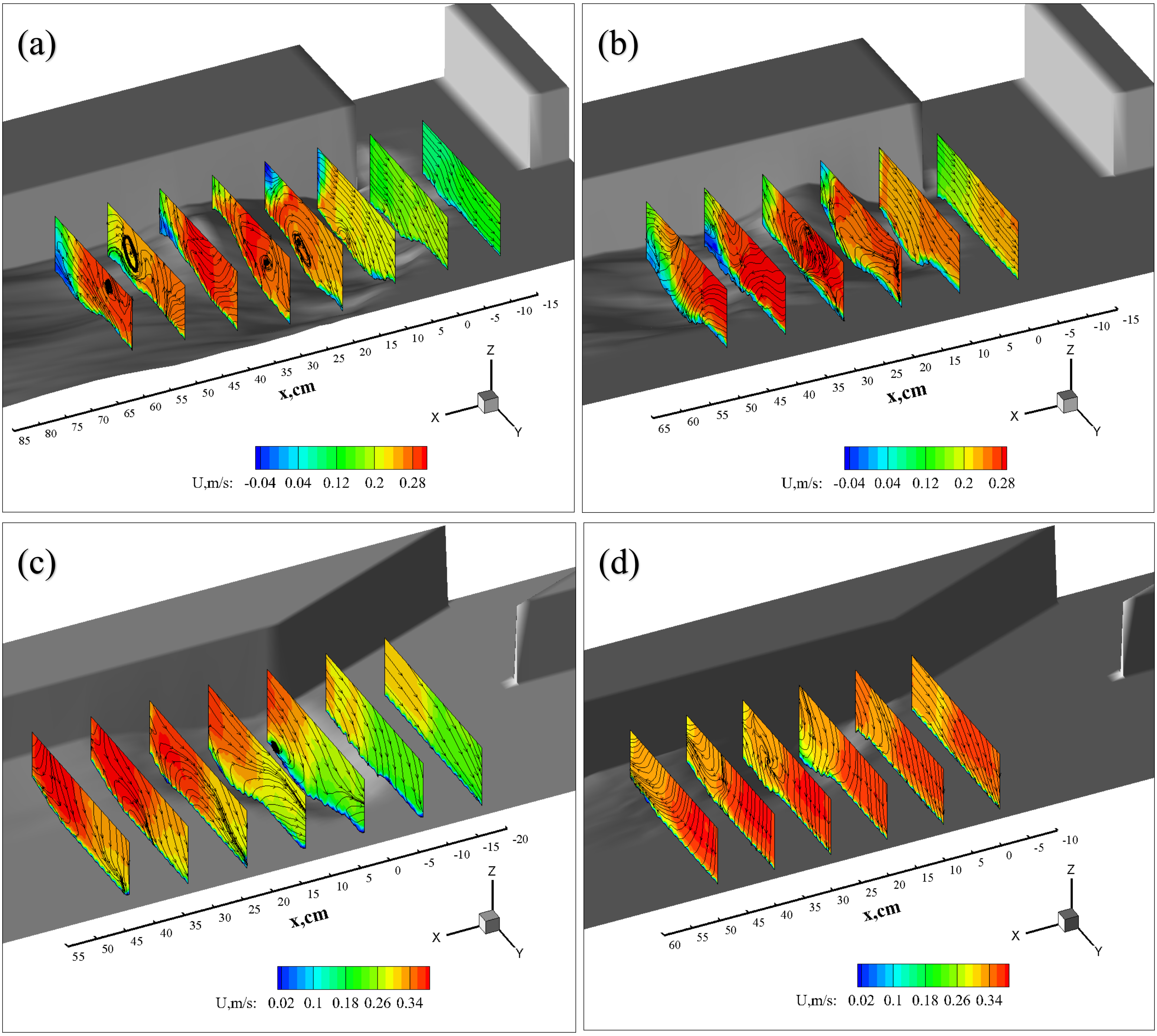

Figure 48. The secondary flow streamlines superposed on the stream-wise flow velocity plots for 4 cases. (a) case 90_3_2; (b) case 90_2_3; (c) case 30_3_2; (d) case 30_2_3. Note use of different velocity scales.

The double-secondary-flow phenomenon could also be explained by the wake flow theory, which usually witnesses inward flow at the tail of its wake region and upstream flow at the middle of its wake region. This theory could be proved when comparing the inward flow in case 90_2_3 with that in case 90_3_2 in this area. It can be seen that the inward flow rate is lower in this area in case 90_2_3 due to the half-cone-shaped upstream bar ahead of the wake region and lower flow rate in the tributary flow, compared to the cone-shaped upstream bar and higher flow rate in the tributary flow in case 90_3_2. Another evidence to support the wake flow theory is that the bed morphology behind the upstream bar, which includes a scour hole and a fan-shaped downstream bar, follows the general pattern of a wake flow bed morphology.

In general, the secondary flow intensity and range of discharge ratio 3:2 cases are always higher than that of discharge ratio 2:3 cases. They also higher in 90°cases than that in 30°cases. Given that the secondary flow is mainly generated by the tributary flow path, higher discharge ratio could bring a higher flow rate and wider path of tributary flow, leading to greater secondary circulation in the confluence zone. Furthermore, a higher junction angle provides a sharper curved path for the secondary flow to develop longer. There also shows some unique secondary flow patterns for the area behind the upstream bar in the 90° cases due to the wake flow.

5.3 Turbulent Kinetic Energy

Figure 49 shows the turbulent kinetic energy (TKE) contour maps for all cases. This term is calculated through formula (7) based on the despiked and filtered flow field data.

It can be seen that the shear layer between tributary and main stream displays a high level of TKE for all cases. This is because significant downwelling flow and high gradient of flow rate in the horizontal plane take place in shear layer, which leads to a high level in the turbulent components U', V' and W'. The TKE level in shear layer gradually decreases as it extends towards downstream for all cases, because both the velocity gradient and downwelling flow decrease as it goes. The TKE level in the shear layer is higher for case 90_3_2 than for case 90_2_3 due to greater acceleration of the tributary flow in the flow acceleration zone. In contrast, the tributary stream is accelerated to a certain level which is almost even to the mean stream flow rate in case 90_2_3, which makes the streamwise flow velocity gradient near shear layer lower in case 90_2_3 compared with that in case 90_3_2.

The TKE level inside the shear layer is almost the same when comparing the case 30_3_2 and case 30_2_3. This is because the acceleration effect is minimal in the 30° cases, which reduces the flow velocity gradient near the shear layer. Moreover, the downwelling flow range and intensity are also similar for these two cases.

The separation zone is another place of high TKE for all cases. Although the separation zone is not so clear in the mean flow for cases 30_3_2 and 30_2_3, the boundary of it still can be located by the large TKE area near the inner bank. For all cases the TKE level is much higher in the separation zone than in the shear layer, because the flow condition is more complex inside the separation zone, including secondary flow in y-z plane and inverse flow in x-axis. The highest TKE level appears at the shear layer between the downstream separation area and the tributary flow both for case 90_3_2 and 90_2_3. This location not only witnesses two secondary flows beside it in y-z plane, but also highest reverse flow level in x-axis near the bottom. The TKE level in this place is higher for case 90_3_2 compared with case 90_2_3, because both the secondary flow and inverse flow intensity are weaker in case 90_2_3.

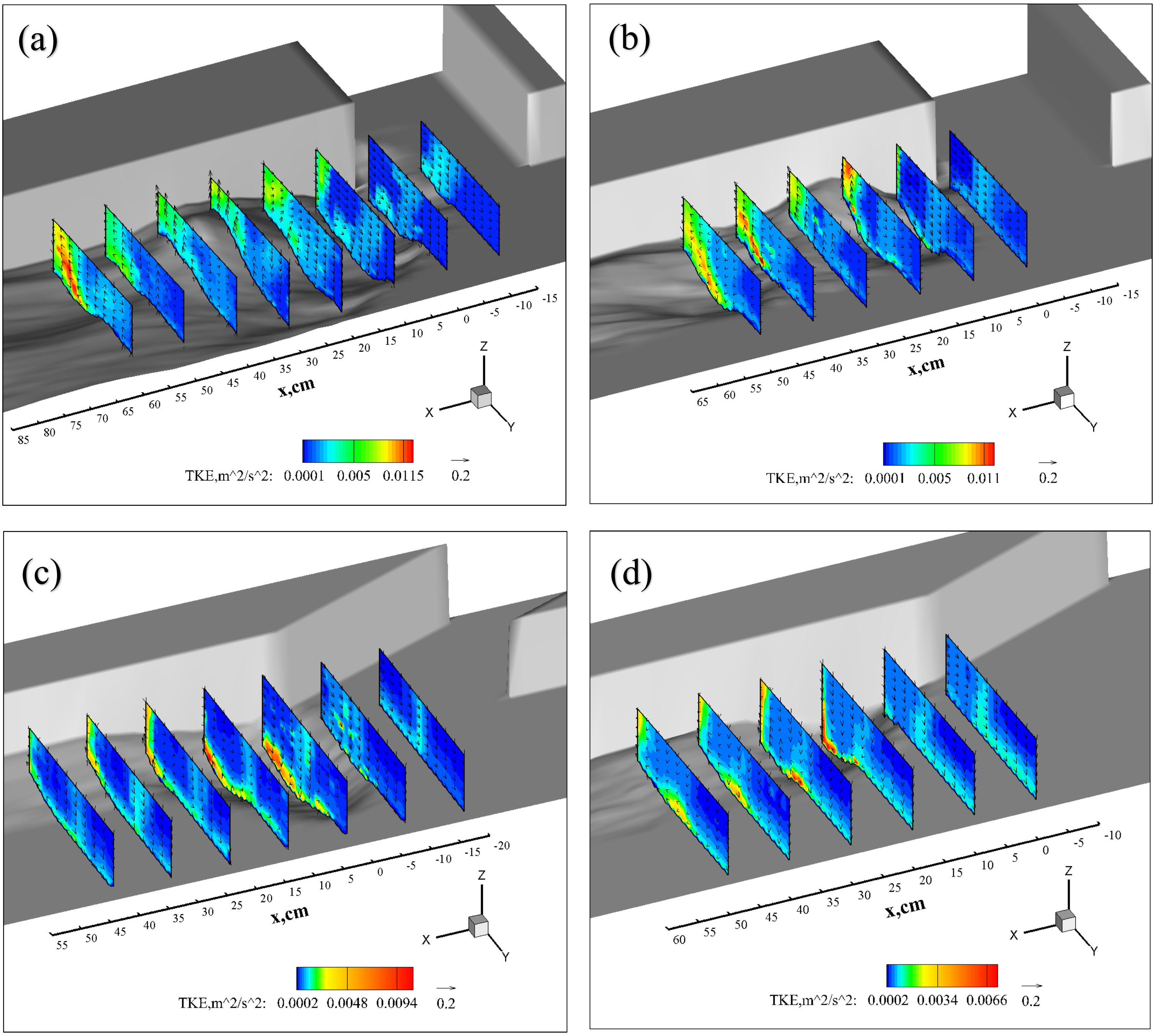

Figure 49. The turbulent kinetic energy “TKE” contour map for 4 cases. (a) case 90_3_2; (b) case 90_2_3; (c) case 30_3_2; (d) case 30_2_3. Note that the vectors stand for the secondary flow direction and intensity. Note use of different scales in each plot.

Another place of high TKE level is above the upstream face of the upstream bar in case 90_3_2 and case 90_2_3. This area is the center of the upstream secondary flow where the flow direction changes dramatically, resulting in a high turbulent level. Case

90_3_2 has a higher level of TKE and longer persistence in this area than case 90_2_3, due to greater secondary flow range and intensity. As for the case 30_3_2 and case 30_2_3, this area is located near the bottom of the scour hole due to the different location of secondary flow center in 30° cases and 90° cases. Interestingly, the TKE level in this area is much higher in 30° cases than that in 90° cases, because the velocity gradient is higher in x, y and z axis at the secondary flow center in 30° cases.

5.4 Reynolds Shear Stress

Reynolds stress is the component of the total stress tensor in a fluid derived from the Reynolds-Averaged Navier–Stokes (RANS) equations to account for turbulent fluctuations in fluid momentum. It includes Reynolds normal stress and Reynolds shear stress.

Based on the RANS equations and the stress state of a fluid element, the components and sign convention (in 3-D right-hand Cartesian space) of the Reynolds shear stresses are summarized in Table 6. Taking the Reynolds shear stress component τ_{vu} as an example, this shear stress acts on the vertical-streamwise (*zx*) plane in the *x*-axis direction. Using the Boussinesq hypothesis to relate the Reynolds stresses to velocity gradients:

$$\tau_{vu} = \vartheta_c \frac{d\overline{u_x}}{dy} \tag{9}$$

where ϑ_c is the eddy viscosity (or turbulent viscosity), which can be written as:

$$\vartheta_c = \rho {l_m}^2 \left|\frac{d\overline{u_x}}{dy}\right| \tag{10}$$

Where l_m is the mixing length.

Figure 50, Figure 51 and Figure 52 show the Reynolds shear stress components ($-\rho\overline{U'W'}, -\rho\overline{U'V'}, -\rho\overline{V'W'}$) contour maps for all cases. They will be noted shortly as “UV”, “VW” and “UW” in the following parts of the thesis.

Figure 50 shows the Reynolds shear stress UW contour map for all cases. The UW level denotes the gradient of flow velocity component U along the z-axis or the gradient of flow velocity component W along the x-axis. This principal shear stress component is generally associated with the streamwise bed shear stress and sediment transport.

Table 6. The components and sign convention of Reynolds shear stress [27].

Measurement	Stress component	Acting plane	Positive direction	Velocity gradient
$-\rho\overline{U'W'}$	τ_{uw}	yz	z	$\frac{\partial w}{\partial x}$
	τ_{wu}	yx	x	$\frac{\partial u}{\partial z}$
$-\rho\overline{U'V'}$	τ_{uv}	yz	y	$\frac{\partial v}{\partial x}$
	τ_{vu}	zx	x	$\frac{\partial u}{\partial y}$
$-\rho\overline{V'W'}$	τ_{vw}	zx	z	$\frac{\partial w}{\partial y}$
	τ_{wv}	yx	y	$\frac{\partial v}{\partial z}$

The area of highest negative UW value is located at the upstream separation zone both for case 90_3_2 and case 90_2_3, due to an inverted streamwise velocity profile at this location (Figure 45). It can also be seen that the upstream separation zone is wider but shorter in case 90_3_2 than in case 90_2_3. The area of highest positive UW value occurs above the downstream scour hole and at the shear layer between the downstream separation zone and the tributary flow path both for case 90_3_2 and case 90_2_3. This area probably results in the formation of the downstream scour hole and the time-series sediment transport pattern reported in following chapters.

As for the case 30_3_2 and case 30_2_3, likewise, the area of negative UW value occurs near the inner bank in the upstream separation zone. The area of positive UW value is located near the bed surface for all cross sections in both cases. This is typical for a uniform boundary shear flow, and demonstrates that the 30° cases are less subject to cross-stream flow dynamics than the 90° cases. The area of largest positive UW value is at the bottom of the scour hole in both cases, which explains the formation of the scour hole.

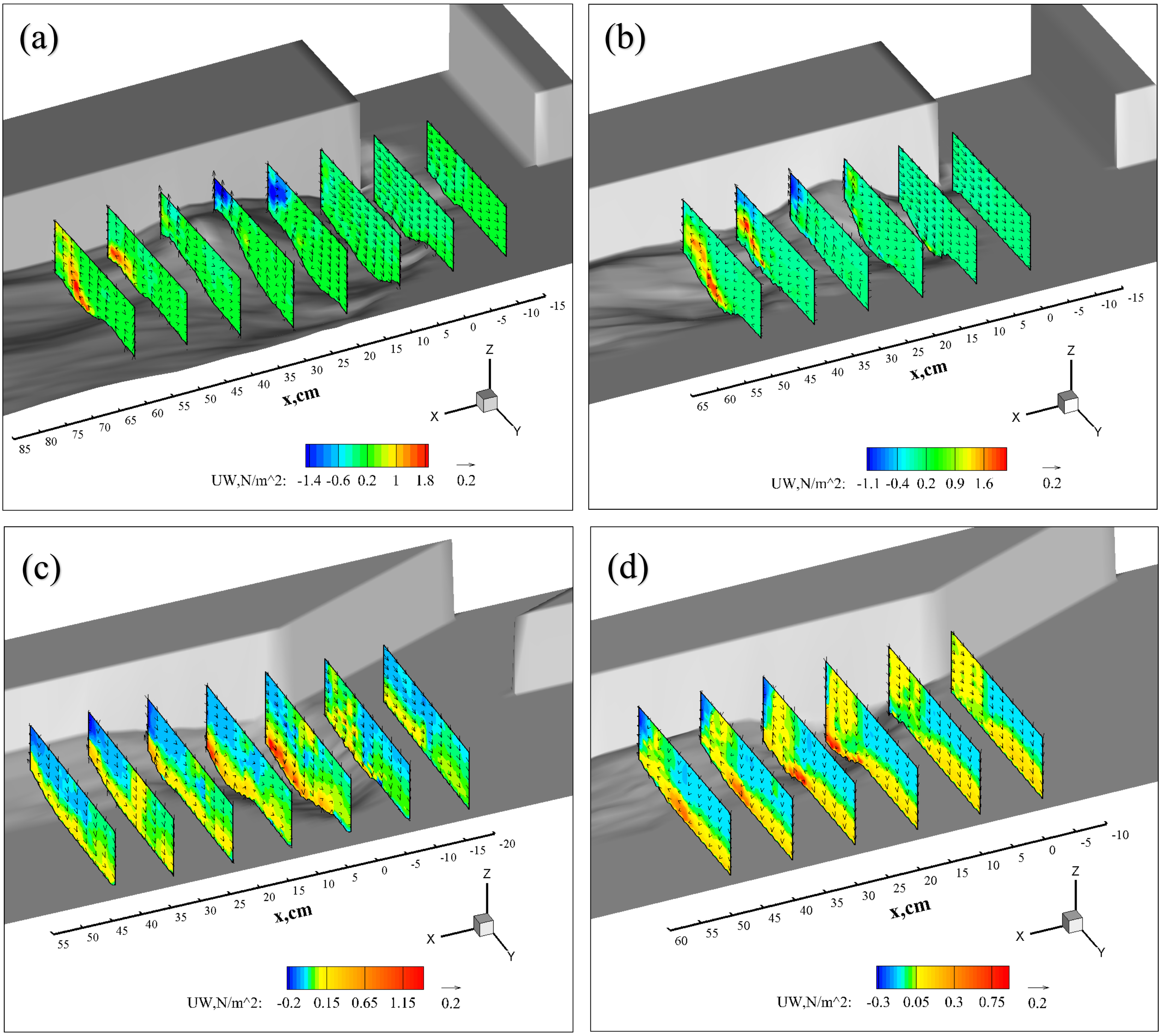

Figure 50. The Reynolds shear stress "UW" contour map for 4 cases. (a) case 90_3_2; (b) case 90_2_3; (c) case 30_3_2; (d) case 30_2_3. Note that the vectors stand for the secondary flow direction and intensity. Note use of different scales in each plot.

Interestingly, this peak UW area ends at the boundary of scour hole in case 30_3_2 (S3/S4/S5 in case 30_3_2 in Figure 50) but spreads from the bottom of the scour hole to further downstream in case 30_2_3 (S3/S4/S5/S6 in case 30_2_3 in Figure 50).

Moreover, the peak UW is higher in case 30_3_2 (1.3 m/s^2) than that in case 30_2_3 (0.9 m/s^2). This is likely because the streamwise tributary flow is accelerated suddenly above the scour hole in case 30_3_2 but is accelerated gradually from the tributary mouth to downstream in case 30_2_3 (Figure 45). The different shapes of the scour holes in case 30_3_2 and case 30_2_3 are related to these differences in location and intensity of flow acceleration.

Figure 51 shows the Reynolds shear stress UV contour map for all cases. The UV level denotes the gradient of flow velocity component U along the y-axis or the gradient of flow velocity component V along the x-axis. This shear stress component is generally regarded as an indicator of the shear layer in open channel confluence study.

It could be seen that in 90° cases (Figure 51 a&b), the maximum negative UV is located above the upstream surface of the upstream bar for case 90_3_2 (-1.30 N/m^2) and case 90_3_2 (-2.24 N/m^2), which is indicative of the flow acceleration zone (Figure 45 a&b). This negative UV area extends to the shear layer and to an average level of -1.0N/m^2 in case 90_3_2 due to the positive gradient of flow velocity component U along the y-axis. In contrast, the UV level in the flow acceleration zone decreases to about -0.1 N/m^2 at the shear layer in case 90_2_3, whose magnitude is almost 1/10 of that in case 90_3_2. Because the U gradient along the y-axis is positive in case 90_2_3 and also quite small at the shear layer, due to the tributary flow acceleration. In addition, both the upstream and downstream separation zone shows a positive level of UV due to the positive gradient of flow velocity component U along the y-axis for case 90_3_2 and case 90_2_3. The peak positive value of UV in the downstream separation area is higher in case 90_3_2 due to the higher U gradient along y-axis, as a result of higher level of flow acceleration in case 90_3_2.

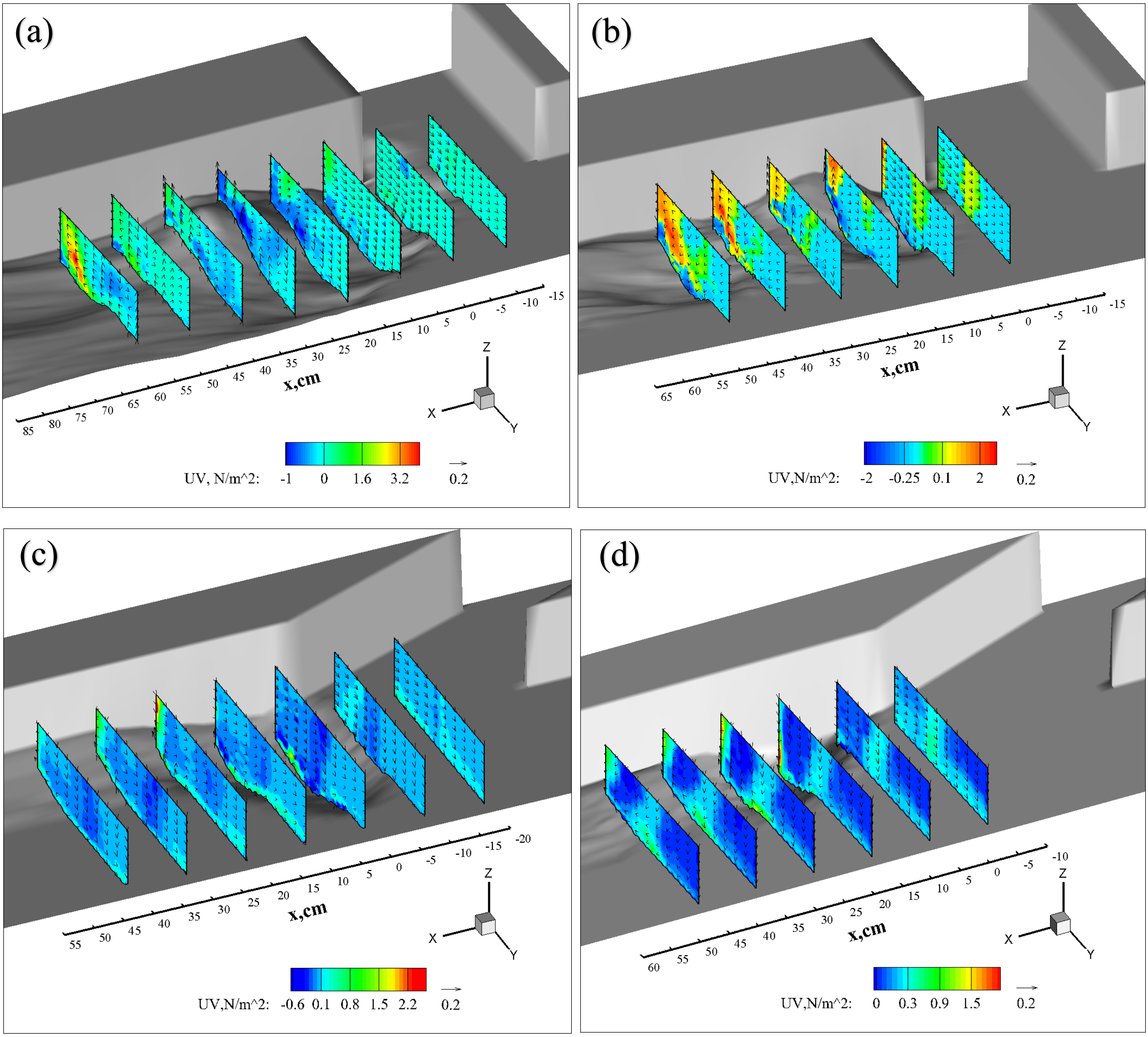

Figure 51. The Reynolds shear stress "UV" contour map for 4 cases. (a) case 90_3_2; (b) case 90_2_3; (c) case 30_3_2; (d) case 30_2_3. Note that the vectors stand for the secondary flow direction and intensity. Note use of different scales in each plot.

As for the 30° cases (Figure 51 c&d), the maximum negative UV is no longer located above the upstream surface of the upstream bar compared to 90° cases, indicating a lower level of flow acceleration. The negative UV level inside the shear layer in case 30_3_2 (about -0.35 N/m^2) is much lower than that in case 90_3_2 (about

-1.0 N/m^2), which is also indicative of a lower level of flow acceleration in case 30_3_2 than that in case 90_3_2. However, The positive UV level inside the shear layer in case 30_2_3 (about -0.35 N/m^2) is little higher than that in case 90_3_2 (<-0.1 N/m^2). This is probably because the lack of flow acceleration in case 30_2_3 brings the U gradient along the cross-stream direction closer to the discharge ratio value (2 over 3) while flow acceleration in case 90_2_3 brings the U gradient along the cross-stream direction closer to 1(for example, 2.8 over 3). The positive UV zone in 30_3_2 case and 30_2_3 case probably indicates the shear layer between the flow separation zone and the tributary flow, which shows a much smaller flow separation in 30° cases than that in 90° cases.

Figure 52 shows the Reynolds shear stress VW contour map for all cases. The VW level denotes the gradient of flow velocity component W along the y-axis or the gradient of flow velocity component V along the z-axis. This shear stress component is generally associated with radial bed shear stress, cross-stream sediment transport and secondary flow intensity.

It can be seen that a small area of positive VW is located outside the upstream separation zone in both cases 90_3_2 and 90_2_3. This is due to secondary flow at the outer side of the shear layer between the upstream separation zone and the tributary flow (Figure 47), which results in the positive gradient of flow velocity component V along the z-axis outside. This positive VW area may explain the formation of the upstream bar. Interestingly, the VW level becomes negative inside the upstream separation zone. Because the secondary flow direction inside the upstream flow separation zone is clockwise, which is different from that outside the upstream flow separation zone, which is counter-clockwise, when seeing from upstream. This high negative VW area could also be observed inside the downstream separation zone, which follows the similar reason. The consistency of positive VW area development indicates that the secondary flow inside the downstream separation zone probably generates from the secondary flow near the inner bank inside the upstream separation zone due to the widening of flow path behind the upstream bar. This area also results in the formation of the inner sand ridge.

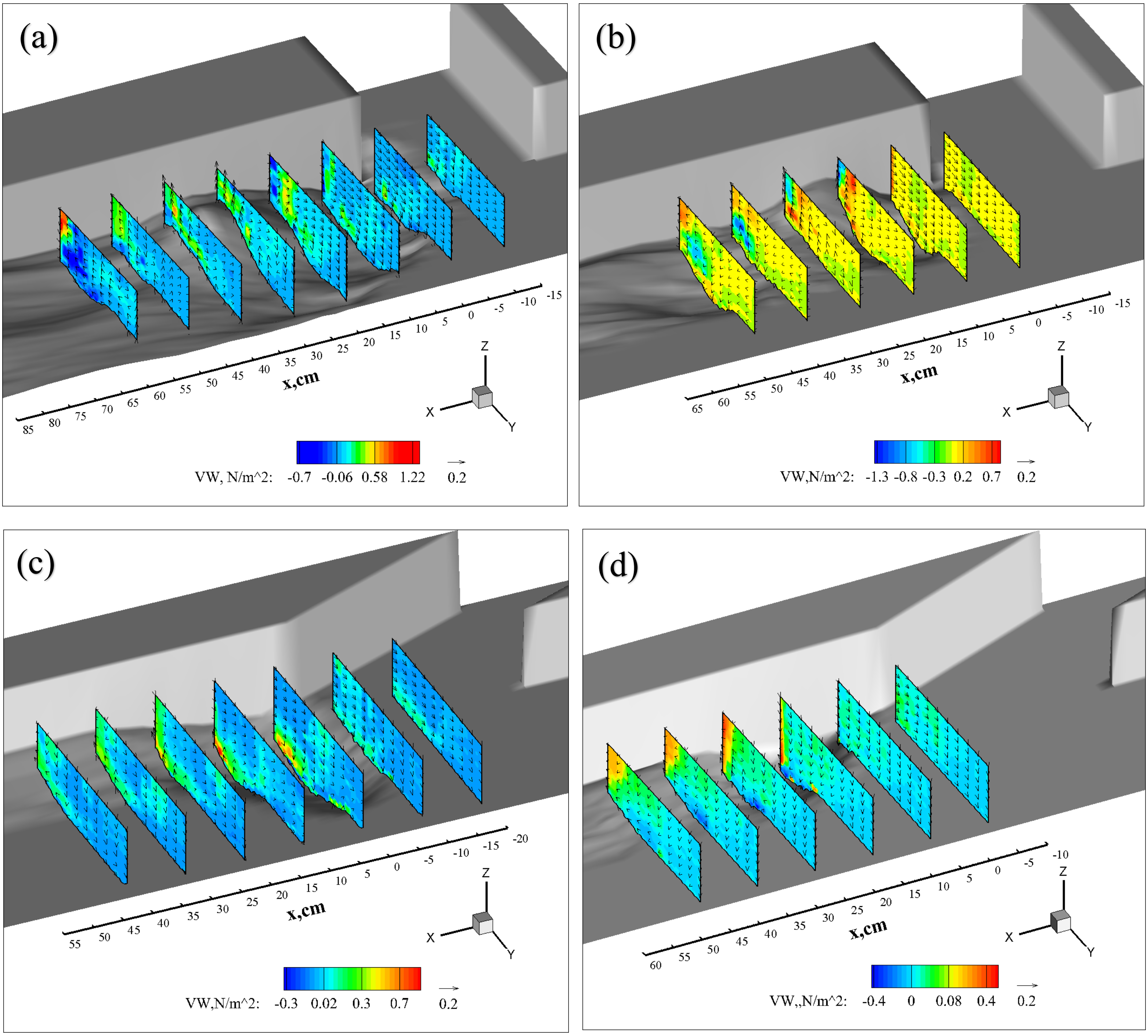

Figure 52. The Reynolds shear stress “VW” contour map for 4 cases. (a) case 90_3_2; (b) case 90_2_3; (c) case 30_3_2; (d) case 30_2_3. Note that the vectors stand for the secondary flow direction and intensity. Note use of different scales in each plot.

As for the case 30_3_2 and case 30_2_3, likewise, the area of positive VW is located at the outer side of the shear layer between the upstream flow separation zone and the tributary flow for both cases, indicative of clockwise secondary flow (seeing from upstream). There is an area of high VW level spreading from the bottom of the scour hole to the foot of the upstream bar for both cases (S3/S4/S5 in case 30_3_2 and S3/S4/S5 in case 30_2_3 in Figure 52). This spreading area has the similar spreading length in these two cases. However, this area is much wider in case 30_3_2 (nearly 3/4 of the channel width) than that in case 30_2_3 (nearly 1/3 of the channel width). This probably explained why the length of scour hole is similar for these two cases but the width of it is different. It is noteworthy that VW is positive across the spreading area in case 30_3_2 while negative in case 30_2_3, which indicates the existence of a small counter-clockwise secondary flow near the bed in case 30_2_3, having different direction with the dominated clockwise secondary flow in this two cases.

In conclusion, based on the VW results obtained from this study, the overall secondary flow range is wider in the cases with higher discharge ratio and higher junction angles. Higher discharge ratio also could bring a higher secondary flow intensity. However, higher junction angle with the same discharge ratio does not mean higher secondary flow intensity. For example, the maximum VW value in the tributary flow is higher in case 30_3_2 (0.9 N/m^2) than that in case 90_3_2 (0.2N/m^2) while the maximum VW value in the tributary flow is similar in case 30_2_3 (-0.4 N/m^2) than that in case 90_3_2 (0.7N/m^2). This is probably because the raise of total discharge rate in 30° cases resulted in the universal increase of Reynolds shear stress.

5.5 Sedimentation and Transport Pattern

5.5.1 Different Discharge Ratios

Figure 53 shows the deposition patterns for different discharge ratios in the 90° confluence, following feeding of 800 g of sediment from the mid channel of the tributary stream. The images were taken right after the feeding is done (see Appendix 1 for the images). The feeding time was consistently 10 minutes. Only the discharge ratio is different in order to control variables and study the mechanism through comparison.The red zone indicates the places where the sediment temporarily deposited, as indicated by the photo images taken immediately after cessation of sediment feeding.

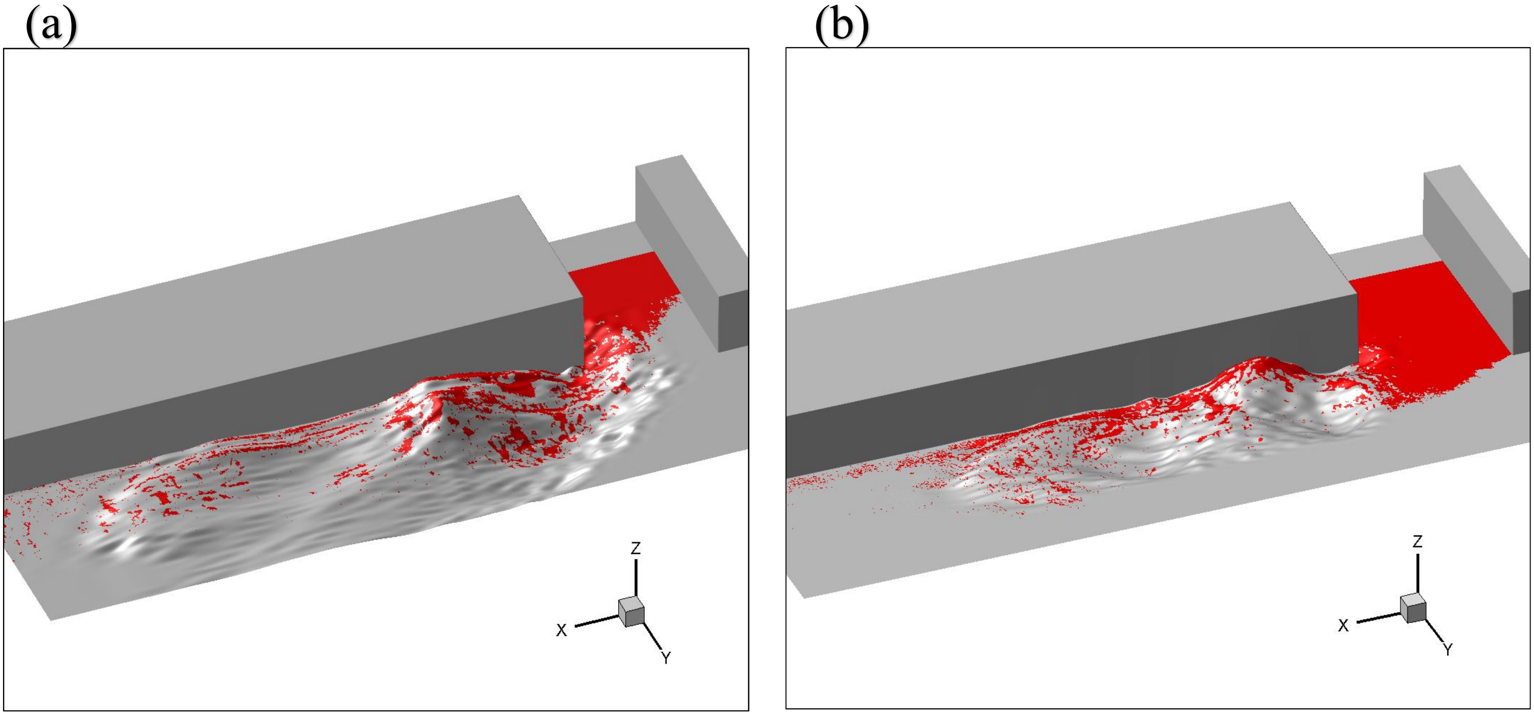

Figure 53. The sedimentation patterns for different discharge ratios in 90° confluence. (a) case 90_3_2; (b) case 90_2_3.

It can be seen that few grains deposit at the upstream corner of the channel junction when discharge ratio is 3:2 but not when discharge ratio is 2:3. Obviously, this is because the tributary flow rate is higher when discharge ratio is 3:2. The tributary flow could carry more and coarser sediment and transport them into the confluence zone, which results in less deposition in the upstream channel (Figure 53a). On the other hand, for the circumstance of discharge ratio 3:2, the coarse sediment deposit at the mouth of the tributary channel as the tributary flow moves into the main channel (Figure 53b).

Interestingly, the approximate location of the shear layer could also be indicated through the outer boundary of the sedimentation area. For the circumstance of discharge ratio 3:2, there is a noticeable secondary flow taking place in the flow acceleration zone (Figure 46). The secondary flow goes downward near the shear layer and flow rate both in x-direction and y-direction is lower. Consequently, the coarse sediment that come from the tributary channel would deposit at the inner side of the shear layer. Since there is no sediment feeding from the main channel, the shear layer is shown by the boundary of the sedimentation coming from the tributary channel (Figure 53a). In contrast, most coarse sediment has already deposited at the mouth of the tributary channel for the circumstance of discharge ratio 2:3 and the secondary flow intensity is much lower than that of discharge ratio 3:2. There would be less deposition in the confluence zone to show the location of the shear layer. The shear layer is only shown around the upstream junction corner (Figure 53b), indicative of the region of lowest flow rate around the corner, which is also noted as the “stagnation zone” (Figure 5).

There is little deposition at the scour holes in the confluence zone for either of the two cases except for the region of downwelling near the shear layer in the case of discharge ratio 3:2. This is as expected, because the scour hole is located at the flow acceleration zone which is characterized by higher flow rate. Interestingly, sedimentation could be seen at the downstream junction for both cases even though there is a scour hole located at this place. This suggests that the corner scour hole has developed equilibrium bathymetry such that bed shear stress is minimized at this location.

Both cases share the same result of sedimentation at the upstream surface of the bar and near the inner bank of the confluence zone. As noted above, this is because these features are located in the flow separation zone which is characterized by lower flow rate. In addition, there is some scattered sedimentation in the downstream area due to the lower flow rate in the flow recovery zone.

In conclusion, the variation of discharge ratio could change the sedimentation pattern near the upstream area of the confluence zone, especially around the shear layer. The post confluence area (flow recovery zone) and the separation zone share similar sedimentation features. The sedimentation pattern follows a location sequence of “Shear Layer - Separation Zone - Recovery Zone” for the higher discharge ratio while follows a different sequence of “Tributary mouth - Separation Zone - Recovery Zone” for the lower discharge ratio. This may explain the cause of bed discordance for river confluences when the tributary stream is in drought period [46].

The sedimentation under different discharge ratios in 30° confluence share the similar pattern when comparing to that in 90° confluence. The images can be seen in Appendix 1.

5.5.2 Different Junction Angles

Figure 54 shows the deposition patterns for different confluence junction angle at the same discharge ratio of 3:2. Again, 800 g of sediment were fed from the mid channel of the tributary stream for these two scenarios. The images were taken immediately after cessation of sediment feeding. The feeding time was 10 minutes. Note that the total discharge rate is raised for 30° confluence flume compared to that of 90° confluence flume in order to generate the same scour hole depth in these two cases. Except for this variable, only the junction angle is different in order to control variables and study the mechanism through comparison. The red zone indicates the places where the sediment temporarily deposited.

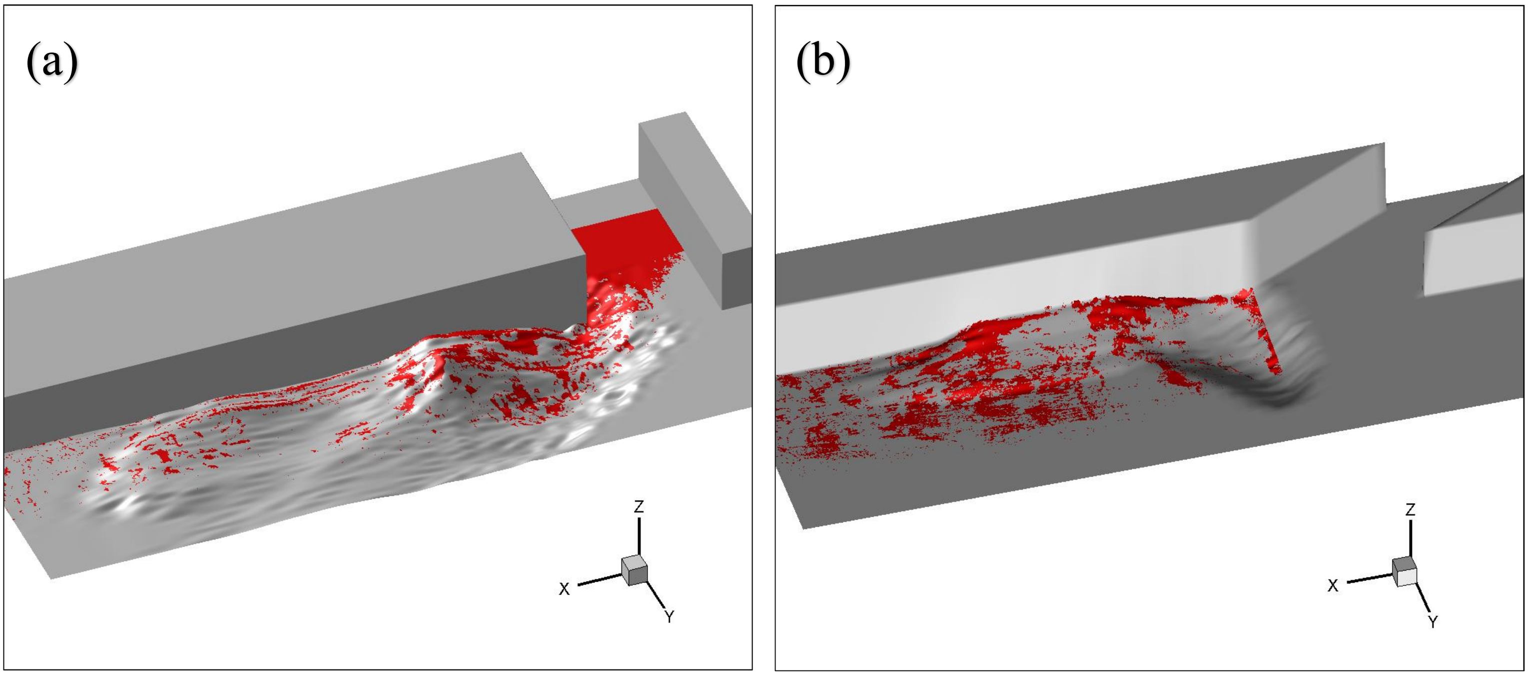

Figure 54. The sedimentation patterns for different confluence junction angles. (a) case 90_3_2; (b) case 30_3_2.

Since the total discharge rate is greater for the 30° confluence (12 L/s) compared to the 90° confluence (9 L/s), few sediment deposit at the tributary channel or tributary mouth and most are transported into the confluence area (Figure 54b). However, the interesting thing is that the overall lateral range of the sedimentation area is quite similar for the 30 and 90° confluence cases, which is about 3/4 of the downstream channel width. This may be owing to the similar location of shear layer under the same discharge ratio for the two cases.

It can be also seen that both the 30°and 90°confluences have sedimentation near the scour hole in the flow acceleration zone, where there is high downward flow, and at the upstream surface of the bar, where there is upward flow. In other words, sedimentation tends to occur at the places where there is a high level of "z-direction flow". However, due to the wider spatial domain of substantial z-direction flow in the 90° confluence, the sedimentation in these two areas is spread over a wider range in the 90° than the 30° confluence.

In addition, there is little sedimentation on the leeward part of the bar past the bar peak in the 30° confluence, perhaps because of convectively accelerated flow over the bar peak. In contrast, there are no such deposition free spaces on the bar in the 90°confluence, likely because the total flow rate is lower and longitudinal range of the bar is smaller than in the 30°confluence.

In conclusion, the general sedimentation pattern is dominated by the z-direction flow for the same discharge ratio and different junction angles. Some places may vary due to the different morphology and original flow condition.

The sedimentation under different junction angles share the similar pattern when discharge ratio is 2:3. The images can be seen in Appendix 1.

5.5.3 Different Feeding Locations

Figure 55 shows the deposition patterns for different sediment feeding location (the left bank, mid channel and right bank) angle under the same discharge ratio of 3:2, the same junction angle of 90°, with same amount of 800 g and from the same section in the tributary channel 100 cm away from the tributary mouth. The feeding time was consistently 10 minutes. The sediment was fed under the water near the free surface of the flow. The left and right bank feeding location is 5 cm away from the bank and the mid channel feeding is 15 cm away from both banks. The images were taken immediately after completion of the sediment feeding. The red zone indicates the places where the sediment temporarily deposited.

The sediment fed from the right bank of the tributary are transported by the flow along the inner bank. The coarser sediment deposit in the flow separation zone, whereas the fines translate over the bar and deposit at the back of the bar where the flow diverges. The amount of sedimentation at these two areas may have been approximately equal, given the relatively equal proportions of coarse and fine sediment in the colored sand.

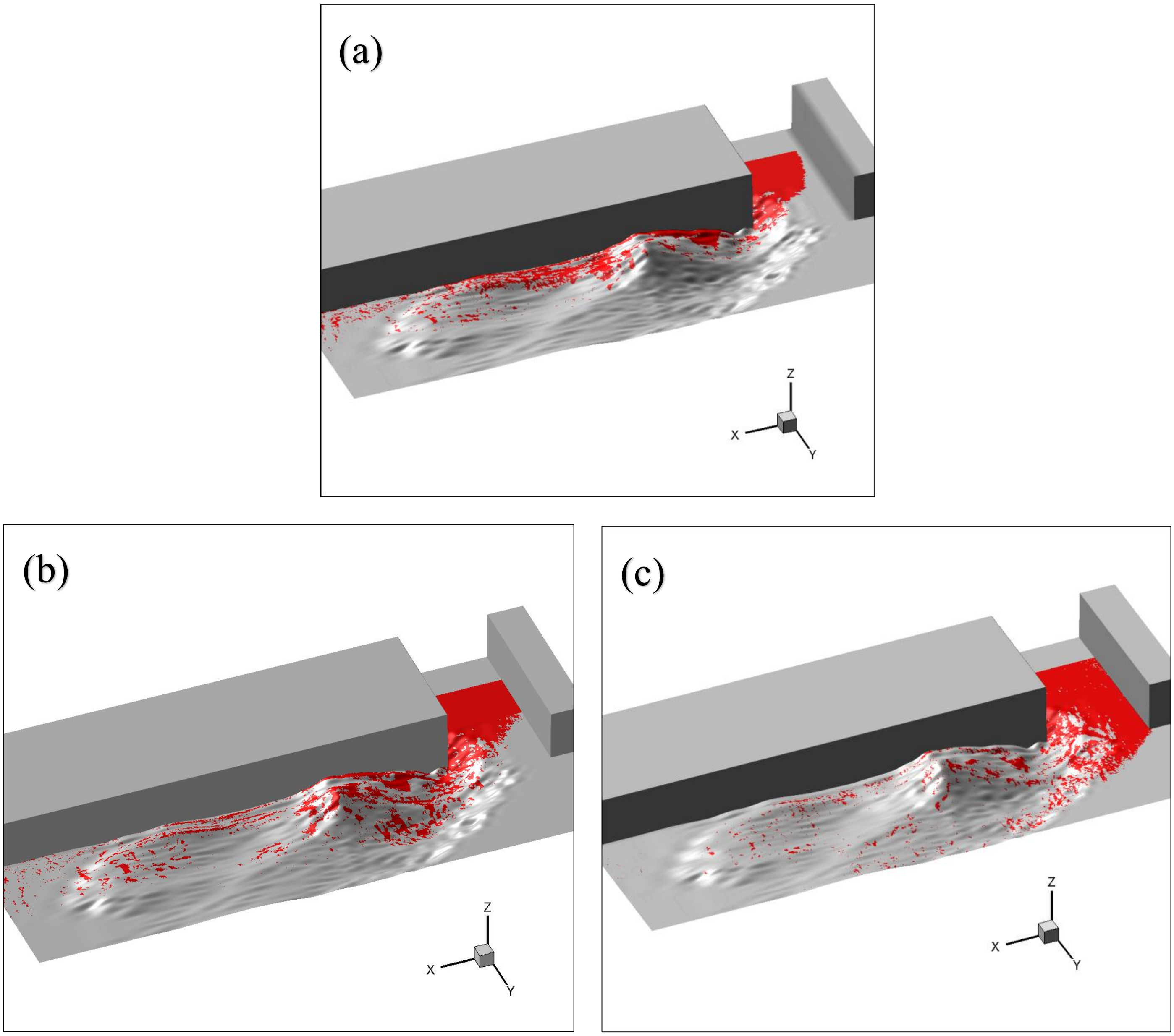

Figure 55. The sedimentation patterns for different feeding locations in case 90_3_2. (a) Fed from the left bank of tributary; (b) Fed from the mid channel of tributary; (c) Fed from the right bank of tributary.

When fed from the mid channel, most the sediment tends to deposit in the scour hole due to the strong downwards flow, as well as in the low velocity flow separation zone. Less sedimentation could be observed at the back of the bar and in the flow recovery zone.

Interestingly, most sedimentation could be seen near the upstream corner of the confluence flume when the sediment were fed from the left bank of the tributary channel. This occurred because most sediment follow the flow path near the left bank of the tributary channel towards the lower velocity stagnation zone. Some sediment also deposited near the scour hole due to the downward flow. Still, the sedimentation is much less in this area in this case compared to the case of feeding from the mid channel. Moreover, much less sedimentation could be observed at the back of the bar and the flow recovery zone.

In conclusion, different sediment feeding locations produce different sedimentation patterns due to the change in sediment transport pathways through the various confluence hydrodynamic zones.

The sedimentation of three feeding locations for other junction angles and discharge ratios share the similar pattern. The images can be seen in Appendix 1.

5.5.4 Time Series

Figure 56 shows the deposition patterns for different time series (0h, 1h, 2h and 3h) under the same discharge ratio of 3:2 and the same junction angle of 90°, with the same amount of 4000 g and from the same feeding location of mid channel. The sediment is fed under the water near the free surface of the flow. The sedimentation pattern does not change much after 3 hours of scouring. The red zone indicates the places where the sediment temporarily deposited.

Figure 56a shows that the sediment tends to deposit initially at the mouth of the tributary channel, at the bottom of curved scour hole, the top of the upstream bar and the face of the downstream bar. Little sedimentation is found on the upstream face of the upstream bar and the front of the downstream scour hole. The original sedimentation pattern in 0 h is mainly determined and limited by the sediment transport capacity of the tributary stream when feeding sediment constantly into the channel. Most areas are covered with sediment except for the places with highest TKE, UV, UW and flow velocity, such as the upstream face of the upstream bar, or with high level of upwelling flow, such as the front of the downstream scour hole.

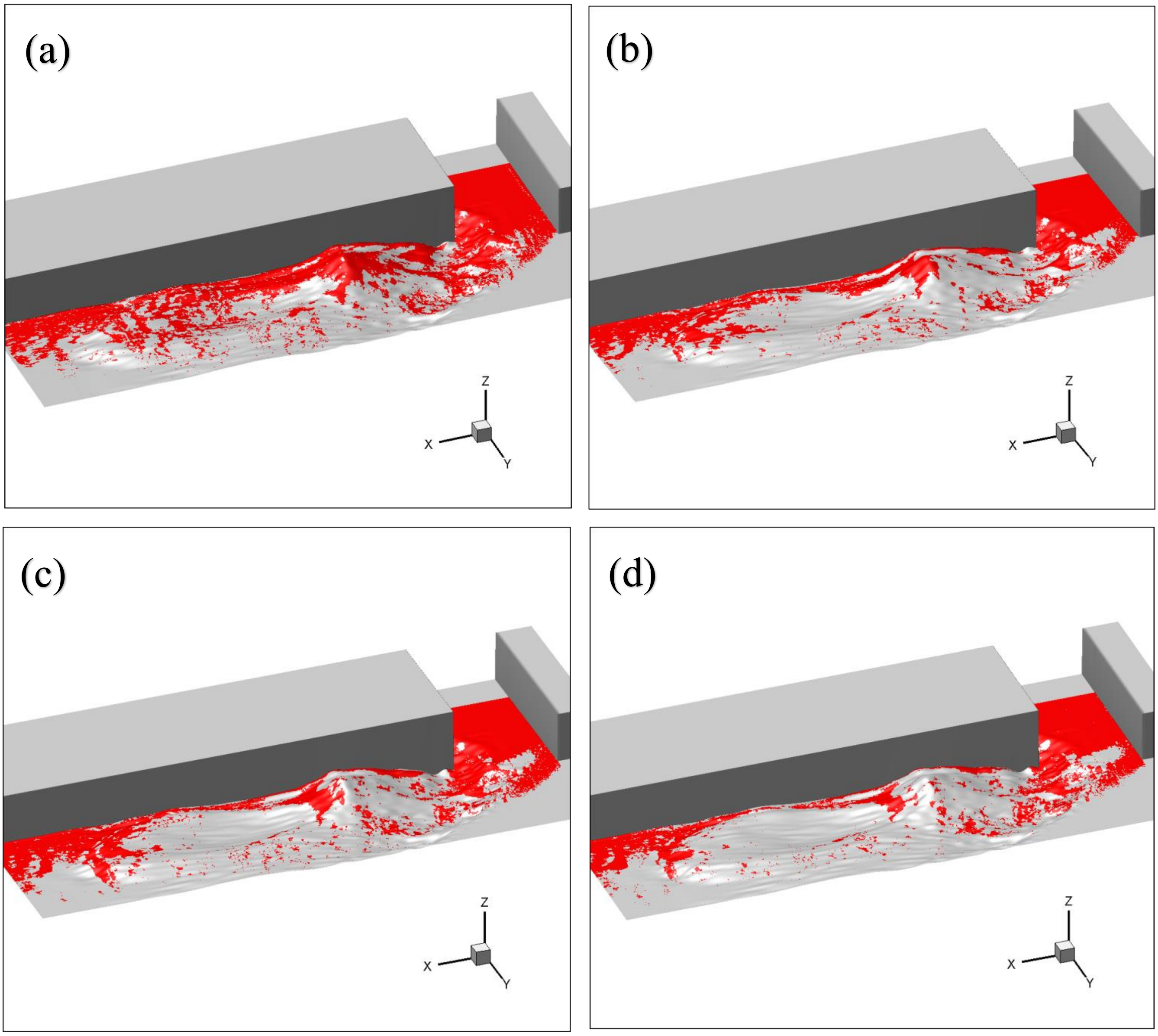

Figure 56. Time series of the sedimentation patterns for case 90_3_2. (a) The image taken right after the feeding is done (0 h); (b) The image taken 1 hour after the feeding is done (1 h); (c) The image taken 2 hours after the feeding is done (2 h); (d) The image taken 3 hours after the feeding is done (3 h).

After one hour most sediment initially on the upstream face of the upstream bar have been transported to the downstream side (Figure 56b). This is likely due to the high level of TKE, Reynolds shear stress and flow velocity around this area. Some of the sediment deposited at the upstream scour hole have also been taken away. It is probably due to the high TKE level inside the shear layer, which is right above the upstream scour hole. Interestingly, a new scour area is generated in front of the upstream scour hole. The location and tilting direction show that this new area is also located beneath the shear layer. However, the equilibrium bed morphology state is flat in this area, suggesting this is a location of relatively low bed shear stress. Perhaps the finer gradation of the additional sediment, compared with the original bed sand, allows for transport despite relatively low Reynolds shear stress. In addition, the sediment inside the downstream scour hole are also taken away due to the high level of TKE and Reynolds shear stress in this area. In contrast, sediment remain deposited near the inner bank because of the low flow velocity inside the separation zone. The sediment on the inner sand ridge also remain because of the downwelling flow above it.

After two and three hours of running (Figure 56c and 56d), most places which scoured after 1 hr demonstrate expanded scour zones, especially for the new-developed scour area, the upstream face of the upstream bar and the downstream scour hole. However, no additional sediment has been transported from the upstream scour hole. It is reckoned that because coarser sediment deposited in this area. Furthermore, sediment continue to be observed in most places where sedimentation remained after 1 hour, such as the inner sand ridge, the separation zone and the foot of downstream bar. In addition, the foot of the downstream bar seems to accumulate more and more sediment as the run progresses, likely because this place lies in the flow recovery zone. Sediment taken away from the upstream zones and the downstream scour hole tend to accumulate in this area. Finally, the sedimentation around the top of the upstream bar tends to move to the back side (downstream side) of the bar. This is likely because the upwelling flow and Reynolds shear stress are higher in the upstream face than the downstream face of the upstream bar.

5.5.5 Feeding Amount

Figure 57 shows the deposition patterns for different sediment feeding amounts (800 g and 4000 g) under the same discharge ratio of 3:2 and the same junction angle of 90° from the same feeding location of mid channel. The pictures were taken right after the cessation of feeding. The red zone indicates the places where the sediment temporarily deposited.

It can be seen that most areas of sedimentation when feeding 800 g tend to have more sedimentation when feeding 4000 g, such as the inner bank area and the places around the top of the upstream bar and around the downstream scour hole. The shape of the sedimentation area is also quite similar under different feeding amount, which proves that the sedimentation pattern is mostly determined by the flow field and the equilibrium bed morphology. Interestingly, the sediment tends to go further to the outer side of the shear layer between the tributary and the mean stream and deposit under it when feeding 4000 g. That's because the flow velocity in y-axis is quite high at the inner tributary mouth but gets lower and lower when approaching the shear layer. The fine sediment in the tributary flow will move with the flow into the flow acceleration zone due to that high level of flow velocity. The coarse sediment which could not be carried by the flow tend to move to the downwelling flow and deposit at the outer side of the shear layer due to the low level of flow velocity.

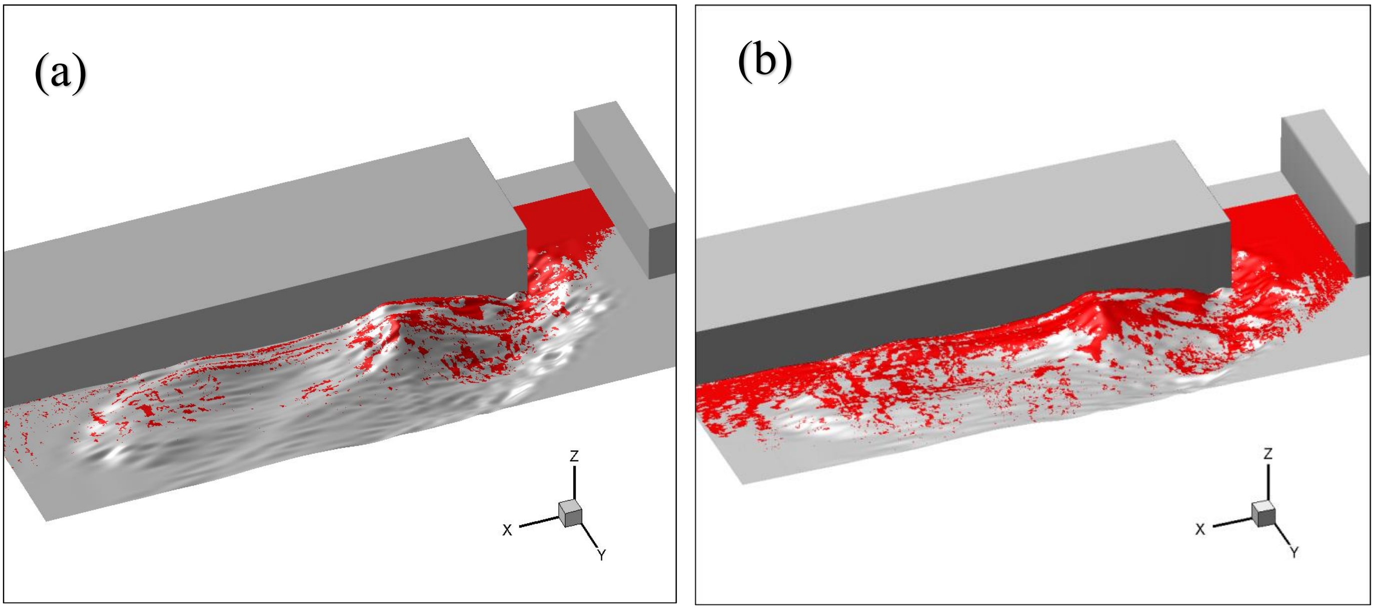

Figure 57. The sedimentation patterns for different feeding amount for the case 90_3_2. (a) Feeding amount = 800 g. (b) Feeding amount = 4000 g.

Chapter 6 Discussion

One of the motivations for this study was to understand how contaminated sediment transported from a tributary deposit in a main channel. An open channel confluence area can undergo a high level of sediment and pollutant transport due to flow joining and mixing. Confluences can also be relatively rich ecologically due this mixing. Many varieties of aquatic animals live, reproduce and migrate in this area. Studying the transport of sediment and pollutants in open channel confluences is of great importance for aquatic environment protection and pollution control. However, the complex interaction between flow, sediment and the bed condition make it hard to study and predict the pollutants transport pattern. The variation of discharge ratio during different hydrological period and the variation of junction angle due to the channel evolution also bring extra difficulties to the study.

A physical hydraulic model usually serves as a tool for investigating the patterns, studying the mechanisms and solving problems in real hydraulic engineering issues economically and conveniently. In order to ensure the guidance values of a physical model to a real model, the scaling issues between them should be considered carefully. The scaling issues generally include three aspects: geometric similarity, kinematic similarity and dynamic similarity. Geometric similarity requires similarity in all length dimensions. Kinematic similarity indicates a similarity of motion between model and prototype particles. Dynamic similarity requires that all force ratios in the two systems are identical.

For the geometric similarity, The length scale, λ_l, is determined by:

$$\lambda_l = \frac{L_m}{L_p} \tag{8}$$

Where L stands for “length” and the subscripts m and p stands for the model scale and the prototype scale, respectively. For open channel studies, the gravitational force is the dominated force other than the inertial force. Following that, the Froude scaling principle should be applied for dynamic similarity, which is given as:

$$Fr_m = Fr_p \quad \text{or} \quad \frac{{v_m}^2}{g_m L_m} = \frac{{v_p}^2}{g_p L_p} \tag{9}$$

Where Fr stands for the Froude number, v stands for the flow velocity and g is the gravitational acceleration. From (8) and (9), the velocity scale, λ_v, and time scale, λ_t, for kinematic similarity could be derived as:

$$\lambda_v = \lambda_t = {\lambda_l}^{0.5} \tag{10}$$

From (8), (9) and (10), assume that the water density, ρ_w, is equal for the prototype and physical model (i.e. $\lambda_{\rho_w} = 1$), the Reynolds shear stress scale, λ_τ, and turbulent kinetic energy, λ_{TKE}, could be derived as:

$$\lambda_\tau = \lambda_{TKE} = \lambda_l \tag{11}$$

Concerning the scales related to sediment transport, direct Froude scaling of a volumetric transport rate would yield

$$\lambda_{Q_s} = {\lambda_l}^{2.5} \tag{12}$$

For the tributary sediment feeding rate scale, λ_{Q_s}. Conversion of a volumetric transport rate to mass transport rate would require the assumption that the grain density, ρ_s, is equal for the prototype and physical model (i.e. $\lambda_{\rho_s} = 1$). More usefully, the non-dimensional transport rate (Φ) can be used as a scaling parameter by setting it equal in model as prototype [64]:

$$\Phi = \frac{g_s}{\rho_s \sqrt{g\left({(\rho_s - \rho_w)}/{\rho_w}\right) d^3}} \tag{13}$$

where g_s is the mass transport rate per unit width and d is the grain diameter. However, the sediment size scale is often different from geometric scaling because very fine particles have cohesive properties. The usual way of sediment size scale derivation is based on the the velocity scale and Shields' curve to ensure scaled entrainability of bed sediments.

There have been relatively few field studies on the pollutants transport and sedimentation pattern in open channel confluences. Furthermore, the initial equilibrium bed state generation is little considered in most studies concerning pollutants transport.

For example, [60] [56] studied the concentration of phosphorus near the bed in an open channel confluence flume under the condition of evenly distributed phosphorus concentration inside the flume. Results shows that the area of high phosphorus concentration is mainly located beneath the shear layer due to downwelling flow. However, a clay plate was used for the bed to capture deposited phosphorus, which inhibited re-exchange of phosphorus from the bed to the flow. Moreover, not all pollutants are soluble. Most Many pollutants sorb to and are transported with sediment particles. This experiment did not model these conditions.

The study by [30] is the most relevant recent research of the confluence sedimentation pattern under a constant sediment feeding condition in the tributary channel. However, the diameter of additional sediment was chosen too coarse and too even; consequently, most of the sediment deposited along the tributary flow. No sedimentation nor evolution patterns are found in the results. Moreover, [30] [60] [56] share the same flaws where the confluence bed morphology is not equilibrium state but flat when the feeding starts, which could not mimic the real cases.

In contrast, first, the size of additional sediment in this study were carefully chosen through pre-tests in order to find the ones that could deposit in the confluence area but not within the tributary channel itself. The gradation of additional sediment in this study was also set to be sufficiently wide to ensure both suspended load and bed load transport, which could model all modes of contaminated sediment transport except for the dissolved pollutants. The sediment moved in suspension until they were initially deposited. Some of this initial deposition occurred in the confluence after exiting the tributary. Subsequent transport (i.e. time-series evolution) was as bedload.

Second, The flow field measurements and sediment feeding were done after the equilibrium bed state generation and consolidation in this study, which makes it clearer to compare the different scouring and sedimentation pattern for bed and additional sediment. Note that the equilibrium bed morphology state in this study is developed under clear water scour condition and then consolidated. Additional introduction of mobile sediment breaks the equilibrium state and may cause deposition above the bed. If the equilibrium bed state is not consolidated and the feeding experiments are carried out under live-bed state, the additional sediment would have interactions with the bed materials and results in different bed morphology.

As for the bed condition, the studies done by [60] [52] [56] [42] used the mixture of two different sizes of sand grains as the bed material in order to quickly generate scour holes and an equilibrium bed state. However, the present study utilized a naturally poorly sorted river sand and appropriately scaled discharge rates, allowing for generation of more realistic morphological features, such as the curved boundary of the upstream scour hole in case 90_3_2, the mid channel hole in case 90_2_3 and the development of the downstream scour hole.

However, there are also some shortcomings and limitations that should be modified and improved in this study for further exploration:

1. The total discharge rate was increased for the 30° cases compared with 90° cases in order to generate a degraded bed condition. This was done to ensure the maximum scour hole depth was the same for each case with the same discharge ratio. However, the total discharge rate is an additional variable that should not be involved when explaining the mechanism of junction angle variation. And it has been proved that different total discharge rates will result in different equilibrium bed morphology even if other variables are kept the same through pretests. It would be better if the 30° cases are replaced with some other cases with higher junction angles such as 50 degrees or 70 degrees where the bed morphology could change when applying the same total discharge rate as the 90° cases.

2. For the ADV data processing, the raw data filter condition in this thesis is different from the traditional condition of signal noise ratio (SNR) and correlation. It is determined both by the noise ratio, which considers both the absolute noise level and the turbulent level. This new filter condition could avoid filtering out the data with high noise caused by high turbulent level and make the TKE and Reynolds shear stress results more accurate. However, it would possibly filter out the data with medium noise level and low turbulent level, resulting in overall TKE results a little higher than the actual values. Some of these data should probably be kept. So it would be better if the noise ratio and SNR are both applied as the filter condition. We can determine which variable is more reasonable to use based on different turbulent levels.

3. The noise may cause an uncertainty of about 10% for the time-averaged cross-stream velocities (V, W), 15% for the turbulent shear stresses, and 20% for the turbulent normal stresses [14]. The time-averaged cross-stream velocity uncertainty level in this study is less than 10%. However, the time-averaged Reynolds shear stress uncertainty level is much higher than 15% for some measurement samples. The results are shown in Figure 58.

The relative filtered amount is determined:

$$\Delta \mathrm{F} = \frac{RSS' - RSS_r}{RSS_r} \tag{14}$$

ΔF is the relative filtered amount, RSS' is the Reynolds shear stress after filtering, $\mathrm{RSS_r}$ is Reynolds shear stress in raw data. It can be seen that the filtered Reynolds shear stress deviates quite far from the raw data for some filtered samples when the filter condition is applied. Although there are not many filtered samples with high ΔF among all filter samples and it has little impact on the Reynolds shear stress contour map, the abnormal high filter amount still indicates that the filter condition could be modified and improved.

4. The flow field data series of one sample should be excluded in data converting process if the nominal velocity range is improperly set in the Vectrino software interface during the measurements. However, it could not be identified through the Matlab code in this thesis and needs to be excluded manually. New code needs to be developed so that these samples could be identified and excluded.

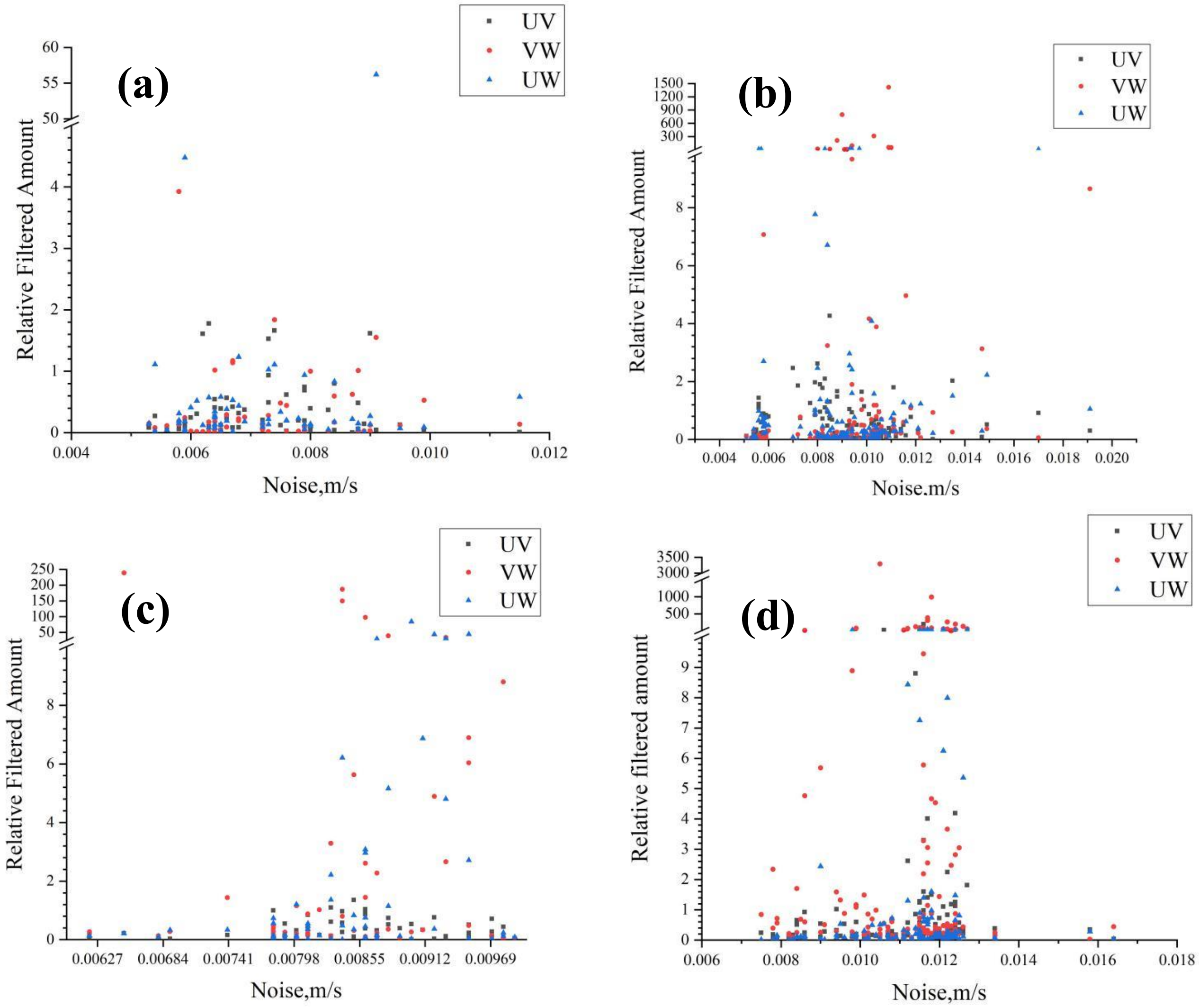

Figure 58. The relative filter amount for the filtered samples in 4 cases. (a) case 90_3_2; (b) case 90_2_3; (c) case 30_3_2; (d) case 30_2_3.

5. The number and locations of measured cross sections are set based on the range of the bed morphology development. It would be more convenient to compare among cases if the number and locations of measured cross sections are the same. In addition, the flow field near the flow surface and the bank is not measured in this study. The flow field would be completely measured if PIV or side-oriented ADV is applied.

6. Using grout as the consolidation material can generate the hardest and most stable bed condition for further measuring and sediment feeding. However, it could cover some bed surface details. It can also change the bed roughness which will disturb the velocimetry and the sedimentation pattern when feeding addition sediment. Other

materials should be applied in the consolidation process such as glue. And the bed roughness and bathymetry should be measured before and after the consolidation.

7. The feeding rate and concentration is hard to control when feeding manually. It would be better if the additional sediment could be wet and fed automatically through independent equipment directly into the upstream flow. In addition, due to the original flow rate setup, the grain size range of the additional sediment was quite small. The sedimentation patterns would be clearer if the additional sediment could be separated into two groups and colored differently based on the grain sizes. And the sediment transportation paths could be seen if they are covered with water-proof fluorescent material.

Chapter 7 Conclusion

7.1 Conclusion

This study put forward a systematic methodology on experimental open channel confluence research, which considers almost all factors that mainly affect the flow field and sediment transport pattern, including discharge ratio, junction angle, sediment feeding location, feeding amount and sedimentation evolution pattern. The flow field parameters including flow velocity, turbulent kinetic energy and Reynolds shear stress are thoroughly investigated and analyzed. The innovation of this study has the following three aspects.

- The deposition pattern of incoming tributary sediment was assessed. Discharge ratio, confluence junction angle, sediment feeding location, feeding amount and time-series evolution pattern were all taken into consideration when investigating the sediment transport pattern.
- The bed morphology is generated from initial flat bed condition after 24 hours of scouring. All measurements and additional sediment feeding are carried out based on that equilibrium bed state, which is closer to real confluence river sediment transport cases. The bed sand in this study was excavated from a real river bed and the flume model is designed also based on real river confluences;
- The size of additional sediment is determined based on several pre-tests in order to ensure the sediment would mostly deposit at the confluence area but not at the tributary channel. The size range is set to be as wide as possible to mimic all modes of contaminated sediment transport in real river cases;

Both the equilibrium bed morphology and the sedimentation patterns are highly related to the flow field in confluence area, especially the Reynolds shear stress parameter. Several conclusions which haven't been raised before could be drawn in this research, which are listed below:

- Under the discharge ratio and junction angle setups in this study, the confluence junction angle seems to dominate the general patterns of equilibrium bed morphology and pollutants transport pattern while the variation of discharge ratio plays a secondary role. This is probably because the junction angle variation has a bigger impact on the tributary flow path and secondary flow pattern compared with discharge ratio. It is also found that there is no scouring or deposition taking place in 30° cases when keeping the total discharge rate equal to the 90° cases.

- The flume experiment in this study shows that the equilibrium bed morphology in 90° cases is characterized by a cone-shaped upstream bar. The equilibrium bed morphology in 30° cases is characterized by a ribbon-shaped bar. It indicates that the formation of upstream bar is highly related to shape and location of flow separation zone. The corner scour hole presents in all cases probably due to the high velocity gradient caused by abrupt flow turning. The mid channel scour hole is generated by the high Reynolds shear stress in the shear layer. The emergence of a downstream scour hole highly relies on the shape of flow separation zone and the bar inside it.
- In this study, the mid channel scour hole only exists in high discharge ratio cases (90_3_2 and 30_3_2) or low discharge ratio cases with high junction angle (90_2_3). And it is much smaller in the latter case than the former cases. Moreover, it seems that higher discharge ratio will cause a wider range of mid channel scour holes.
- Based on the flume configuration in this study, there are two helical cells in 90° cases: one is the tributary flow in the flow acceleration zone, the other is in the separation zone near the inner bank. Due to the wake flow behind the cone-shaped upstream bar, the inner secondary flow continues to exist and forms the downstream separation zone, characterized by high TKE, Reynolds shear stress and a helical cell inside it. No downstream separation zone or scour hole is observed in 30° cases, which is probably because of the absence of wake flow effect due to ribbon-shaped upstream bar.
- Based on the additional sediments and feeding approaches used in this study, the overall sedimentation pattern seems to follow the equilibrium bed

morphology pattern for all four cases. In other words, the upstream sand bar, downstream sand bar and the sand ridges usually witness additional deposition due to low flow rate. The scour holes usually witness no deposition due to high Reynolds shear stress and high flow rate. However, sedimentation could also occur in the mid channel scour hole right after the feeding is done due to the strong downwelling flow in the shear layer. Moreover, where there is no scouring at the tributary mouth in equilibrium bed morphology, there is scouring when feeding sediment, likely because the medium size of additional sediment is smaller than the bed sand.

- In this study, the sedimentation pattern is quite different when fed from different locations. This indicates that under the flow conditions in this study, sediment particles coming from the tributary channel probably move along different stream layers, and there is little exchange between adjacent layers.
- Based on the results obtained from this study, it is reckoned that the undissolved contaminants tend to deposit and accumulate at the mid channel scour hole, near the inner bank and the downstream face of the upstream bar in open channel confluence areas.

7.2 Future Work

In future work, the author intends to cover the whole cross-sectional flow field measurement in order to bring more credibility to the sediment transport and bed morphology evolution pattern analysis. Furthermore, real river confluences will be studied in the field. Field data for the study would include measurements of incoming flow rate, 3D velocities, temperature, bed morphology, entrained sediment (bedload as well as suspended load) concentration and transport rate. The potential instruments that could be employed in field measurements include: The Global Positioning System (GPS), the Acoustic Doppler Current profiler (ADCP), the Handheld Thermal Infrared (TIR) imagery and passive-integrated transponder (PIT).

The author will choose at least two field sites with different confluence angles and momentum ratios. He will collect data over two field scenarios and use them to build numerical morphodynamics models. He will use the morphodynamics models in a parametric study to evaluate the influence of confluence angle and momentum ratio on confluence morphodynamics and mixing characteristics. This study is a further exploration on the flow and sediment transport patterns in open channel confluences. It is expected that the new sediment tracing and temperature mapping technology could work fine in confluences and help us have a better understanding about the interaction mechanism between flow, sediment and bed morphology. The similarities and differences when comparing this study with previous ones will be pointed out and clearly explained. It is also expected to develop a numerical model which could fit well with the actual case. Moreover, the results differences between flume and in situ experiments should be deeply studied in order to help improving the flume design for better simulation.

References

[1] Antonelli M, Klaus J, Smettem K, Teuling AJ, Pfister L. 2017. Exploring Streamwater Mixing Dynamics via Handheld Thermal Infrared Imagery. J. Water 2017, 9, 358; DOI: 10. 3390/w9050358.

[2] Ashmore PE, Parker G. 1983. Confluence scour in coarse braided streams. Water Resour Res, 19 392-402.

[3] Ashmore PE, Ferguson RI, Prestegaard KL, Ashworth PJ, Paola C. 1992. Secondary flow in anabranch confluences of a braided, gravel-bed stream. Earth Surf Process Landforms, 17 299-312.

[4] Baranya S, Olsen NRB, Józsa J. 2013. Flow analysis of a river confluence with field measurements and RANS model with nested grid approach. DOI: 10.1002/rra.2718

[5] Best, JL. 1986. The morphology of river channel confluences. Prog Phys Geogr, l0157-174

[6] Best JL, Reid, I. 1984. Separation zone at open-channel junctions. Journal of Hydraulic Engineering, 110, 1588-1594. DOI: 10.1061/ (ASCE) 0733-9429(1984)110:11(1588).

[7] Best JL. 1985. Flow dynamics and sediment transport at river channel confluences: Unpublished Ph.D. Thesis, Birkbeck College, University of London, 393 p.

[8] Best JL. 1987. Flow dynamics at river channel confluences: Implications for sediment transport and bed morphology. In F. G. Ethridge, R. M. Flores, & M. D. Harvey (Eds.), recent developments in fluvial sedimentology (pp. 27–35). Tulsa:SEPM Society for Sedimentary Geology.

[9] Best JL. 1988. Sediment transport and bed morphology at river channel confluences. Sedimentology, 35, 481–498. DOI: 10. 1111/j. 1365-3091. 1988. Tb00999. x

[10] Best JL, Rhoads BL. 2008. Sediment transport, bed morphology and the sedimentology of river channel confluences. In River Confluences, Tributaries and the Fluvial Network, Rice SP, Roy AG, Rhoads BL (eds). John Wiley &

Sons: Chichester; 45–72. DOI: 10. 1002/9780470760383. ch4.

[11] Biron PM, Serres BD, Roy AG, Best JL. 1993. Shear layer turbulence at an unequal depth channel confluence. In: Clifford, N. J., French, J. R., Hardisty, J. (Eds.), Turbulence: Perspectives on Flow and Sediment Transport. John Wiley, Chichester, UK, pp. 197–213.

[12] Biron P, Best JL, Roy AG. 1996. Effects of bed discordance on flow dynamics at open channel confluences. J Hydraul Eng 122(12):676–682.

[13] Biron PM, Ramamurthy AS, Han S. 2004. Three-dimensional numerical modeling of mixing at river confluences. J Hydraul Eng 130(3):243–253.

[14] Blanckaert K. 2010. Topographic steering, flow recirculation, velocity redistribution, and bed topography in sharp meander bends. Water Resource Research. 46, W09506.

[15] Boyer C, Roy AG, Best JL. 2006. Dynamics of a river channel confluence with discordant beds Flow turbulence, bed load sediment transport, and bed morphology. Journal Of Geophysical Research, VOL. 111, F04007, DOI: 10.1029/2005JF000458, 2006.

[16] Chen JQ, Liu XL, Zhao WX, Ding JP. 2005. Numerical Simulation on Confluence of the Two Rivers in Chongqing City. Journal of Chongqing University (Natural Science Edition). Vol.28 No.8.1000-582X (2005)08-0135-03.

[17] Chen L, Duan T, Yan T, Liu TH, Zhu XK. 2013. Study on Sediment Deposition Characteristics at River Confluence in Reservoir Area. Journal Of Sichuan University (Engineering Science Edition). Vol.45 No.3. 1009-3087(2013) 03-0057-06.

[18] Dietrich WE. 1987. Mechanics of flow and sediment transport in river bends. Environment and Process, Richards KS (ed). Basil Blackwell: Oxford; 179–227.

[19] Firooz R. 2014. The effect of confluence angle on the flow pattern at a rectangular open-channel. J. Engineering, Technology & Applied Science Research Vol. 4, No. 1, 2014, 576-580.

[20] Guillén-Ludeña S, Franca MJ, Cardoso AH, Schleiss AJ. 2015. Morphodynamics

In River Confluences. R. E-proceedings of the 36th IAHR World Congress 28 June – 3 July, 2015.

[21] https://www. vcg. Com/creative/805998748.

[22] http://www. nycsgl. gov. cn/html/2014/yw_1009/2608. html.

[23] https://www.gettyimages.ca/detail/photo/beginningof-los-angeles-river-at-high-res-stock-photography/586897675.

[24] https://www.homedepot.com/p/Bosch-130-ft-Laser-Distance-Measurer-DLR130K/202504985

[25] https://www. travelchinaguide. com/river/yangtze/.

[26] https://geo-matching.com/category/current-meters/vectrino.

[27] Jamieson EC, Post G, Rennie CD. 2010. Spatial variability of three-dimensional Reynolds stresses in a developing channel bend. Earth surface processes and landforms 35, 1029–1043 (2010). DOI: 10.1002/esp.1930.

[28] Kashyap S, Doutreleau B, Bou-botros G, Rennie CD, Townsend R. 2010. A semi-permanent method for fixing sand beds in laboratory flumes. Journal of Hydraulic Research Vol. 48, No. 3 (2010), pp. 377–382.DOI:10.1080/00221686.2010.481831.

[29] Kato C, Sakuma M. 2011. Application of full-resolved large eddy simulation to unsteady fluid flow and aero-acoustics predictions. Proceedings of seventh international symposium on turbulence and shear flow phenomena (TSFP-7), Ottawa, Canada.

[30] Leite Ribeiro M, Blanckaert K, Roy AG, Schleiss AJ. 2012. Flow and sediment dynamics in channel confluences. Journal Of Geophysical Research, VOL. 117, F01035, DOI: 10.1029/2011JF002171, 2012.

[31] Lira VMP. 2014. Numerical modeling of a 90° open-channel confluence flow using OpenFOAM CFD.

[32] Li DH. 2017. Water Level characteristic of Confluence Between Jialing River and the Yangtze River before and after Completion of the Three Gorges Reservoir. Port & Waterway Engineering. No.6 Serial No. 530. 1002-4972(2017)06-0144-06.

[33] Liu QY. 2010. The Flow and sediment transport patterns of open channel confluences in upstream reach of Yangtze River. The Chongqing Jiaotong University Master Thesis. 20100401.

[34] Liu TH, Chen, L, Fan, BL. 2012. Experiment study on flow pattern and sediment transportation at a 90° open-channel confluence. Int. J. Sediment Res.27 (2), 178-187.

[35] Mignot E, Vinkovic I, Doppler D, Riviere N. 2014. Mixing layer in open-channel junction flows. J. Environ Fluid Mech (2014) 14:1027–1041. DOI 10. 1007/s10652-013-9310-7.

[36] Modi PN, Dandekar MM, Ariel PD. 1981. Conformal mapping for channel junction flow. Journal of the Hydraulics Division, ASCE, 1981, Vol. 107, No. HY12, pp. 1713-1733.

[37] Mosley MP. 1976. An experimental study of channel confluences. J Geol, 107 1713-1733.

[38] Mohammadiun S, Neyshabouri SAAS, Naser B, Vahabi H. 2016. Numerical Investigation of Submerged Vane Effects on Flow Pattern in a 90- Junction of Straight and Bend Open Channels. Iranian Journal of Science and Technology - Transactions of Civil Engineering. 40(4):1–17. DOI:10. 1007/s40996-016-0039-7.

[39] Nikora VI, Goring DG. 1998. ADV Measurements of turbulence: can we improve their interpretation. Journal of Hydraulic Engineering, 124 (6), 630-634.

[40] Parhizkar H, Vahabi H, Mohammadiun S. 2015. Effects of open-channel geometry on flow pattern in a 90° junction. IJST, Transactions of Civil Engineering, Vol. 39, No. C2+, pp 559-573.

[41] Post GC. 2007. The measurement of Reynolds stresses in a model river bend using Acoustic Doppler Velocimeters. ISBN: 978-0-494-49265-9.

[42] Qiu XH, Tang HW, Yuan SY, Zhang HM, Yu DD, Li SM. 2015. Effects of discharge ratios on flow structure at a 90° flow confluence with degraded channel beds. E-proceedings of the 36th IAHR World Congress 28 June – 3 July, 2015.

[43] Rennie CD, Hay A. 2010. Reynolds Stress Estimates in a Tidal Channel from

Phase-Wrapped ADV Data. Journal of Coastal Research 26 1 157–166 West Palm Beach, Florida January 2010.

[44] Rice S. 1998. Which tributaries disrupt downstream fining along gravel-bed rivers? Geomorphology 22 (1), 39-56.

[45] Riley JD, Rhoads BL. 2012. Flow structure and channel morphology at a natural confluent meander bend. Geomorphology 163: 84–98. DOI: 10. 1016/j. geomorph. 2011. 06. 011.

[46] Riley JD, Rhoads BL, Parsons DR, Johnson KK. 2015. Influence of junction angle on three-dimensional flow structure and bed morphology at confluent meander bends. J. Earth Surf. Process. Landforms 40, 252–271 (2015). DOI: 10. 1002/esp. 3624.

[47] Rhoads BL, Kenworthy ST. 1995. Flow structure at an asymmetrical stream confluence. Geomorphology. 11: 273–293. DOI: 10. 1016/0169-555X (94)00069-4.

[48] Rhoads BL, Sukhodolov AN. 2001. Field investigation of three-dimensional flow structure at stream confluences: 1. Thermal mixing and time-averaged velocities. Water Resources Research 37: 2393–2410. DOI: 10. 1029/2001WR000316.

[49] Schindfessel L, Creëlle S, Mulder TD. 2015. Influence of cross-sectional shape on flow patterns in an open-channel confluence. R. E-proceedings of the 36th IAHR World Congress 28 June – 3 July, 2015.

[50] Sekine M, Parker G. 1992. Bed-load transport on transverse slope. I. J. Hydraul. Eng., 118, 513–535, DOI: 10. 1061/ (ASCE) 0733-9429(1992)118:4(513).

[51] Sharifipour M, Bonakdari H, Zaji AH, Shamshirband S. 2015. Numerical investigation of flow field and flowmeter accuracy in open channel junctions. J. Engineering Applications of Computational Fluid Mechanics, 2015 http://dx. doi. Org/10. 1080/19942060. 2015. 1008963.

[52] Tang HW, Li Q, Yuan SY, Li Z. 2017. Effect of aggregation on the adsorption of phosphorus onto air-dried sediment in contrasting shear flow conditions. J. Soil Sediment 17 (8), 2177–2186.

[53] Voulgaris G, Trowbridge JH. 1998. Evaluation of the Acoustic Doppler Velocimeter (ADV) for Turbulence Measurements. Journal of Atmospheric and Oceanic Technology, vol. 15, issue 1, p. 272. DOI: 10.1175/1520-0426(1998)015<0272: EOTADV>2.0.CO;2.

[54] Wang XK, Zhou SF, Ye L, Wang HZ. 2015. Numerical simulation of confluence flow structure between Jialing River and Yangtze River. Advances in Water Science. DOI: 10. 14042/j. cnki. 32. 1309. 2015. 03. 009.

[55] Wilcox DC. 2000. Turbulence Modeling for CFD (Third Edition). La Canada, CA: DCW Industries.

[56] Xiao Y, Xia Y, Yuan SY, Tang HW. 2017. Flow structure and phosphorus adsorption in bed sediment at a 90˚ channel confluence. J. Hydrodynamic 2017, 29(5):902-905 DOI: 10. 1016/S1001-6058(16)60804-1.

[57] Yan T. 2014. Preliminary Study on Sediment Deposition Law and Prevention of Confluence Reach in Reservoir. The Wuhan University Doctoral Thesis No. 10486.

[58] Yoshimura H, Moriguchi R, Fujita I. 2015. Numerical and experimental study of three dimensional flow structures and water surface fluctuations at a right-angled confluence, R. E-proceedings of the 36th IAHR World Congress, 28 June – 3 July, 2015.

[59] Yuan SY, Tang HW, Xiao Y, Qiu XH, Zhang HM, Yu DD. 2016. Turbulent flow structure at a 90° open channel confluence: accounting for the distortion of the shear layer. J Hydro-Environmental Res 12:130–147.

[60] Yuan SY, Tang HW, Xiao Y. Xi C, Xia Y, Jiang ZY. 2018. Spatial variability of phosphorus adsorption in surface sediment at channel confluences: Field and laboratory experimental evidence. J Hydro-Environmental Res 18:25-36.

[61] Yuan SY, Tang HW, Xiao Y, Qiu XH, Xia Y. 2017. Water flow and sediment transport at open-channel confluences: an experimental study. J. Hydraulic Res., in press. DOI: 10. 1080/00221686. 2017. 1354932.

[62] Zhang YF, Wang P, Wu BS, Hou SZ. 2012. An experimental study of fluvial processes at asymmetrical river confluences with hyper-concentrated tributary

flows. J. Geomorphology 230 (2015) 26–36.

[63] Zhao SW. 2005. Numerical Simulation of Flow Characteristic at 90° Open-Channel Junction. The Tsinghua University Master Thesis.

[64] Ettema, R. (2017) Multi-phase flows and processes, Section 3.5 in Experimental Hydraulics, Volume 1; M. Muste,, D.A. Lyn, D.M. Admiraal, R. Ettema, V. Nikora, and M.H. Garcia (Editors); Taylor and Francis, New York, N.Y.

Appendix 1: Sedimentation

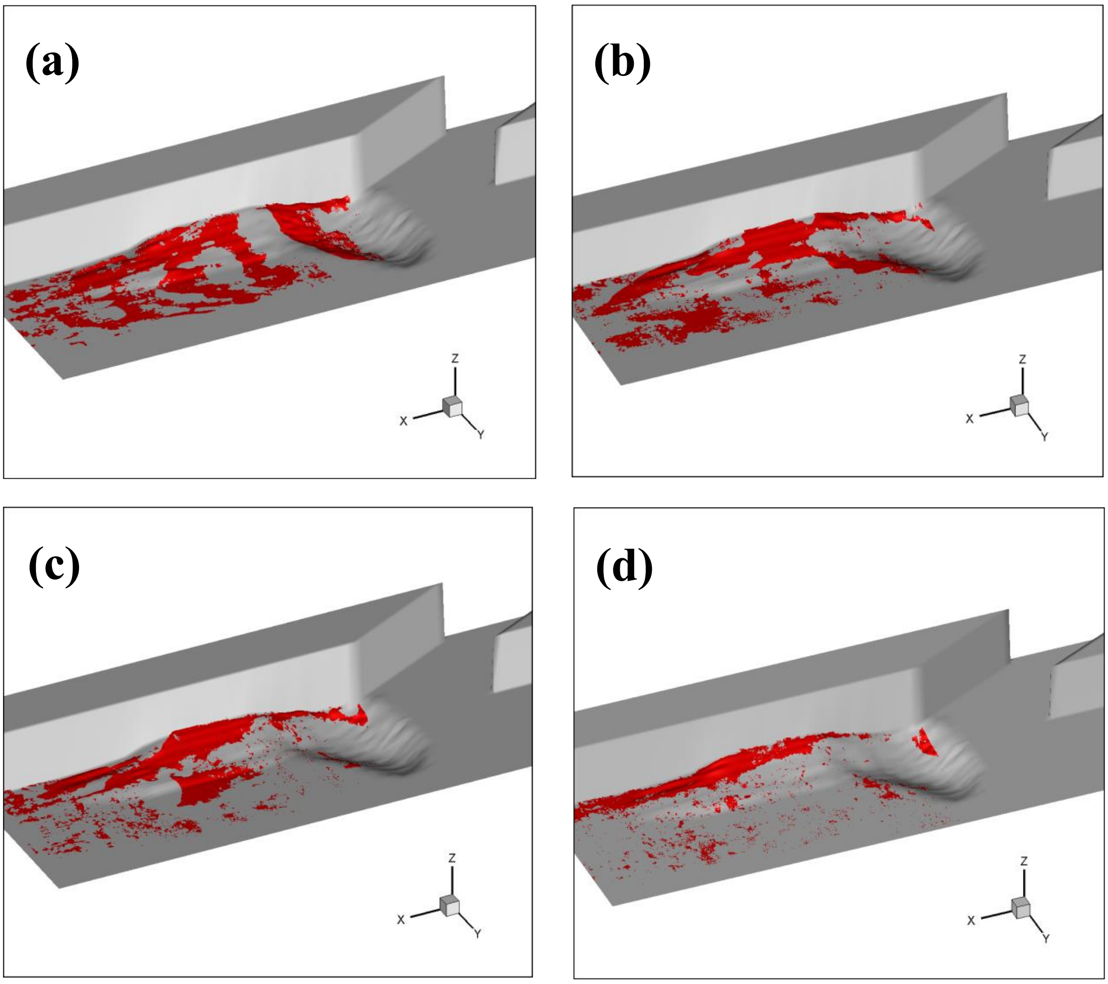

Figure 59. The sedimentation patterns for different time series in case 30_3_2. (a) 0 h; (b) 1 h; (c) 2 h; (d) 3 h.

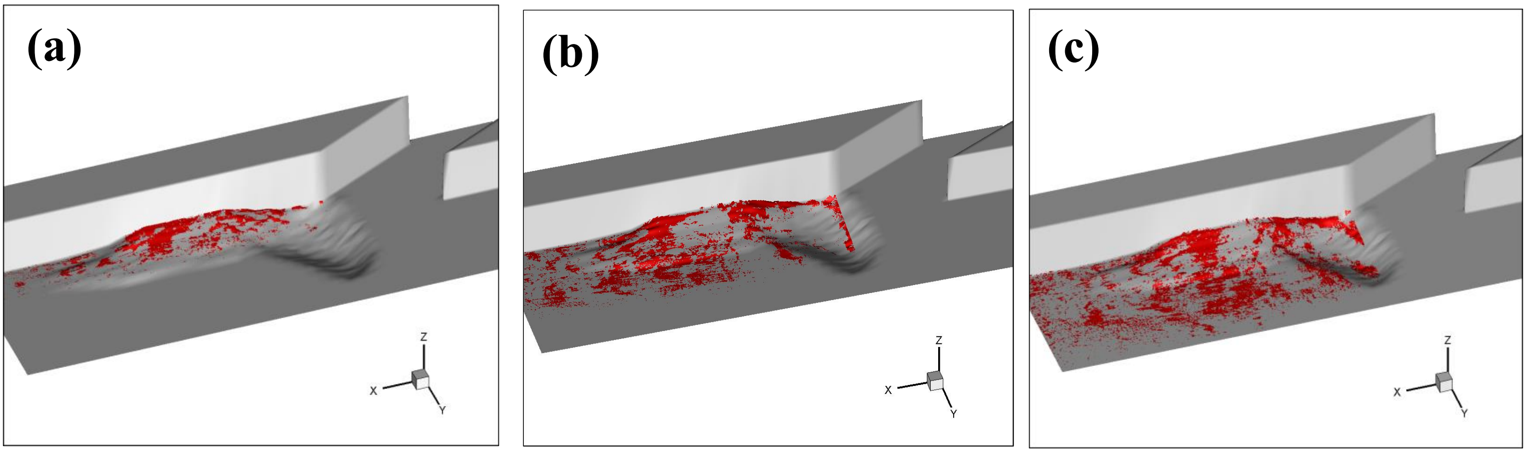

Figure 60. The sedimentation patterns for different feeding locations in case 30_2_3. (a) Fed from the left bank of tributary; (b) Fed from the mid channel of tributary; (c) Fed from the right bank of tributary.

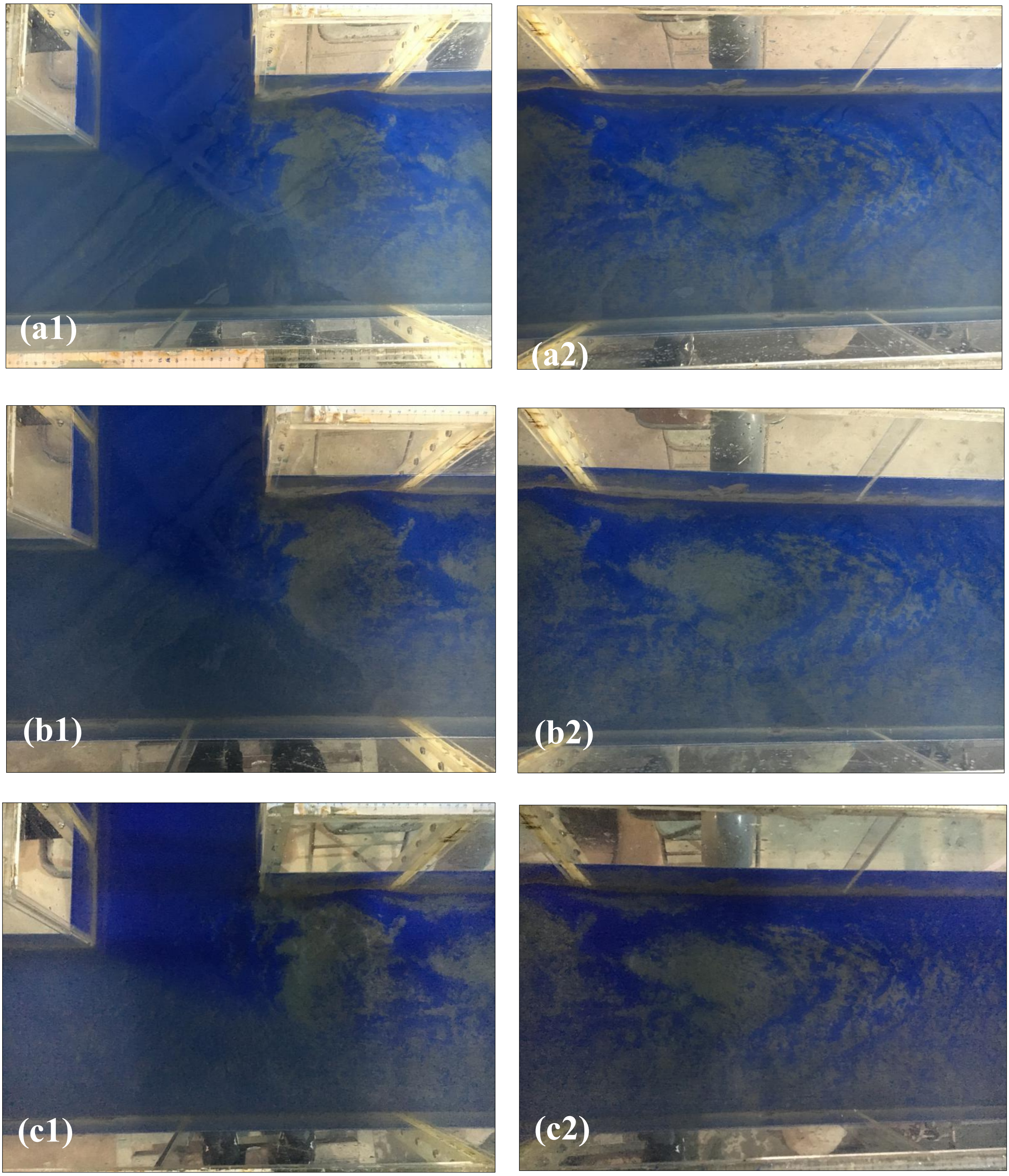

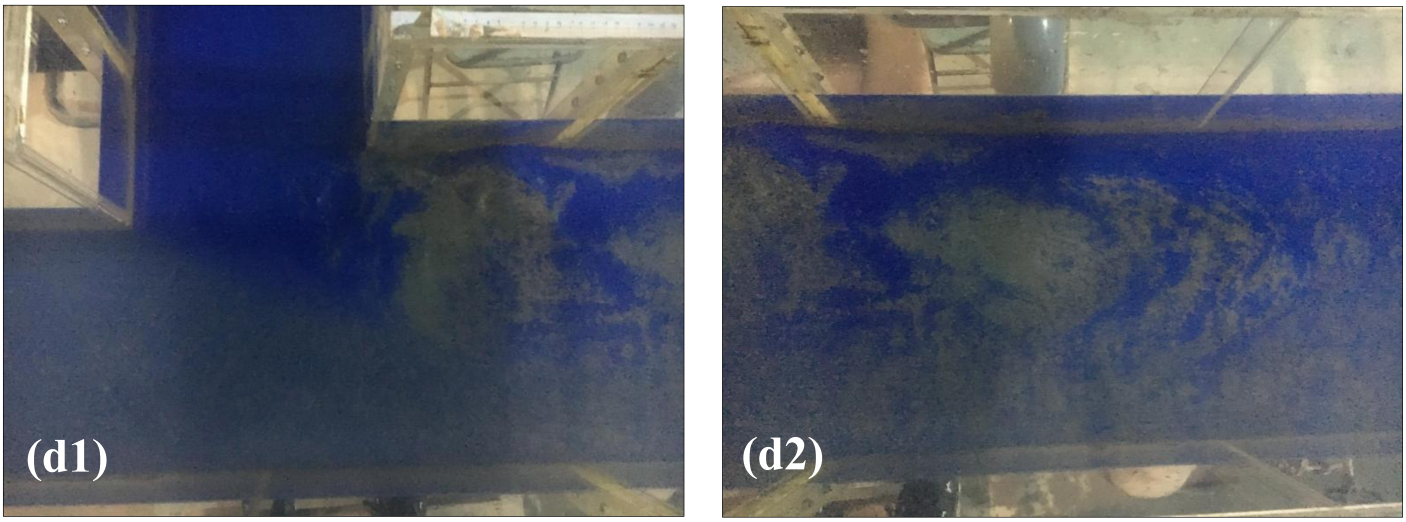

Figure 61. The sedimentation patterns for different time series in case 90_2_3. (a1) (a2) 0 h; (b1) (b2) 1 h; (c1) (c2) 2 h; (d1) (d2) 3 h.

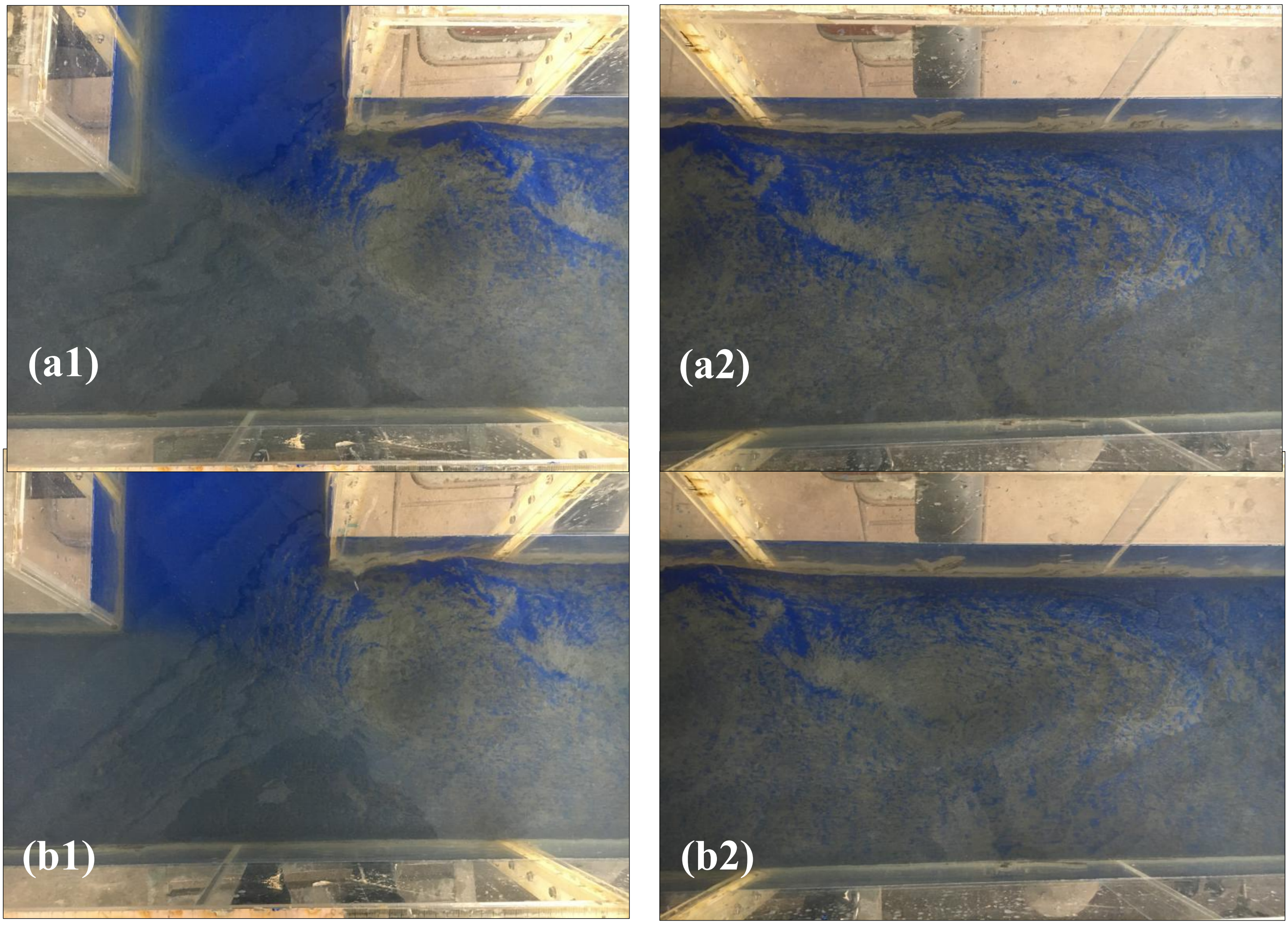

Figure 62. The sedimentation patterns for different feeding locations in case 90_2_3. (a1) (a2) Fed from the left bank of tributary; (b1) (b2) Fed from the right bank of tributary.

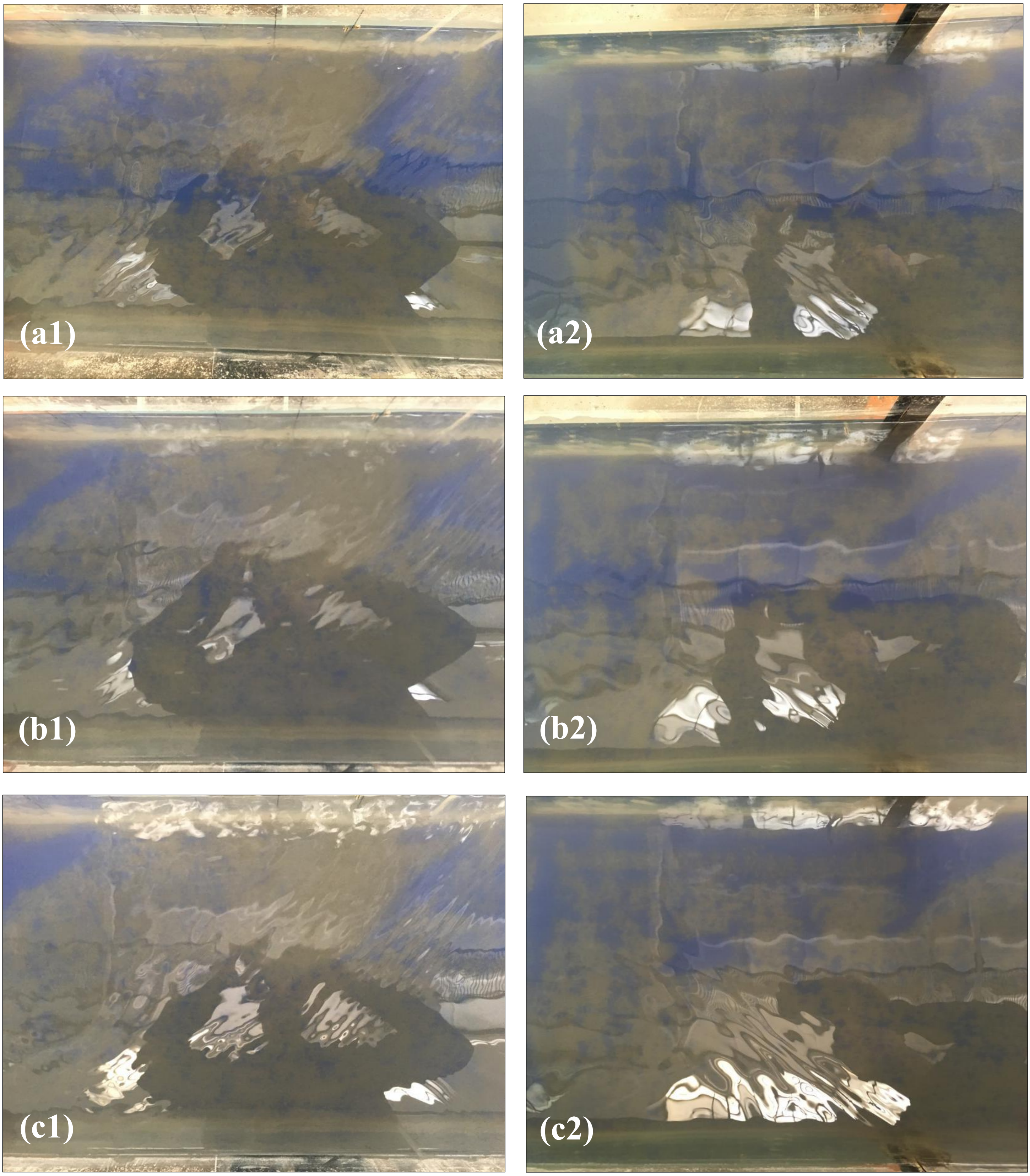

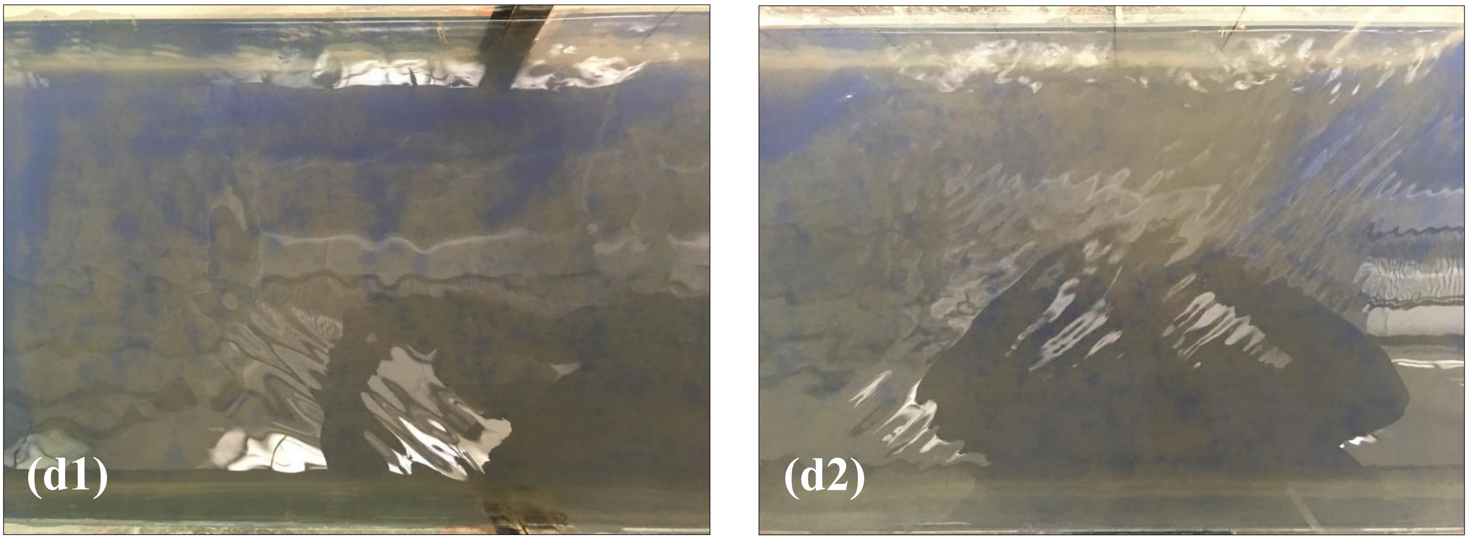

Figure 63. The sedimentation patterns for different time series in case 30_2_3. (a1) (a2) 0 h; (b1) (b2) 1 h; (c1) (c2) 2 h; (d1) (d2) 3 h.

Appendix 2: Matlab Code

2.1 The Flow Field Data Processing Code

2.1.1 “processVectrinobatch.m”

```
%assume water temperature in lab is 20degC, therefore
rho=998;%density of water in kg/m3, (note temp changed from 18degC to 22degC
during run
writematrixall=[];
%this file will process Vectrino .dat files
%load file
%Mikes note: files must begin with alphabetic character for this script to
%work properly


filename={'junction30_23_1_5cm_0'}

%Note you can add more file names to run several files one after the other.
% All results data for all files are stored in writematrixall (see line 95
% for what is stored)

for p=1:length(filename)
filescript = ['load ' filename{p} '.dat -ASCII'];
eval(filescript)

dummy=['tvec=' filename{p} '(:,1);'];
eval(dummy);
dummy=['vx=' filename{p} '(:,4);'];
eval(dummy);
dummy=['vy=' filename{p} '(:,5);'];%note vy follows right-hand rule with x forward
and z vertical
eval(dummy);
dummy=['vz1=' filename{p} '(:,6);'];
eval(dummy);
dummy=['vz2=' filename{p} '(:,7);'];
eval(dummy);
dummy=['amp1x=' filename{p} '(:,8);'];
eval(dummy);
dummy=['amp2y=' filename{p} '(:,9);'];
eval(dummy);
dummy=['amp3z=' filename{p} '(:,10);'];
```

```
eval(dummy);
dummy=['amp4w=' filename{p} '(:,11);'];
eval(dummy);
dummy=['snr1x=' filename{p} '(:,12);'];
eval(dummy);
dummy=['snr2y=' filename{p} '(:,13);'];
eval(dummy);
dummy=['snr3z=' filename{p} '(:,14);'];
eval(dummy);
dummy=['snr4w=' filename{p} '(:,15);'];
eval(dummy);
dummy=['cor1x=' filename{p} '(:,16);'];
eval(dummy);
dummy=['cor2y=' filename{p} '(:,17);'];
eval(dummy);
dummy=['cor3z=' filename{p} '(:,18);'];
eval(dummy);
dummy=['cor4w=' filename{p} '(:,19);'];
eval(dummy);

headerscript = ['FID = fopen( ''' filename{p} '.hdr'')'];
eval(headerscript)
for k=1:80
fgetl(FID);
end
advhead=fgetl(FID);
fclose(FID);

advheadnum=str2num(advhead(end-3:end));


%based on which adv, correct for twist of probe head.   The actual
%correction will occur after initial filtering in processVectrinocore
%Mike's note: it's not getting the 'advheadnum' value
xyrotate=0;
if advheadnum==7059
    xyrotate=2.658*pi/180;
elseif advheadnum==7047
    xyrotate=2.194*pi/180;
elseif advheadnum==7055
    xyrotate=2.497*pi/180;
end

timestep=tvec(2)-tvec(1);
```

```
if advheadnum==7857 %ie side looking ADV without duplicate vertical velocity
	processVectrinocoresidelooker
else
	processVectrinocore
end

spectralVectrinofinalfiltnoisebatch %does spectral analysis, and low pass filters data if
noise observed in spectrum

Vectrinooutput%note this calculates the turbulence scales, as well as the reynstresses
again in case the Vectrino data were low-pass filtered (Vectorfiltflag=1)

writematrix=[meanxraw meanyraw meanzraw uwreynstressraw uvreynstressraw
vwreynstressraw xrmsraw turbintxraw yrmsraw turbintyraw zrmsraw turbintzraw
turbkinenergyraw meanxdespike meanydespike meanzdespike uwreynstressdespike
uvreynstressdespike vwreynstressdespike xrmsdespike turbintxdespike yrmsdespike
turbintydespike zrmsdespike turbintzdespike turbkinenergydespike Vectorfiltflag
noisevx meanxfilt meanyfilt meanzfilt uwreynstressfilt uvreynstressfilt
vwreynstressfilt xrmsfilt turbintxfilt yrmsfilt turbintyfilt zrmsfilt turbintzfilt
turbkinenergyfilt integraltimescale microtime integrallengthscale microlengthscale
taylormicrolength integraltimescaley microtimey integrallengthscaley
microlengthscaley taylormicrolengthy integraltimescalez microtimez
integrallengthscalez microlengthscalez taylormicrolengthz];

writematrixall=[writematrixall; writematrix];

save VectrinoOutput writematrixall filename rho p
clear
load VectrinoOutput

end

xlswrite('VectrinoOutput',writematrixall)
```

2.1.2 “processVectrinocoresidelooker.m”

```
badvx=find(isnan(vx))
badvz1=find(isnan(vz1))
%badvz2=find(isnan(vz2))
```

```
%vz1_1307=vz1(1307)
%vz2_1307=vz2(1307)

%figure
%plot(tvec,vx)
%xlabel('time, s')
%ylabel('raw x vel, m/s')
%figure
%plot(tvec,vy)
%xlabel('time, s')
%ylabel('raw y vel, m/s')
%figure
%plot(tvec,vz1,tvec,vz2)
%xlabel('time, s')
%ylabel('raw z vels, m/s')
vzerrorraw=vz2-vz1;
%figure
%plot(tvec,vzerrorraw)
%xlabel('time, s')
%ylabel('raw z error, m/s')

%remove bad data
for k=1:length(vx)
    if vx(k)==3276.7 | vy(k)==3276.7 | vz1(k)==3276.7 |vx(k)==-3276.7 | vy(k)==-3276.7 | vz1(k)==-3276.7
        vx(k)=NaN;
        vy(k)=NaN;
        vz1(k)=NaN;
        vz2(k)=NaN;
    end
end
%remove bad data
for k=1:length(vx)
    if vx(k)==0
        vx(k)=NaN;
    end
    if vy(k)==0
        vy(k)=NaN;
    end
    if vz1(k)==0
        vz1(k)=NaN;
    end
%       if vz2(k)==0
%               vz2(k)=NaN;
```

```
%       end
end

%vz=(vz1+vz2)/2;
vz=vz1;

badvx=find(isnan(vx))
badvz=find(isnan(vz))

%Reynolds stress
meanxraw=nanmean(vx)
%stdvxraw_cmpers=(nanstd(vx)*100)^2
meanzraw=nanmean(vz)
meanz1raw=nanmean(vz1)
%stdvzraw_cmpers=(nanstd(vz)*100)^2
meanyraw=nanmean(vy)
fluctxraw=vx-meanxraw;
fluctzraw=vz-meanzraw;
%fluctz1raw=vz1-meanz1raw;
fluctyraw=vy-meanyraw;
%varuw_cmperssq=(nanstd(fluctxraw*100.*fluctzraw*100))^2
uwreynstressraw=-rho*nanmean(fluctxraw.*fluctzraw)%reynolds stress in N/m2
%uw1reynstressraw_cmpers=meanignoringNaN(fluctxraw*100.*fluctz1raw*100)%reynolds stress in N/m2
uvreynstressraw=-rho*nanmean(fluctxraw.*fluctyraw)%reynolds stress in N/m2
vwreynstressraw=-rho*nanmean(fluctzraw.*fluctyraw)%reynolds stress in N/m2
CDraw=-2*nanmean(fluctxraw.*fluctzraw)/meanxraw^2;

%statistics
xprsqrraw=fluctxraw.^2;
xrmsraw=sqrt(nanmean(xprsqrraw));
turbintxraw=xrmsraw/meanxraw;
yprsqrraw=fluctyraw.^2;
yrmsraw=sqrt(nanmean(yprsqrraw));
zprsqrraw=fluctzraw.^2;
zrmsraw=sqrt(nanmean(zprsqrraw));
turbintyraw=yrmsraw/meanyraw;
turbintzraw=zrmsraw/meanzraw;
%turbulent kinetic energy
turbkinenergyraw=0.5*(nanmean(xprsqrraw)+nanmean(yprsqrraw)+nanmean(zprsqrraw));


%vzerror=vz2-vz1;
```

```
%figure
%plot(tvec,vzerror)
%xlabel('time, s')
%ylabel('z vel error (vz2-vz1), m/s')
%vzerrorthresh=0.1;%interpolate data that exceeds vert vel error threshold
%for k=2:(length(vx)-1)
%       if abs(vzerror(k))>vzerrorthresh
%                   vx(k)=(vx(k-1)+vx(k+1))/2;
%                   vy(k)=(vy(k-1)+vy(k+1))/2;
%                   vz1(k)=(vz1(k-1)+vz1(k+1))/2;
%                   vz2(k)=(vz2(k-1)+vz2(k+1))/2;
%       end
%end

%figure
%plot(tvec,vx)
%xlabel('time, s')
%ylabel('x vel after vertvelerrorthresh despike, m/s')
%figure
%plot(tvec,vy)
%xlabel('time, s')
%ylabel('y vel after vertvelerrorthresh despike, m/s')
%figure
%plot(tvec,vz1)
%xlabel('time, s')
%ylabel('z1 vel after vertvelerrorthresh despike, m/s')

%despike v based on local acceleration (Nortek uses a 1 g filter)
%accelthresh=9.81*1.5;% used for Gavin
accelthresh=9.81;% Nortek default is one g acceleration cutoff threshold - I'm using
less severe 1.5
for k=2:(length(vx)-1)
      if abs((vx(k)-vx(k-1))/timestep)>accelthresh & abs((vx(k+1)-
vx(k))/timestep)>accelthresh
                  vx(k)=(vx(k-1)+vx(k+1))/2;
      end
      if abs((vy(k)-vy(k-1))/timestep)>accelthresh & abs((vy(k+1)-
vy(k))/timestep)>accelthresh
                  vy(k)=(vy(k-1)+vy(k+1))/2;
      end
      if abs((vz1(k)-vz1(k-1))/timestep)>accelthresh & abs((vz1(k+1)-
vz1(k))/timestep)>accelthresh
                  vz1(k)=(vz1(k-1)+vz1(k+1))/2;
      end
```

```
%       if abs((vz2(k)-vz2(k-1))/timestep)>accelthresh & abs((vz2(k+1)-
vz2(k))/timestep)>accelthresh
%                 vz2(k)=(vz2(k-1)+vz2(k+1))/2;
%       end
end
%figure
%plot(tvec,vx)
%xlabel('time, s')
%ylabel('x vel after accel<g despike, m/s')

%despikev by interpolating any values that are more than 4 (Gavin) or 3
%(Ali)
%standard deviations from the local mean
stdthresh=3;
startlength=10;
stdvx=nanstd(vx);
for k=(startlength+1):(length(vx)-1)
    if abs(vx(k)-nanmean(vx((k-startlength):(k-1))))>stdthresh*stdvx
            vx(k)=(vx(k-1)+vx(k+1))/2;
    end
end
stdvy=nanstd(vy);
for k=(startlength+1):(length(vy)-1)
    if abs(vy(k)-nanmean(vy((k-startlength):(k-1))))>stdthresh*stdvy
            vy(k)=(vy(k-1)+vy(k+1))/2;
    end
end
stdvz1=nanstd(vz1);
for k=(startlength+1):(length(vz1)-1)
    if abs(vz1(k)-nanmean(vz1((k-startlength):(k-1))))>stdthresh*stdvz1
        vz1(k)=(vz1(k-1)+vz1(k+1))/2;
    end
end
%stdvz2=nanstd(vz2);
%for k=(startlength+1):(length(vz2)-1)
%       if abs(vz2(k)-nanmean(vz2((k-startlength):(k-1))))>stdthresh*stdvz2
%           vz2(k)=(vz2(k-1)+vz2(k+1))/2;
%       end
%end

%figure
%plot(tvec,vx)
%xlabel('time, s')
%ylabel('x vel after std despike, m/s')
```

```
%vz=(vz1+vz2)/2;
vz=vz1;

%at least one adv head is twisted, therefore rotate by degree of twist for
%that head
if xyrotate~=0
        vxnew=vx.*cos(xyrotate)+vy.*sin(xyrotate);
        vynew=vy.*cos(xyrotate)-vx.*sin(xyrotate);
        vx=vxnew;
        vy=vynew;
        clear vxnew vynew
end

%%finally, Ali had the ADVs backwards.    Therefore make x and y negative
%vx=-vx;
%vy=-vy;

%calculate statistics.    Note: these are not raw. Rather, they are despiked,
%and rotated for adv head twist.
%Reynolds stress
meanxdespike=nanmean(vx)
meanzdespike=nanmean(vz)
meanydespike=nanmean(vy)
fluctxdespike=vx-meanxdespike;
fluctzdespike=vz-meanzdespike;
fluctydespike=vy-meanydespike;
uwreynstressdespike=-rho*nanmean(fluctxdespike.*fluctzdespike);%reynolds stress
in N/m2
uvreynstressdespike=-rho*nanmean(fluctxdespike.*fluctydespike);%reynolds stress
in N/m2
vwreynstressdespike=-rho*nanmean(fluctzdespike.*fluctydespike);%reynolds stress
in N/m2
CDdespike=-2*nanmean(fluctxdespike.*fluctzdespike)/meanxdespike^2;

%statistics
xprsqrdespike=fluctxdespike.^2;
xrmsdespike=sqrt(nanmean(xprsqrdespike));
turbintxdespike=xrmsdespike/meanxdespike;
yprsqrdespike=fluctydespike.^2;
yrmsdespike=sqrt(nanmean(yprsqrdespike));
zprsqrdespike=fluctzdespike.^2;
zrmsdespike=sqrt(nanmean(zprsqrdespike));
turbintydespike=yrmsdespike/meanydespike;
```

```
turbintzdespike=zrmsdespike/meanzdespike;
%turbulent kinetic energy
turbkinenergydespike=0.5*(nanmean(xprsqrdespike)+nanmean(yprsqrdespike)+nanm
ean(zprsqrdespike));
```

2.1.3 “processVectrinocore.m”

```
badvx=find(isnan(vx))
badvz1=find(isnan(vz1))
badvz2=find(isnan(vz2))

%vz1_1307=vz1(1307)
%vz2_1307=vz2(1307)

%figure
%plot(tvec,vx)
%xlabel('time, s')
%ylabel('raw x vel, m/s')
%figure
%plot(tvec,vy)
%xlabel('time, s')
%ylabel('raw y vel, m/s')
%figure
%plot(tvec,vz1,tvec,vz2)
%xlabel('time, s')
%ylabel('raw z vels, m/s')
vzerrorraw=vz2-vz1;
%figure
%plot(tvec,vzerrorraw)
%xlabel('time, s')
%ylabel('raw z error, m/s')

%remove bad data
for k=1:length(vx)
	if vx(k)==3276.7 | vy(k)==3276.7 | vz1(k)==3276.7 | vz2(k)==3276.7 |vx(k)==-
3276.7 | vy(k)==-3276.7 | vz1(k)==-3276.7 | vz2(k)==-3276.7
		vx(k)=NaN;
		vy(k)=NaN;
		vz1(k)=NaN;
		vz2(k)=NaN;
	end
end
%remove bad data
```

```
for k=1:length(vx)
        if vx(k)==0
                vx(k)=NaN;
        end
        if vy(k)==0
                vy(k)=NaN;
        end
        if vz1(k)==0
                vz1(k)=NaN;
        end
        if vz2(k)==0
                vz2(k)=NaN;
        end
end

vz=(vz1+vz2)/2;

badvx=find(isnan(vx))
badvz=find(isnan(vz))

%Reynolds stress
meanxraw=nanmean(vx)
%stdvxraw_cmpers=(nanstd(vx)*100)^2
meanzraw=nanmean(vz)
meanz1raw=nanmean(vz1)
%stdvzraw_cmpers=(nanstd(vz)*100)^2
meanyraw=nanmean(vy)
fluctxraw=vx-meanxraw;
fluctzraw=vz-meanzraw;
%fluctz1raw=vz1-meanz1raw;
fluctyraw=vy-meanyraw;
%varuw_cmperssq=(nanstd(fluctxraw*100.*fluctzraw*100))^2
uwreynstressraw=-rho*nanmean(fluctxraw.*fluctzraw)%reynolds stress in N/m2
%uw1reynstressraw_cmpers=meanignoringNaN(fluctxraw*100.*fluctz1raw*100)%re
ynolds stress in N/m2
uvreynstressraw=-rho*nanmean(fluctxraw.*fluctyraw)%reynolds stress in N/m2
vwreynstressraw=-rho*nanmean(fluctzraw.*fluctyraw)%reynolds stress in N/m2
CDraw=-2*nanmean(fluctxraw.*fluctzraw)/meanxraw^2;

%statistics
xprsqrraw=fluctxraw.^2;
xrmsraw=sqrt(nanmean(xprsqrraw));
turbintxraw=xrmsraw/meanxraw;
yprsqrraw=fluctyraw.^2;
```

```
yrmsraw=sqrt(nanmean(yprsqrraw));
zprsqrraw=fluctzraw.^2;
zrmsraw=sqrt(nanmean(zprsqrraw));
turbintyraw=yrmsraw/meanyraw;
turbintzraw=zrmsraw/meanzraw;
%turbulent kinetic energy
turbkinenergyraw=0.5*(nanmean(xprsqrraw)+nanmean(yprsqrraw)+nanmean(zprsqrr
aw));


vzerror=vz2-vz1;
%figure
%plot(tvec,vzerror)
%xlabel('time, s')
%ylabel('z vel error (vz2-vz1), m/s')
vzerrorthresh=0.1;%interpolate data that exceeds vert vel error threshold
for k=2:(length(vx)-1)
    if abs(vzerror(k))>vzerrorthresh
            vx(k)=(vx(k-1)+vx(k+1))/2;
            vy(k)=(vy(k-1)+vy(k+1))/2;
            vz1(k)=(vz1(k-1)+vz1(k+1))/2;
            vz2(k)=(vz2(k-1)+vz2(k+1))/2;
    end
end

%figure
%plot(tvec,vx)
%xlabel('time, s')
%ylabel('x vel after vertvelerrorthresh despike, m/s')
%figure
%plot(tvec,vy)
%xlabel('time, s')
%ylabel('y vel after vertvelerrorthresh despike, m/s')
%figure
%plot(tvec,vz1)
%xlabel('time, s')
%ylabel('z1 vel after vertvelerrorthresh despike, m/s')

%despike v based on local acceleration (Nortek uses a 1 g filter)
%accelthresh=9.81*1.5;% used for Gavin
accelthresh=9.81;% Nortek default is one g acceleration cutoff threshold - I'm using
less severe 1.5
for k=2:(length(vx)-1)
    if abs((vx(k)-vx(k-1))/timestep)>accelthresh & abs((vx(k+1)-
```

```
vx(k))/timestep)>accelthresh
                vx(k)=(vx(k-1)+vx(k+1))/2;
        end
        if abs((vy(k)-vy(k-1))/timestep)>accelthresh & abs((vy(k+1)-
vy(k))/timestep)>accelthresh
                vy(k)=(vy(k-1)+vy(k+1))/2;
        end
        if abs((vz1(k)-vz1(k-1))/timestep)>accelthresh & abs((vz1(k+1)-
vz1(k))/timestep)>accelthresh
                vz1(k)=(vz1(k-1)+vz1(k+1))/2;
        end
        if abs((vz2(k)-vz2(k-1))/timestep)>accelthresh & abs((vz2(k+1)-
vz2(k))/timestep)>accelthresh
                vz2(k)=(vz2(k-1)+vz2(k+1))/2;
        end
end
%figure
%plot(tvec,vx)
%xlabel('time, s')
%ylabel('x vel after accel<g despike, m/s')

%despikev by interpolating any values that are more than 4 (Gavin) or 3
%(Ali)
%standard deviations from the local mean
stdthresh=3;
startlength=10;
stdvx=nanstd(vx);
for k=(startlength+1):(length(vx)-1)
        if abs(vx(k)-nanmean(vx((k-startlength):(k-1))))>stdthresh*stdvx
                vx(k)=(vx(k-1)+vx(k+1))/2;
        end
end
stdvy=nanstd(vy);
for k=(startlength+1):(length(vy)-1)
        if abs(vy(k)-nanmean(vy((k-startlength):(k-1))))>stdthresh*stdvy
                vy(k)=(vy(k-1)+vy(k+1))/2;
        end
end
stdvz1=nanstd(vz1);
for k=(startlength+1):(length(vz1)-1)
        if abs(vz1(k)-nanmean(vz1((k-startlength):(k-1))))>stdthresh*stdvz1
            vz1(k)=(vz1(k-1)+vz1(k+1))/2;
        end
end
```

```
stdvz2=nanstd(vz2);
for k=(startlength+1):(length(vz2)-1)
    if abs(vz2(k)-nanmean(vz2((k-startlength):(k-1))))>stdthresh*stdvz2
        vz2(k)=(vz2(k-1)+vz2(k+1))/2;
    end
end

%figure
%plot(tvec,vx)
%xlabel('time, s')
%ylabel('x vel after std despike, m/s')

vz=(vz1+vz2)/2;

%at least one adv head is twisted, therefore rotate by degree of twist for
%that head
if xyrotate~=0
    vxnew=vx.*cos(xyrotate)+vy.*sin(xyrotate);
    vynew=vy.*cos(xyrotate)-vx.*sin(xyrotate);
    vx=vxnew;
    vy=vynew;
    clear vxnew vynew
end

%%finally, Ali had the ADVs backwards.  Therefore make x and y negative
%vx=-vx;
%vy=-vy;

%calculate statistics.  Note: these are not raw. Rather, they are despiked,
%and rotated for adv head twist.
%Reynolds stress
meanxdespike=nanmean(vx)
meanzdespike=nanmean(vz)
meanydespike=nanmean(vy)
fluctxdespike=vx-meanxdespike;
fluctzdespike=vz-meanzdespike;
fluctydespike=vy-meanydespike;
uwreynstressdespike=-rho*nanmean(fluctxdespike.*fluctzdespike);%reynolds stress in N/m2
uvreynstressdespike=-rho*nanmean(fluctxdespike.*fluctydespike);%reynolds stress in N/m2
vwreynstressdespike=-rho*nanmean(fluctzdespike.*fluctydespike);%reynolds stress in N/m2
CDdespike=-2*nanmean(fluctxdespike.*fluctzdespike)/meanxdespike^2;
```

```
%statistics
xprsqrdespike=fluctxdespike.^2;
xrmsdespike=sqrt(nanmean(xprsqrdespike));
turbintxdespike=xrmsdespike/meanxdespike;
yprsqrdespike=fluctydespike.^2;
yrmsdespike=sqrt(nanmean(yprsqrdespike));
zprsqrdespike=fluctzdespike.^2;
zrmsdespike=sqrt(nanmean(zprsqrdespike));
turbintydespike=yrmsdespike/meanydespike;
turbintzdespike=zrmsdespike/meanzdespike;
%turbulent kinetic energy
turbkinenergydespike=0.5*(nanmean(xprsqrdespike)+nanmean(yprsqrdespike)+nanmean(zprsqrdespike));
```

2.1.4 “spectralVectrinofinalfiltnoisebatch.m”

```
%spectralVectrinofinalfiltnoisebatch

%this algorithm will do spectral analysis on Vectrino data, will filt if
%noise level exceeds a threshold, and will then output final stats

    %first, fill in missing values
    vxwoNaN=interpolateNaN(vx);
    vywoNaN=interpolateNaN(vy);
    vzwoNaN=interpolateNaN(vz);

%% Mikes linear interpolation of NaN
%
%vx_interp_ts = resample(timeseries(vx),timeseries(vx).time);
%vxwoNaN = vx_interp_ts.data;
%
%vy_interp_ts = resample(timeseries(vy),timeseries(vy).time);
%vywoNaN = vy_interp_ts.data;
%
%vz_interp_ts = resample(timeseries(vz),timeseries(vz).time);
%vzwoNaN = vz_interp_ts.data;


SampleRate=timestep;%200Hz sampling max for Vectrino

%spectrum
```

```
Ts = timestep;%sampling rate;
Hs = 1/Ts;%sampling frequency
Hn = Hs/2%Nyquist frequency
nwindows=4;%number of windows
nfft=floor(length(vxwoNaN)/nwindows);%length of data for each window
noverlap=floor(nfft/2);%overlap of each window
window=hanning(nfft);
[P,F]=spectrum(vxwoNaN,vzwoNaN,nfft,noverlap,window,Hs);
fftvx=P(:,1).*2.*Ts;%area under curve should equal variance of data, so this is correct
conversion (Steve Ponds)
fftvz=P(:,2).*2.*Ts;%ie divide by Nyquist
fftcross=P(:,3);
%find -5/3
fivethirds=F.^(-5/3);
scaledfivethirds=fivethirds.*fftvx(10)./F(10).^(-5/3).*5;%just to show a five thirds
line on plot
scaledfivethirdsz=fivethirds.*fftvz(10)./F(10).^(-5/3).*5;%just to show a five thirds
line on plot
meanvxspecdensity=mean(fftvx);
meanvzspecdensity=mean(fftvz);
meancrossspecdensity=mean(fftcross);
coherencevxvz=P(:,5);
lowerconflimitvx=(P(:,1)-P(:,6)).*2.*Ts;
upperconflimitvx=(P(:,1)+P(:,6)).*2.*Ts;
lowerconflimitvz=(P(:,2)-P(:,7)).*2.*Ts;
upperconflimitvz=(P(:,2)+P(:,7)).*2.*Ts;
lowerconflimitcross=P(:,3)-P(:,8);
upperconflimitcross=P(:,3)+P(:,8);

%fit a noise level to spectrum
%determine where inertial range should be.   Assume starts at 1 Hz, but
%certainly at 5 Hz.   Therefore, find F=5
%Actually, Ali data show integral range starting at about 1 Hz, therefore
%I'll use 2 Hz
%for Gavin data, looks like about 1 Hz
upperinertial=1;
ftest=1;
while F(ftest)<upperinertial
    ftest=ftest+1;
end
%inertialF=F(ftest)%just to check
Fforfit=(F(ftest:end));
fftvxforfit=(fftvx(ftest:end));
fftvzforfit=(fftvz(ftest:end));
```

```
          xdata = Fforfit;
          ydata = fftvxforfit;
          xo=[fftvx(10)./F(10).^(-5/3) fftvx(end)];
        fun = inline('x(1)*xdata.^(-5/3)+x(2)','x','xdata');
        x = lsqcurvefit(fun,xo, xdata, ydata)
        xfit=x(1).*xdata.^(-5/3)+x(2);

          %find noise in m/s by integrating over spectrum
        N=x(2);
        noisevx = sqrt(N*F(end))%noise vx in m/s


        y2data = fftvzforfit;
          xo2=[fftvz(10)./F(10).^(-5/3) fftvz(end)];
        fun2 = inline('x2(1)*xdata.^(-5/3)+x2(2)','x2','xdata');
        x2 = lsqcurvefit(fun2,xo2, xdata, y2data)
        zfit=x2(1).*xdata.^(-5/3)+x2(2);

                      %find noise in m/s by integrating over spectrum
        N2=x2(2);
        noisevz = sqrt(N2*F(end))%noise vx in m/s

        %look for total variance in spectrum
varspec=sum((fftvx)*(F(2)-F(1)))
varvx=var(vxwoNaN)%this is a problem - it appears to be off by a factor of about 3

%filter data if noise too high
%noisecutoff=0.3;
%noiseratio=abs(noisevx/Vectormeanx);
noisecutoff=0.75;
meanabsfluctx=mean(abs(fluctxraw))

noiseratio=abs(noisevx/meanabsfluctx)%this might make more sense: if fluctuations
are due to noise, then reynolds stress unreliable

Vectorfiltflag=0;
if noiseratio>noisecutoff%perform lowpass filter
    Vectorfiltflag=1;
    [b,a]=butter(10,.4);%might need to adjust this to determine frequency cutoff for
filtering. The second number is the cutoff frequency scaled by Nyquist
%for Ali data, collected at 25 Hz, the 0.4 cutoff is 5 Hz (0.4*12.5=5)
    filtvx = filtfilt(b,a,vxwoNaN);
    filtvy = filtfilt(b,a,vywoNaN);
```

```
        filtvz = filtfilt(b,a,vzwoNaN);

        vxwoNaN=filtvx;%rename so I can use same code again
        vywoNaN=filtvy;
        vzwoNaN=filtvz;

[P,F]=spectrum(vxwoNaN,vzwoNaN,nfft,noverlap,window,Hs);
fftvx=P(:,1).*2.*Ts;%area under curve should equal variance of data, so this is correct
conversion (Steve Ponds)
fftvz=P(:,2).*2.*Ts;%ie divide by Nyquist
fftcross=P(:,3);
%find -5/3
fivethirds=F.^(-5/3);
scaledfivethirds=fivethirds.*fftvx(10)./F(10).^(-5/3).*5;%just to show a five thirds
line on plot
scaledfivethirdsz=fivethirds.*fftvz(10)./F(10).^(-5/3).*5;%just to show a five thirds
line on plot
meanvxspecdensity=mean(fftvx);
meanvzspecdensity=mean(fftvz);
meancrossspecdensity=mean(fftcross);
coherencevxvz=P(:,5);
lowerconflimitvx=(P(:,1)-P(:,6)).*2.*Ts;
upperconflimitvx=(P(:,1)+P(:,6)).*2.*Ts;
lowerconflimitvz=(P(:,2)-P(:,7)).*2.*Ts;
upperconflimitvz=(P(:,2)+P(:,7)).*2.*Ts;
lowerconflimitcross=P(:,3)-P(:,8);
upperconflimitcross=P(:,3)+P(:,8);

%figure(22), clf
%%figure
%subplot(3,1,1)
%loglog(F,fftvx,'k-',F,lowerconflimitvx,'g-',F,upperconflimitvx,'g-
',F,meanvxspecdensity,'r',F(10:end),scaledfivethirds(10:end),'c')
%ylabel('x, m^2/s')%units are units^2/frequency
%legend('original','~ conf',0)%note this is matlab 95% conf interval - not Nuttal for
windows
%title([filename{p} ' spectral density and coherence'],'FontSize',14)
%subplot(3,1,2)
%loglog(F,fftvz,'k-',F,lowerconflimitvz,'g-',F,upperconflimitvz,'g-
',F,meanvzspecdensity,'r',F(10:end),scaledfivethirdsz(10:end),'c')
%ylabel('z, m^2/s')%units are units^2/frequency
%legend('original','~ conf',0)
%subplot(3,1,3)
%semilogx(F,coherencevxvz,'k-')%note coherence is the normalized cross-spectrum,
```

```
where complex is eliminated by taking absolute
%%therefore coherence has value between 0 and 1
%xlabel('frequency, Hz')
%ylabel('coherence vxvz,')

%fit a noise level to spectrum
Fforfit=(F(ftest:end));
fftvxforfit=(fftvx(ftest:end));
fftvzforfit=(fftvz(ftest:end));

          xdata = Fforfit;
          ydata = fftvxforfit;
          xo=[fftvx(10)./F(10).^(-5/3) fftvx(end)];
         fun = inline('x(1)*xdata.^(-5/3)+x(2)','x','xdata');
         x = lsqcurvefit(fun,xo, xdata, ydata)
         xfit=x(1).*xdata.^(-5/3)+x(2);

          %find noise in m/s by integrating over spectrum
         N=x(2);
         noisevxfilt = sqrt(N*F(end))%noise vx in m/s


         y2data = fftvzforfit;
          xo2=[fftvz(10)./F(10).^(-5/3) fftvz(end)];
         fun2 = inline('x2(1)*xdata.^(-5/3)+x2(2)','x2','xdata');
         x2 = lsqcurvefit(fun2,xo2, xdata, y2data)
         zfit=x2(1).*xdata.^(-5/3)+x2(2);

                  %find noise in m/s by integrating over spectrum
         N2=x2(2);
         noisevzfilt = sqrt(N2*F(end))%noise vx in m/s
         else
         noisevxfilt=NaN;
         noisevzfilt=NaN;
end

%recompute statistics with filtered data.   Note, if no filtering applied,
%these should be the same as despiked.
     %Reynolds stress
     meanxfilt=meanignoringNaN(vxwoNaN)
     meanzfilt=meanignoringNaN(vzwoNaN)
     meanyfilt=meanignoringNaN(vywoNaN)
     fluctx=vxwoNaN-meanxfilt;%leave these names, so can use correlation code
next
```

```
    fluctz=vzwoNaN-meanzfilt;
    flucty=vywoNaN-meanyfilt;
    uwreynstressfilt=-rho*meanignoringNaN(fluctx.*fluctz)%reynolds stress in
N/m2
    uvreynstressfilt=-rho*meanignoringNaN(fluctx.*flucty)%reynolds stress in
N/m2
    vwreynstressfilt=-rho*meanignoringNaN(fluctz.*flucty)%reynolds stress in
N/m2
    CDfilt=-2*meanignoringNaN(fluctx.*fluctz)/meanxfilt^2;

    %statistics
    xprsqr=fluctx.^2;
    xrmsfilt=sqrt(meanignoringNaN(xprsqr))
    turbintxfilt=xrmsfilt/meanxfilt;
    relturbintxfilt=turbintxfilt
    yprsqr=flucty.^2;
    yrmsfilt=sqrt(meanignoringNaN(yprsqr))
    zprsqr=fluctz.^2;
    zrmsfilt=sqrt(meanignoringNaN(zprsqr))
    turbintyfilt=yrmsfilt/meanyfilt;
    turbintzfilt=zrmsfilt/meanzfilt;
    relturbintyfilt=turbintyfilt
    relturbintzfilt=turbintzfilt
    relturbintyfiltreltoU=yrmsfilt/meanxfilt
    relturbintzfiltreltoU=zrmsfilt/meanxfilt
    %turbulent kinetic energy

turbkinenergyfilt=0.5*(meanignoringNaN(xprsqr)+meanignoringNaN(yprsqr)+meani
gnoringNaN(zprsqr))
```

2.1.5 “Vectrinooutput.m”

```
%Vectrinooutput
%this now just calculates turbulence scales from the correlation function
%as it is written now

%find correlation coefficient (R)
cnt=length(tvec);
num=floor((cnt-1)/2);
for tau=0:1:(num-1)
    N=0;
    sumx=0;
    sumy=0;
```

```
        sumz=0;
        for N=1:1:(cnt-tau-1)
                sumx=sumx+fluctx(N)*fluctx(N+tau);
                sumy=sumy+flucty(N)*flucty(N+tau);
                sumz=sumz+fluctz(N)*fluctz(N+tau);
        end
        corltnx(tau+1)=sumx/(cnt-tau-1);
        corltny(tau+1)=sumy/(cnt-tau-1);
        corltnz(tau+1)=sumz/(cnt-tau-1);
        taup(tau+1)=tau*timestep;
end
Rxmine=corltnx/meanignoringNaN(xprsqr);
Rymine=corltny/meanignoringNaN(yprsqr);
Rzmine=corltnz/meanignoringNaN(zprsqr);

%do x,y,z scales separately

%x
%find integral time scale, and if turbintensity<0.25, integral length scale
%(using Taylor's frozen field hypothesis)
%first, integrate Rx until Rx<0
k=1;
while Rxmine(k)>0
        if k<length(Rxmine)
                k=k+1;
        else
                break
        end
end

Rfit=Rxmine(1:(k-1));
integraltimescale=Rfit(1)*timestep/2+sum(Rfit(2:end))*timestep%in s
%find microtimescale - note the sample volume may be too large
derivx=diff(fluctx)/timestep;%approximate derivative of x fluctuations
derivxsq=derivx.^2;
microtime=sqrt(2)*sqrt(meanignoringNaN(xprsqr))/sqrt(sum(derivxsq)/cnt)
if abs(turbintxfilt)<0.25
        integrallengthscale=meanignoringNaN(vx)*integraltimescale
        microlengthscale=meanignoringNaN(vx)*microtime;
        taylormicrolength=microlengthscale/sqrt(2);
else
        integrallengthscale=NaN
        microlengthscale=NaN;
        taylormicrolength=NaN;
```

```
end

%y
%find integral time scale, and if turbintensity<0.25, integral length scale
%(using Taylor's frozen field hypothesis)
%first, integrate Ry until Ry<0
k=1;
while Rymine(k)>0
        if k<length(Rymine)
                k=k+1;
        else
                break
        end
end

Rfity=Rymine(1:(k-1));
integraltimescaley=Rfity(1)*timestep/2+sum(Rfity(2:end))*timestep%in s
%find microtimescale - note the sample volume may be too large
derivy=diff(flucty)/timestep;%approximate derivative of x fluctuations
derivysq=derivy.^2;
microtimey=sqrt(2)*sqrt(meanignoringNaN(yprsqr))/sqrt(sum(derivysq)/cnt)
if abs(turbintyfilt)<0.25
        integrallengthscaley=meanignoringNaN(vy)*integraltimescaley;
        microlengthscaley=meanignoringNaN(vy)*microtimey;
        taylormicrolengthy=microlengthscaley/sqrt(2);
else
        integrallengthscaley=NaN;
        microlengthscaley=NaN;
        taylormicrolengthy=NaN;
end

%z
%find integral time scale, and if turbintensity<0.25, integral length scale
%(using Taylor's frozen field hypothesis)
%first, integrate Rz until Rz<0
k=1;
while Rzmine(k)>0
        if k<length(Rzmine)
                k=k+1;
        else
                break
        end
end
```

```
Rfitz=Rzmine(1:(k-1));
integraltimescalez=Rfitz(1)*timestep/2+sum(Rfitz(2:end))*timestep%in s
%find microtimescale - note the sample volume may be too large
derivz=diff(fluctz)/timestep;%approximate derivative of x fluctuations
derivzsq=derivz.^2;
microtimez=sqrt(2)*sqrt(meanignoringNaN(zprsqr))/sqrt(sum(derivzsq)/cnt)
if abs(turbintzfilt)<0.25
	integrallengthscalez=meanignoringNaN(vz)*integraltimescalez;
	microlengthscalez=meanignoringNaN(vz)*microtimez;
	taylormicrolengthz=microlengthscalez/sqrt(2);
else
	integrallengthscalez=NaN;
	microlengthscalez=NaN;
	taylormicrolengthz=NaN;
end
```

2.2 Sedimentation Image Converting Code

```
close all
clear all
clc

%Interp
source_x = xlsread('Binary data_mid.xlsx','topo','B1:AY1');
source_y = xlsread('Binary data_mid.xlsx','topo','A2:A78');
source_z = xlsread('Binary data_mid.xlsx','topo','B2:AY78');
interp_x = xlsread('Binary data_mid.xlsx','interp','B1:ARJ1');
interp_y = xlsread('Binary data_mid.xlsx','interp','A2:A466');
interp_z = interp2(source_x,source_y',source_z,interp_x',interp_y','spline');
figure,surf(interp_x,interp_y,interp_z);
xlabel('interp_x');
ylabel('interp_y');
zlabel('interp_z');
title('spline')
shading interp
xlswrite('Binary data_mid.xlsx',interp_z,'interp','B2');

%Left flume edge
edge_left_x = xlsread('Binary data_mid.xlsx','interp','B1:K1');
edge_left_y = xlsread('Binary data_mid.xlsx','interp','A2:A250');
edge_left_z = ones(length(edge_left_y(:)),length(edge_left_x(:)))*0.2;
xlswrite('Binary data_mid.xlsx',edge_left_z,'interp','B2');
```

```
%Right flume edge
edge_right_x = xlsread('Binary data_mid.xlsx','interp','HS1:ARJ1');
edge_right_y = xlsread('Binary data_mid.xlsx','interp','A2:A178');
edge_right_z = ones(length(edge_right_y(:)),length(edge_right_x(:)))*0.2;
xlswrite('Binary data_mid.xlsx',edge_right_z,'interp','HS2');

%Data line up
Lx = length(interp_x)
Ly = length(interp_y)
for i = 1:Lx
for j = 1:Ly
        X(j,i) = interp_x(1,i);
        Y(j,i) = interp_y(j,1);
end
end
X = X(:);
X = roundn(X,-2);
Y = Y(:);
Y = roundn(Y,-2);
Z = xlsread('Binary data_mid.xlsx','interp','B2:ARJ466');
Z = Z(:)*100;
Z = roundn(Z,-2);
Sed = xlsread('Binary data_mid.xlsx','binary','B2:ARJ466');
Sed = Sed(:) ;
Sed = roundn(Sed,-2);
result = [X,Y,Z,Sed];

%Output into dat. flie
fid = fopen('seditopo.dat','wt');
title = 'variables="x","y","z","Sed"';
fprintf(fid,'%s\n',title);
[m,n] = size(result)
for j = 1:m
for z = 1:n
if z == n
fprintf(fid,'%g\n',result(j,z));
else
fprintf(fid,'%g\t',result(j,z));
end
end
end
fclose(fid);
```